



Paula Nomura Watanabe

**Wear analysis of bypass valves applied on
regulated-two-stages turbocharger**

*Análise de desgaste de válvulas de bypass
aplicadas a turbocompressores de dois estágios
regulados*

71/2014

CAMPINAS
2014



UNICAMP

UNIVERSIDADE ESTADUAL DE CAMPINAS
FACULDADE DE ENGENHARIA MECÂNICA

PAULA NOMURA WATANABE

Wear analysis of bypass valves applied on regulated-two-stages turbocharger

Análise de desgaste de válvulas de bypass aplicadas a turbocompressores de dois estágios regulados

Master Dissertation presented to the School of Mechanical Engineering of the University of Campinas in partial fulfillment of the requirements for the degree of Master in Mechanical Engineering, in the Mechanic of Solids and Mechanic Projects.

Dissertação de Mestrado apresentada à Faculdade de Engenharia Mecânica da Universidade Estadual de Campinas como parte dos requisitos exigidos para obtenção do título de Mestra em Engenharia Mecânica, na Área de Mecânica dos Sólidos e Projeto Mecânico.

Orientador: Prof. Dr. Milton Dias Júnior

ESTE EXEMPLAR CORRESPONDE À VERSÃO
FINAL DA DISSERTAÇÃO DEFENDIDA PELA
ALUNA PAULA NOMURA WATANABE E
ORIENTADA PELO PROF. DR. MILTON DIAS JÚNIOR

.....
ASSINATURA DO ORIENTADOR

CAMPINAS
2014

Ficha catalográfica
Universidade Estadual de Campinas
Biblioteca da Área de Engenharia e Arquitetura
Rose Meire da Silva - CRB 8/5974

N729w Nomura, Paula Watanabe, 1983-
Wear analysis of bypass valves applied on regulated-two-stages turbocharger
/ Paula Nomura Watanabe. – Campinas, SP : [s.n.], 2014.

Orientador: Milton Dias Júnior.
Dissertação (mestrado) – Universidade Estadual de Campinas, Faculdade de
Engenharia Mecânica.

1. Desgaste mecânico. 2. Eixos. 3. Automóveis - Motores -
Turbocompressores. I. Dias Junior, Milton, 1961-. II. Universidade Estadual de
Campinas. Faculdade de Engenharia Mecânica. III. Título.

Informações para Biblioteca Digital

Título em outro idioma: Análise de desgaste de válvulas de bypass aplicadas a turbocompressores de dois estágios regulados.

Palavras-chave em inglês:

Mechanic wear

Shaft

Vehicle - Engine - Turbocharger

Área de concentração: Mecânica dos Sólidos e Projeto Mecânico

Titulação: Mestra em Engenharia Mecânica

Banca examinadora:

Milton Dias Júnior [Orientador]

Kátia Lucchesi Cavalca Dedini

Ruis Camargo Tokimatsu

Data de defesa: 04-07-2014

Programa de Pós-Graduação: Engenharia Mecânica

UNIVERSIDADE ESTADUAL DE CAMPINAS
FACULDADE DE ENGENHARIA MECÂNICA

COMISSÃO DE PÓS-GRADUAÇÃO EM ENGENHARIA MECÂNICA
DEPARTAMENTO DE SISTEMAS INTEGRADOS

TESE DE MESTRADO

Wear analysis of bypass valves applied on regulated-two-stages turbocharger

Análise de desgaste de válvulas de bypass aplicadas a turbocompressores de dois estágios regulados

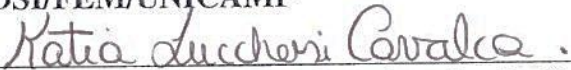
Autora: Paula Nomura Watanabe

Orientador: Milton Dias Júnior

A Banca Examinadora composta pelos membros abaixo aprovou esta Tese:



Prof. Dr. Milton dias Júnior, Presidente
DSI/FEM/UNICAMP



Profa. Dra. Kátia Lucchesi Cavalca Dedini
DSI/FEM/UNICAMP



Prof. Dr. Ruis Camargo Tokimatsu
DEM/FEIS/UNESP

Campinas, 04 de julho de 2014.

Abstract

The new emission legislations demand, from vehicle manufactures the development of technologies to improve fuel consumption and pollutants emission. Following this trend, the turbocharging systems innovate together and release new turbocharger architectures in the market. One of them is the regulated-two-stages turbocharger, which optimizes the efficiency in a broader engine speed range. In this system, there are two turbochargers, the high and low pressure stages. The former has a bigger influence on the low engine speeds, and the latter in the higher engine speeds. Between both stages there is a bypass valve that controls the gas flow to the low pressure stage, avoiding overpressure in the high pressure stage. This bypass valve is composed by a rotating shaft and a fixed bushing, and exactly between these two components it was detected wear, increasing the clearances and causing gas leakage. In order to reduce this leakage and solve the problem, an investigation about this premature wear has started inside the company where the author of the present dissertation works. In the present work the force analysis of the static and dynamic conditions that involve the shaft and bushing, the forces and momentum to open and close the valve plate, and the equations of motion are presented. The experimental analysis includes measurements made on two real engines: one of them connected to a dynamometer and the other installed on a vehicle used on the same application where the excessive wear was observed. Also, the wear analysis of ten shafts and bushings returned from durability tests is presented. The wear comparison between two shaft-bushing systems was performed. Both systems run in the same condition except for the control valve operational frequency, so the influence of this frequency could be evaluated. In the end, this entire data base collected could be used as input to a wear rate calculation that evaluates the influence of different design parameters on the wear rate.

Key Words: Wear, shaft and bushing, Turbocharger.

Resumo

As novas legislações de emissões demandam das montadoras de veículos automotores, o desenvolvimento de tecnologias para melhorar o consumo de combustível e emissão de poluentes. Seguindo esta tendência, os sistemas de turbocompressores inovam junto e lançam ao mercado novas arquiteturas de turbos. Uma delas é o turbocompressor regulado de dois estágios, que otimiza a eficiência em um intervalo de rotação mais amplo. Neste sistema, há dois turbocompressores: o estágio de baixa pressão e de alta pressão. O primeiro tem maior influência nas baixas rotações, enquanto o segundo nas altas rotações do motor. Entre os dois estágios, existe uma válvula bypass que controla a passagem do gás de escape para o estágio de baixa pressão, evitando assim, sobrecarregar o estágio de alta pressão. Esta válvula bypass é composta por um eixo rotativo e uma bucha fixa, e exatamente entre estes dois componentes foi detectado desgaste, aumentando as folgas e causando vazamento de gás. Com o objetivo de diminuir este vazamento e resolver o problema, uma investigação sobre este desgaste prematuro foi iniciada dentro da empresa onde a autora da presente dissertação trabalha. Neste trabalho a análise de forças das condições estática e dinâmica que envolve a bucha e o eixo, as forças e momentos para abrir e fechar o prato da válvula, e as equações de movimento são apresentadas. A análise experimental inclui medições feitas em dois motores reais: um deles conectado a um dinamômetro e o outro instalado em um veículo usado na mesma aplicação onde o desgaste excessivo foi observado. Além disso, a análise de desgaste de dez pares bucha-eixo que retornaram de testes de durabilidade é apresentado. A comparação do desgaste entre dois sistemas de bucha e eixo foi realizada. Ambos os sistemas rodaram na mesma condição, exceto pela frequência de operação da válvula de controle, assim a influência desta frequência pôde ser analisada. Ao final, todo este dado foi coletado e usado para o cálculo de taxa de desgaste que avalia a influência de diferentes parâmetros de design sobre a taxa de desgaste.

Palavras chave: Desgaste, eixo e bucha, Turbocompressor.

TABLE OF CONTENTS

1	OBJECTIVE AND MOTIVATION	1
2	BIBLIOGRAPHIC REVIEW	3
3	THE TURBOCHARGER	6
	3.1 REGULATED-TWO- STAGES – R2S SYSTEM.....	8
	3.2 Bypass valve	9
4	THEORETICAL MODEL.....	10
	4.1 Wear Rate	11
	4.2 Force Analysis	14
	4.2.1 Actuator Force	16
	4.2.2 Exhaust Gas Force	20
	4.2.3 Forces Distribution	20
	4.3 Natural frequency calculation.....	23
5	EXPERIMENTAL PROCEDURE I – VEHICLE AND ENGINE MEASUREMENTS	27
	5.1 Engine measurements – Dynamometer test.....	29
	5.2 Vehicle measurements	40
6	EXPERIMENTAL PROCEDURE II – WEAR ANALYSIS	51
	6.1 Wear parameters	53
	6.2 Wear comparison between two control valve systems	60
	6.3 Semi-ellipse adaptation.....	62
	6.4 Wear rate calculation based on measurements	65
7	CONCLUSION AND FUTURE WORKS PROPOSALS	68
	7.1 Conclusions.....	68
	7.2 Future Works Proposals.....	70
	References.....	72
	APPENDIX A – MATLAB FILES	74
	APPENDIX B – WEAR MEASUREMENTS	82

I dedicate my dissertation work to my parents, husband and to beloved expected son.

Acknowledgments

I would like to express the deepest appreciation to Professor Dr. Milton Dias Júnior, who always received me in a good mood to listen to the challenges I bring him, and patiently instructed how to proceed, to analyze, and to see the problem in a more academic way.

To the colleagues from Integrated Systems Department - UNICAMP for the tips, good advises and patience to share their experiences with me.

I would like to thank BorgWarner for consenting to use the experimental data base, my director Lauro Takabatake who gave me total freedom to accomplish this master studies and all the BorgWarner colleagues who directly or indirectly contributed to this work.

A special thanks to Alysson, who helped me every time I was lost, with his great know-how, academic experience, program knowledge, study methodology or simple with a comfortable talk.

My mother Nanami and my father Cláudio, my reason for keep studying. My twin sister Natália and brother Gustavo, who turn my life always happier.

Thanks to my husband Burts who was constantly beside me to motivate when I didn't believe I could continue, his encouragement words were very important. Without him, I would not have gotten here. To my baby Kenzo who behaved very well during all pregnancy allowing me to spend hours working on the thesis and specially for not coming earlier than expected.

*“All things are difficult before they are easy”
(Thomas Fuller)*

List of Figures

Figure 1.1 - Brazilian emission legislation	1
Figure 1.2 - Wear between bushing and shaft.	2
Figure 2.1 - Pressure distribution in three dimensions. Reproduced from Nayak and Johnson.	4
Figure 3.1 - The turbocharger. Reproduced from BorgWarner.	7
Figure 3.2 – Regulated-two-stages turbocharger. Reproduced from BorgWarner.	8
Figure 3.3 - a) bypass valve with actuator. b) actuator schematics.	9
Figure 3.4 - Bypass valve pressed in the turbine housing.	10
Figure 4.1 - Shaft and Bushing contact. Reproduced from Dickrell & Sawyer.	11
Figure 4.2 - Shaft diameter variation. Reproduced from Dickrell & Sawyer.	12
Figure 4.3 - Bushing diameter variation. Reproduced from Dickrell & Sawyer.	13
Figure 4.4 - Exhaust and actuator forces on the system.	15
Figure 4.5 - Forces on Valve and plate assembly.	15
Figure 4.6 - bypass valve closed position.	16
Figure 4.7 - Actuator rod inclination γ	17
Figure 4.8 - Actuator rod inclination schematic.	18
Figure 4.9 - Schematic forces acting on the bypass valve.	21
Figure 4.10 - Schematic forces of complete system.	24
Figure 5.1 - Measurement points in the vehicle.	28
Figure 5.2 - Actuator displacement.	28
Figure 5.3 - Engine speed measured during dynamometer test.	29
Figure 5.4 - Actuator displacement – dynamometer test.	30
Figure 5.5 - Actuator displacement histogram - dynamometer test.	30
Figure 5.6 - Actuator cumulative histogram - dynamometer test.	31
Figure 5.7 - Actuator displacement waterfall - dynamometer test.	31
Figure 5.8 - Actuator pressure - dynamometer test.	32
Figure 5.9 - Actuator pressure histogram - dynamometer test.	32
Figure 5.10 - Actuator pressure cumulative histogram - dynamometer test.	33
Figure 5.11 - Actuator pressure waterfall - dynamometer test.	33
Figure 5.12 - Actuator force components.	34
Figure 5.13 - Percentage of Fact components.	34
Figure 5.14 - Exhaust gas pressure - dynamometer test.	35
Figure 5.15 - Exhaust gas pressure histogram - dynamometer test.	36
Figure 5.16 - Exhaust gas pressure cumulative histogram - dynamometer test.	36
Figure 5.17 - Exhaust gas pressure waterfall - dynamometer test.	37
Figure 5.18 - Exhaust gas force components.	37
Figure 5.19 - Valve opening angle (Beta).	38
Figure 5.20 - Percentage of exhaust gas force components.	38
Figure 5.21 - Resultant forces in the X direction – dynamometer test.	39
Figure 5.22 - Resultant force in the Y direction - dynamometer test.	39
Figure 5.23 - Engine speed- vehicle test.	40
Figure 5.24 - Actuator displacement - vehicle test.	41

List of Figures

Figure 5.25 - Actuator displacement histogram - vehicle test	41
Figure 5.26 - Actuator displacement cumulative histogram - vehicle test.	42
Figure 5.27 - Actuator displacement order map - vehicle test.....	43
Figure 5.28 - Actuator pressure - vehicle test.	43
Figure 5.29 - Actuator pressure histogram - vehicle test.	44
Figure 5.30 - Actuator pressure cumulative histogram - vehicle test.	44
Figure 5.31 - Actuator pressure waterfall - vehicle test.....	45
Figure 5.32 - Actuator pressure order map - vehicle test.	45
Figure 5.33 - Actuator force components- vehicle test.....	46
Figure 5.34 - Percentage of actuator force components - vehicle test.	46
Figure 5.35 - exhaust pressure - vehicle test.....	47
Figure 5.36 - Exhaust pressure histogram - vehicle test.	47
Figure 5.37 - Exhaust pressure cumulative histogram - vehicle test.	48
Figure 5.38 - Exhaust pressure order map - vehicle test.....	48
Figure 5.39 - Exhaust gas force components - vehicle test.	49
Figure 5.40 - Valve opening position (Beta) - vehicle test.....	49
Figure 5.41 - Percentage of exhaust force components - vehicle test.	50
Figure 5.42 - Resultant force in X direction - vehicle test.....	50
Figure 5.43 - Resultant force in Y direction - vehicle test.....	51
Figure 6.1 - Universe of vehicles analyzed.	52
Figure 6.2 – Fixing device for wear measurement.	53
Figure 6.3 – (a) Shaft and (b) bushing wear measurement. Truck T4.2.	54
Figure 6.4 – (a) Shaft and (b) bushing wear area bounded for each wear depth. Truck T4.2.	55
Figure 6.5 – Bushing wear length vs depth.	55
Figure 6.6 – Shaft wear area vs wear depth. Truck T4.2.	56
Figure 6.7 – Bushing wear area vs wear depth. Truck T4.2.	56
Figure 6.8 – Shaft cumulative wear volume vs wear depth. Truck T4.2.	57
Figure 6.9 – Bushing cumulative wear volume vs wear depth. Truck T4.2.	57
Figure 6.10 – Shaft circumference axis. Truck T4.2.	58
Figure 6.11 – Bushing circumference axis. Truck T4.2.	58
Figure 6.12 – Shaft length axis. Truck T4.2.	59
Figure 6.13 – Bushing length axis. Truck T4.2.	59
Figure 6.14 – Shaft wear measurements. (a) 21Hz and (b) 150Hz PWM control valve.	60
Figure 6.15 – Shaft wear rate comparison: 21Hz and 150Hz PWM control valve.	61
Figure 6.16 – Bushing wear measurements. (a) 21Hz and (b) 150Hz PWM control valve.	61
Figure 6.17 – Bushing wear rate comparison: 21Hz and 150Hz PWM control valve.	62
Figure 6.18 – Bushing wear curve level and adapted ellipse. Truck T4.2.	63
Figure 6.19 – T 4.1 Adapted semi-ellipse area errors for each wear level. Truck T4.2.	63
Figure 6.20 - Area semi-ellipse error overview	64
Figure 6.21 - Wear rate comparison - different bushing design parameters.	66
Figure 6.22 – Bushing - % comparison between different design parameters.	66

List of Figures

Figure 6.23 - Wear rate comparison - Different shaft design parameters.	67
Figure 6.24 - Shaft - % comparison between different design parameters.	67

List of Abbreviations

Latin Letters

$\mathbf{A}(\mathbf{l}, \mathbf{t})$ – Contact area	[mm ²]
A_A – Actuator diaphragm area	[mm ²]
A_V – Valve plate area	[mm ²]
\mathbf{c} - Actuator counterforce from lever pin	[mm]
\mathbf{d}_{act} - Lever length	[mm]
$\mathbf{F}(\mathbf{z}, \mathbf{t})$ – Resultant force	[N]
\mathbf{F}_{act} - Actuator force	[N]
\mathbf{F}_{actX} - Actuator force in the X direction	[N]
\mathbf{F}_{actY} - Actuator force in the Y direction	[N]
\mathbf{F}_{P3} - Exhaust gas force	[N]
\mathbf{F}_{P3X} - Exhaust gas force in the X direction	[N]
\mathbf{F}_{P3Y} - Exhaust gas force in the Y direction	[N]
\mathbf{F}_{spring} - Spring force	[N]
\mathbf{h}_1 – Actuator rod final length minus h_2	[mm]
\mathbf{h}_2 – Length from the actuator to the shaft center line	[mm]
\mathbf{h}_n – Bushing internal radius at cycle n	[mm]
$\Delta\mathbf{h}_n$ – Change in bushing internal radius at cycle n	[mm]
\mathbf{k} - Spring coefficient	[N/mm]
\mathbf{K}_b - Bushing wear coefficient	[mm ³ /Nm]
\mathbf{K}_S - Shaft wear coefficient	[mm ³ /Nm]
\mathbf{L} – Bushing length	[mm]
\mathbf{L}_i – Actuator rod initial length	[mm]
\mathbf{l}_w – Wear depth	[mm]
\mathbf{m}_A – Actuator rod mass	[kg]
\mathbf{n} – Rod displacement	[mm]
\mathbf{P}_3 – Exhaust gas pressure	[mbar]

List of Abbreviations

P_{act}	– Actuator pressure	[mbar]
P_n	– Uniform pressure	[N/mm ²]
R	– Shaft radius	[mm]
R_0	– Initial shaft radius	[mm]
Res_x	– Resultant Force in the X direction	[N]
Res_y	– Resultant Force in the Y direction	[N]
R_n	– Shaft radius at cycle n	[mm]
ΔR_n	– Change in shaft radius at cycle n	[mm]
z	– Contact length	[mm]
zm	– Wear length at each level	[mm]

.....

Greek letters

α	– Contact angle	[degree]
β	– bypass valve opening angle	[degree]
γ	– Actuator rod angle	[degree]
θ	– wear angle	[degree]

.....

Abbreviations

- HP** - High Pressure
- LP** - Low Pressure
- PWM** - Pulse-Width-Modulation
- R2S** - Regulated-two-stages

.....

1 OBJECTIVE AND MOTIVATION

The demanding automotive market requires continuous improvement on combustion engines in order to reduce fuel consumption and increase lifetime. Besides that, the increasing pollution levels in the urban centers forces governments to tight emission legislations.

Following the worldwide trend, the Brazilian emission legislations have, over time, reduced the acceptable limit of the main pollutants like carbon monoxide, mono-Nitrogen oxide and particulate matter, as can be seen in Figure 1.1. These legislations have motivated the development of new technologies regarding to the complete vehicle chain, involving all components related to engine and vehicle, including the turbocharger, which is one of the possible solutions to achieve these challenging targets.

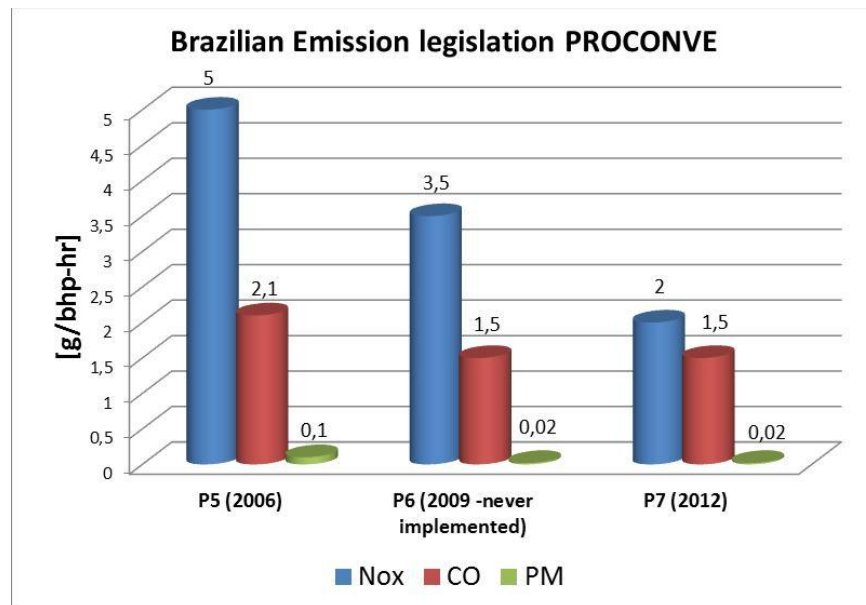


Figure 1.1 - Brazilian emission legislation

Turbochargers compress air into the engine cylinders, supplying more oxygen to the same volume compared to a natural aspirated engine. This guarantees more complete combustion, and in consequence less pollutants.

In order to fulfill the 2012 restricted emission limits, a new turbocharging system called regulated two-stages turbocharger was developed focusing the thermodynamic optimization. This

turbocharger architecture is most applied in addressing performance targets demanding aggressive boost and/or optimized efficiency in a wide engine speed range. A small turbocharger, optimized for the lower engine speeds, is connected in series with a bigger turbocharger, which brings more advantages at higher engine speeds. A bypass valve is responsible for controlling the operation between the two stages of the turbocharger.

The bypass valve is the component under study in this dissertation. Composed by an oscillating shaft and a fixed bushing, it receives forces from a pneumatic actuator to open and close the bypass channel, allowing exhaust gas coming from the smaller turbocharger to flow to the bigger one, covering a broader engine speed range.

Wear between the shaft and bushing of bypass valves was detected, increasing the clearance and causing exhaust gas leakage. The consequence is power loss, which is very critical to the final customer. Figure 1.2 shows an example of clearance between shaft and bushing that causes gas leakage. The objective of this dissertation is to analyze the wear and propose solutions to minimize it.



Figure 1.2 - Wear between bushing and shaft.

This work can be divided in two parts: theoretical and experimental analysis. The first one is the development of an extended formulation to calculate the wear rate based on a restricted model that does not include (among other assumptions) the cylinder length and in consequence the force distribution along it. In order to calculate this force distribution, the force analysis of the static and dynamic conditions that involve the shaft and bushing was performed, as well as the calculation of the forces and momentum to open and close the valve plate, and the equations of motion. Recognized the forces acting on the system, a linear force distribution along the shaft was considered as hypothesis and introduced in the wear rate formulation.

From the equation of motion, it was possible to calculate the system natural frequency to evaluate the possibility of resonance problem.

The second part is based on experimental analysis of two types: measurements on real engines and wear measurements of ten shaft and bushings based on dimensional data of parts returned from durability tests.

The measurements on real engines were performed on a dynamometer test bench and a vehicle representative of the application. In both cases, exhaust gas pressure, actuator pressure, actuator displacement and engine speed were recorded, because these are the parameters needed to calculate the forces acting on the shaft and bushing system.

The wear measurement of the components, which returned from durability test, was performed in precise tridimensional equipment and processed into image for more detailed evaluations. From these data, some wear parameters were calculated: wear area, length, width and depth.

The wear parameters of two pairs of shaft and bushing were compared, the only difference between both was the operational frequency of the control valve that commands the bypass. So the influence of this frequency on the wear could be evaluated. It was also investigated the possibility to predict wear by adapting semi-ellipses parameters in the wear curves measured from the shafts and bushings.

In the end all data from the experimental analysis could be used as input to the extended wear rate formula developed for general cases. This formula could also be modified with different design parameters to observe their influence on the wear rate.

2 BIBLIOGRAPHIC REVIEW

This work analyzes the wear region between shaft and bushing of bypass valves and the forces acting on them. As the wear area depends on the contact between two cylindrical components: the shaft and bushing, a research about cylinder contact was performed. Wear rate calculation and models were also investigated. There are several wear studies in the industry

about ball bearings and gears, but the description here will be limited to the ones with similar application to the problem under study in this dissertation.

(Johnson, 1987) and later on (Ciavarella & Decuzzi, 2000) propose the contact area calculation between cylindrical surfaces varying with pressure and cycle, with elastic similar materials. It gives a more elaborated closed form solution to cylindrical bodies in frictionless contact with elastic similar materials considering different clearances. They interpret the influence of contact parameters to the pressure distribution and strength of contact. One year later a computational algorithm was published (Ciavarella & Decuzzi, 2001) for the part I from their study.

For a realistic contact area calculation, (Nayak & Johnson, 1979) present a numerical calculation for the pressure distribution and contact area shape of a slender area between two elastic bodies, considering the pressure distribution linear along the length and semi-elliptical across the section, whose width is also very small in comparison to the length. The elastic displacement along the axis contains the contact width, which is a function of the elliptic distribution of pressure in the transversal direction, as seen in Figure 2.1.

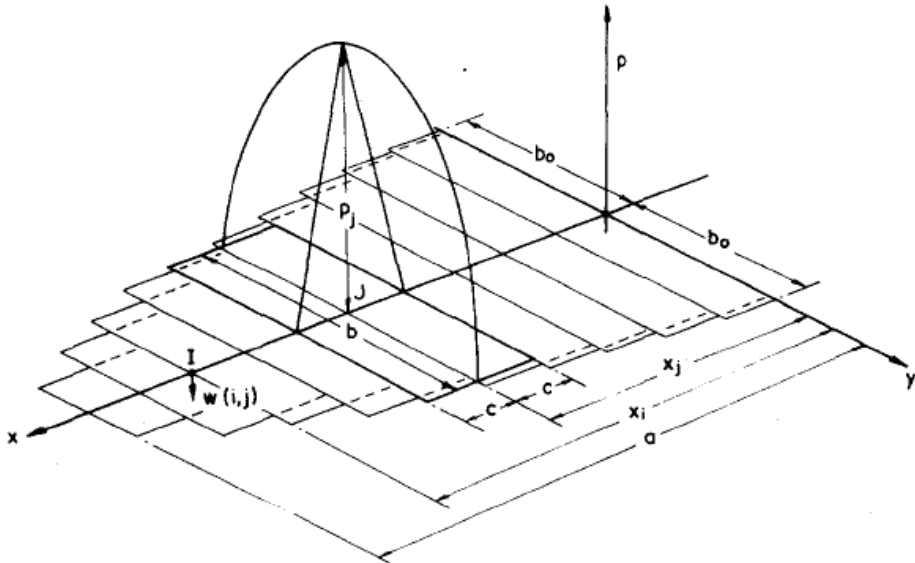


Figure 2.1 - Pressure distribution in three dimensions. Reproduced from Nayak and Johnson.

A numerical validation was done on smooth and continuous bodies, and also for cylindrical, crowned rollers and ball bearings, which present risen stress concentration on the edges. Satisfactory results were obtained only on points without stress concentration.

The main difficulty to calculate the contact area is to predict its shape in the outset, when the initial area is a Hertzian ellipse. This paper is restricted to contact areas where the width is smaller than the length and the transverse profiles are circular arcs.

(Ahmadi, Keer, & Mura, 1983) develop an iterative method using rectangular subdivisions, which includes shear force and emphasizes the profile of the edge to find the contact area between two smooth and elastic bodies under normal load. The numerical results had a great agreement with the analytical Hertz solution, and were applied on various situations as for miss- and aligned cylinders, friction, frictionless and conical cylinder.

(Kunert, 1961) proposes a mathematical solution to calculate the stress distribution between two elastic bodies, considering the contact area. He uses the half-space theory to characterize the pressure distribution as elliptical in the cross section and constant in the length direction. Using Businessq solution, the first integration gives the line load over the length. The second integration calculates the load over a rectangular area, and the third integration reveals the stress distribution from the rectangular area over its thickness depending on the distance to the contact surface.

Regarding wear, there are several models proposed for different cases, and wear rate calculations: (Dickrell & Sawyer, 2004) present one model based on the hypothesis of linear wear per shaft rotation cycle. This model considers the shaft has unitary length, performs complete revolutions at each cycle and there is uniform contact pressure with constant applied load.

A model for contact wear of radial journal bearing in outer space is proposed by (Aleksandrov, Bronovets, & Soldatenkov, 2008) based on the integration of wear rate. The model considers variations of wear conditions (and wear rate, consequently) induced by a sinusoidal pattern of temperature. It is applied to coated shafts and bushings operating mechanical parts of orbiting satellites, and as such, subjected to large temperature variations caused by different solar radiation. Cyclic changes in wear conditions are modeled through Fourier series expansion and elliptic integrals are included in the wear model.

An extensive work from (Williams, 1999) presents different methods of predicting, calculating and analyzing wear, depending on the application, measurements, kind of wear and

material available. In his paper, there is a list of the pros and cons of each methodology, what is involved, and how to interpret the results. But the work concludes that wear in condition of sliding contacts cannot follow an universal mechanism of wear, because of a complex correlation between wear rate, degradation and wear coefficient.

Adding complexity to wear models, wear particles may be considered to increase friction and local normal load to the contact, as published by (Mosleh, Saka, & Suh, 2002). Another parameter that can be added to the wear rate is the heat transfer due to friction between shaft and bushing during oscillating motion, this was presented by (Wen & Khonsari, 2009). They used Finite Element simulation for the thermo mechanical, contact and transient heat transfer analysis. A detailed description of each step until the thermally induced seizure is given, illustrated by the simulation results.

(Dine, Cromer, & Calabrese S. J., 1996) created a system dynamic model using commercial software tools for multi-body dynamical analysis to predict wear of complex machinery with sliding contacts. Wear prediction was confronted with wear measurements and retrofitted to the model. Different design parameters and material change were than investigated to check the effectiveness to reduce wear rate.

The wear rate calculation from (Dickrell & Sawyer, 2004) will be analyzed in detail in the next chapters, considering a more generic point of view and also merging some other parameters of different papers summarized here.

3 THE TURBOCHARGER

An overall explanation about the principles of the turbocharger, the regulated two-stages turbocharger and the bypass valve is given in order to clarify how the component that is presenting wear works, what are the functions, and what are the interfaces between the bypass valve and the complete system.

The turbocharger shown in Figure 3.1 is a mechanical component applied to combustion engines with the main objectives of increasing the output power, reducing the engine emissions

and decreasing the fuel consumption. In normal aspirated vehicles, an average of 40% of total fuel energy is dissipated in the exhaust system. If a turbocharger is applied, part of this energy can be recovered to provide more boost.

The turbine takes advantage of the exhaust energy to spin a shaft which is mechanically coupled with a compressor stage. This compressor stage captures the atmosphere air from the air filter and compresses it into the cylinder engine. By pressurizing more air into the cylinders, the turbocharger allows the engine to optimize its efficiency, increasing the output power.

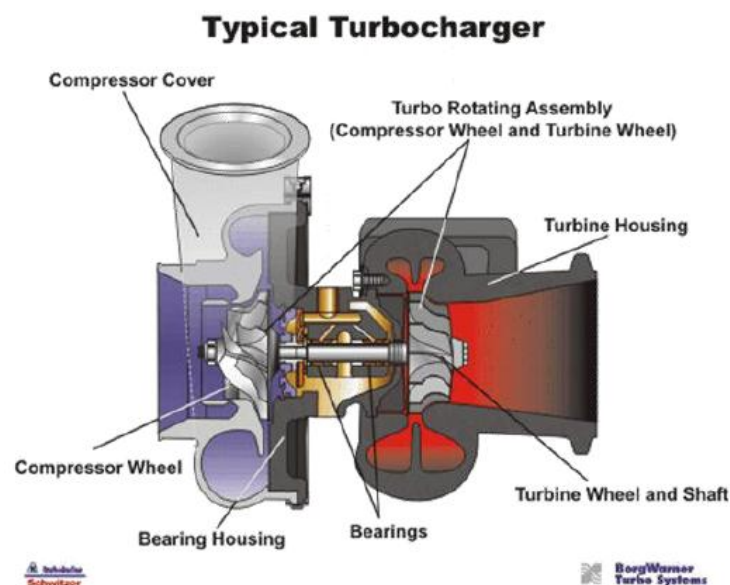


Figure 3.1 - The turbocharger. Reproduced from BorgWarner.

Upgraded technologies developed based on this classical concept of turbocharging have been greatly applied, especially on downsizing engines that aims building smaller engines without jeopardizing the power and still fulfilling the challenging new emission legislations.

The turbocharger is designed in a way that the most efficient thermodynamic behavior matches with the most important engine speeds for that application. For example, some city applications require optimized fuel consumption at low engine speeds, and the highway applications demand for a more efficient thermodynamic at higher engine speeds.

3.1 REGULATED-TWO- STAGES – R2S SYSTEM

The regulated-two-stages turbocharger consists of two turbochargers in series, a small one – called High Pressure stage (HP stage) –, responsible for the transient response at low engine speeds, and a bigger one – called Low Pressure stage (LP stage) –, that contributes at higher engine speeds. These architectures are most applied in addressing performance targets, demanding aggressive boost and/or optimized efficiency in a wide engine speed range.

There are different configurations of R2S systems: series sequential, parallel sequential, including fixed turbochargers, variable vanes, and different quantities of bypass valves. The one analyzed in this dissertation, illustrated in Figure 3.2, will be described in order to explain the overall function of the bypass valve, the component that presents wear and is under investigation here.

During low engine speeds, the bypass valve is closed, so the exhaust gas delivered by the engine flows into the HP turbine and after that into the LP turbine. On the compressor side, the air coming from the air filter goes through the first compression stage, at the LP compressor, and then follows to the HP compressor for the second compression stage.

At higher engine speeds, the system needs to bypass part of the HP turbine flow directly to the LP turbine, and this bypass is done by the bypass (or wastegate) valve, shown in Figure 3.2. This valve opens gradually, as the exhaust flow increases, controlling the turbocharger speed and compensating the energy between both stages.

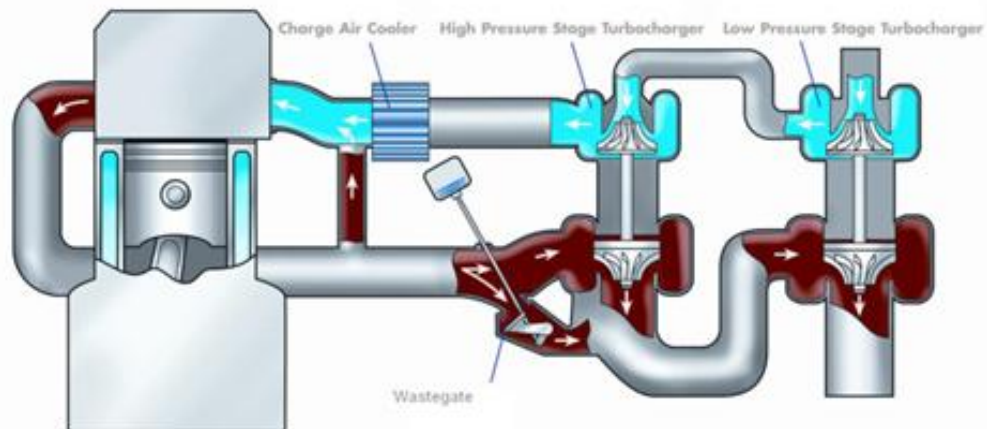


Figure 3.2 – Regulated-two-stages turbocharger. Reproduced from BorgWarner.

3.2 Bypass valve

The bypass valve has the main function to bypass the exhaust flow from the HP stage to the LP stage. In single stage turbo, this valve can bypass the exhaust flow from the turbine straight to the exhaust system, and that is the reason it is also called wastegate. This latter function is applied in order to control the maximum turbocharger speed, avoiding over speed failures.

The bypass valve is actuated by a pneumatic actuator (vacuum or pressurized) or by an electronic actuator. It depends on the precision, packaging and costs required. In this study case, a pneumatic actuator will be addressed. The working concept is simple: A PWM valve sends signal to a pressurized air valve to open and close at a certain frequency. The pressurized air coming from this valve is the input signal for the pneumatic actuator, which pushes a diaphragm; this diaphragm compresses a spring and pushes a rod, which has one end connected to the bypass valve assembly (see Figure 3.3).

The PWM valve has a regular interval or “period” of time, which is dictated by its operational frequency. The longer the switch is “on” compared to the “off” periods, the higher is the power supplied. This means that the PWM signal controls the valve plate opening angle by its pulse duration.

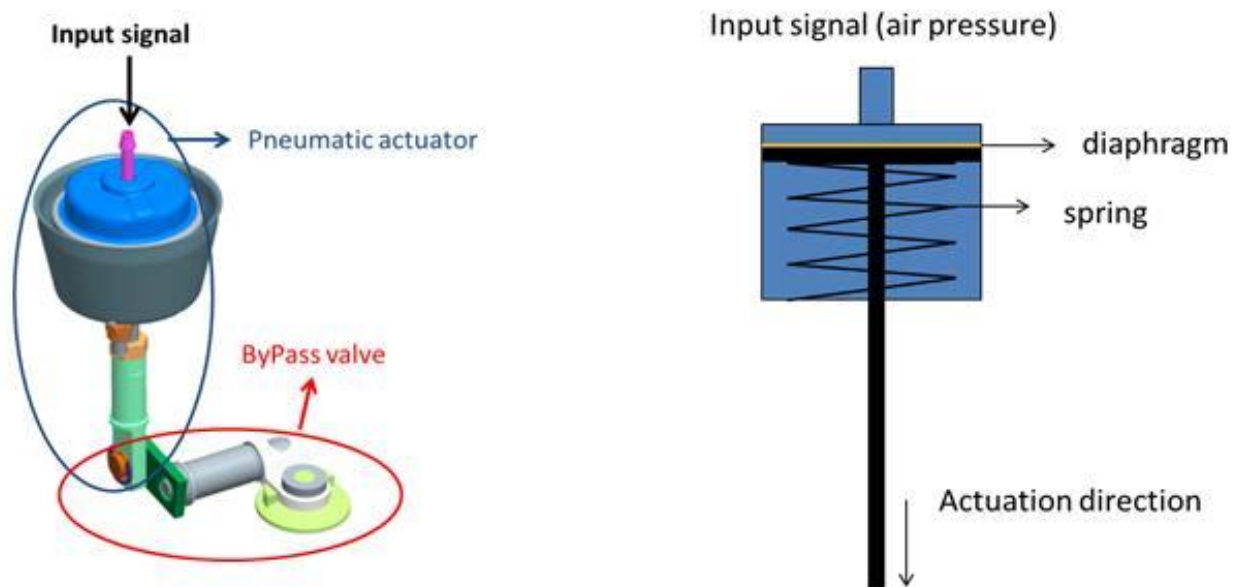


Figure 3.3 - a) bypass valve with actuator. b) actuator schematics.

The PWM operational frequency, as well as the overall engine (firing frequency) and vehicle vibration, are responsible for the bypass valve micro movements, called uncommand movement. This is the vibration that the bypass valve is subjected even when it is stopped at a certain angular position. On the other hand, commanded movement is the real action of opening and closing the bypass valve, which is driven by the duty cycle, the actual need to release or not the exhaust gas.

The bypass valve is pressed in the turbine housing as shown in Figure 3.4. This means that the bushing is static and the shaft oscillates back and forth to open and close the valve plate. The wear between these two components will be studied here in order to deep understand the root cause, critical application condition and possible design solutions.

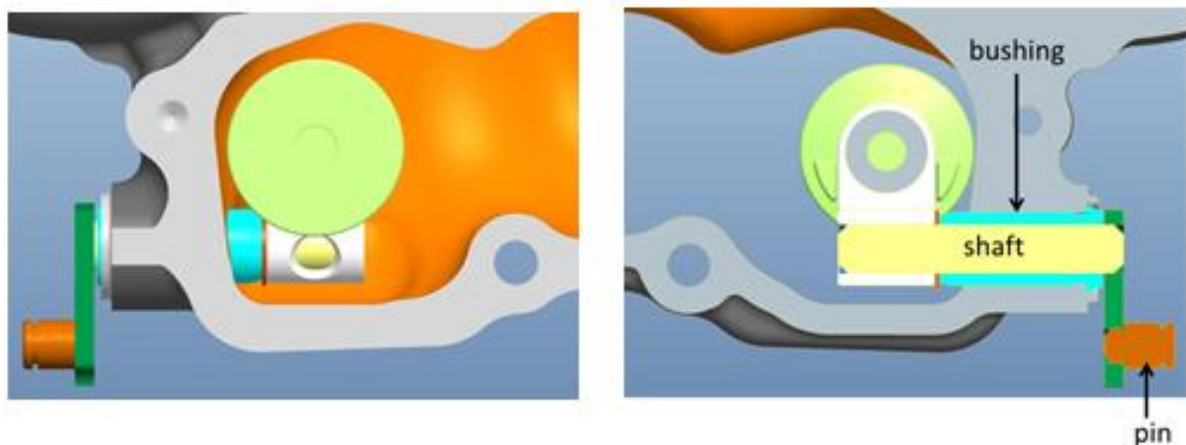


Figure 3.4 - Bypass valve pressed in the turbine housing.

4 THEORETICAL MODEL

In this chapter some theoretical calculations are made: it is presented the extension of the wear rate formula based on (Dickrell & Sawyer, 2004), analyzes and decomposition of the forces acting on the shaft and bushing including the force distribution along the shaft and the system natural frequency calculation.

4.1 Wear Rate

(Dickrell & Sawyer, 2004) used the assumptions of uniform contact pressure, constant applied load, unitary length and complete revolution to calculate the wear progression of a shaft moving inside the bushing, as illustrated in Figure 4.1, as a function of the number of cycles or time.

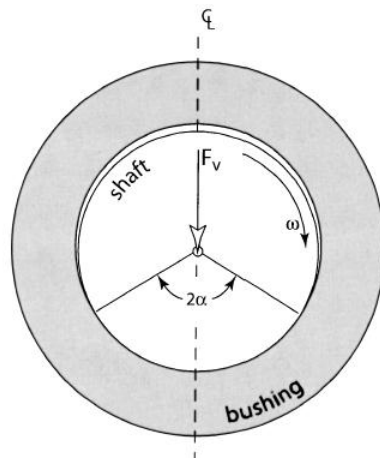


Figure 4.1 - Shaft and Bushing contact. Reproduced from Dickrell & Sawyer.

Not considering the friction effect at the interface, the shaft wear rate can be calculated as the integral of applied load multiplied by the wear rate over the contact length. Assuming the contact angle between the shaft and bushing is equal to 2α , the initial shaft radius is R_n , the pressure P_n is uniform, and the contact length is uniform and constant, the following formula from equation (4.1) can be used to calculate the shaft radius variation ΔR_n , where K_S [mm^3/Nm] is the wear rate of the shaft material and is not a function of cycle number neither time:

$$\Delta R_n = \int_0^{2\alpha R_n} K_S P_n ds = 2\alpha R_n P_n K_S \quad (4.1)$$

The physical representation of the shaft radius variation can be seen in Figure 4.2, where the dotted line represents the initial radius.

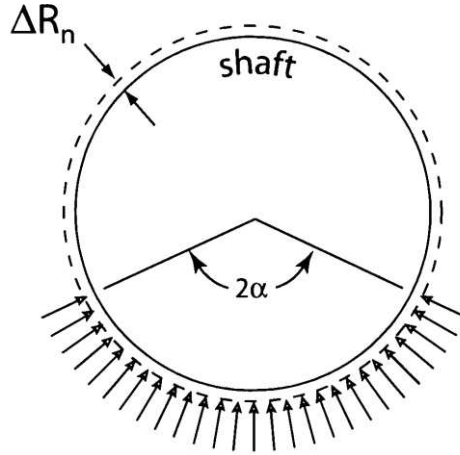


Figure 4.2 - Shaft diameter variation. Reproduced from Dickrell & Sawyer.

For every cycle, the shaft radius R_{n+1} decreases ΔR_n in comparison to the previous radius R_n as equation (4.2):

$$R_{n+1} = R_n - \Delta R_n \quad (4.2)$$

So the final radius R_f will be the initial radius minus the number of cycles times shaft radius variation as in equation (4.3):

$$R_f = R_0 - n\Delta R_n \quad (4.3)$$

For the bushing wear, the sliding distance for each element in contact is $2\pi R_n$ and the bushing radius variation is given by Δh_n . Unlike the shaft, the bushing inner radius increases with wear as showed in Figure 4.3, the dotted line represents the initial radius.

The variation in the bushing radius is given by equation (4.4):

$$\Delta h_n = \int_0^{2\pi R_n} K_b P_n ds = 2\pi R_n P_n K_b \quad (4.4)$$

For every cycle, the bushing inner radius h_{n+1} increases Δh_n in comparison to the previous radius h_n as equation (4.5):

$$h_{n+1} = h_n + \Delta h_n \quad (4.5)$$

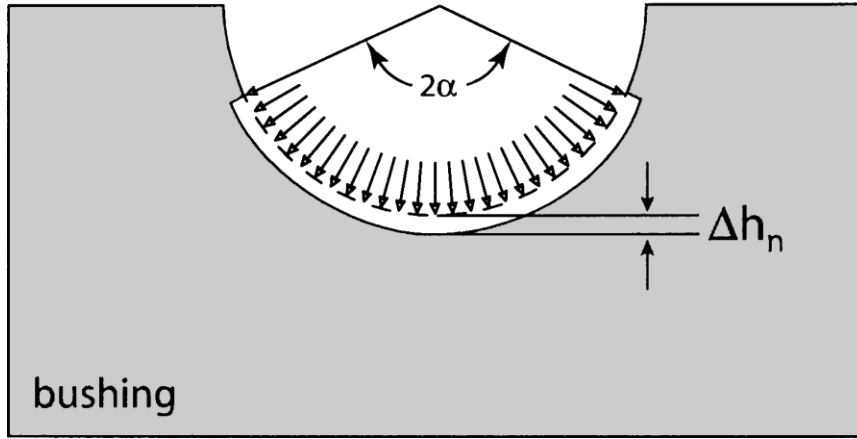


Figure 4.3 - Bushing diameter variation. Reproduced from Dickrell & Sawyer.

So the final bushing radius h_f will be the number of cycles times variation in bushing radius as in equation (4.6):

$$h_f = n\Delta h_n \quad (4.6)$$

The problem under study in this dissertation may not satisfy all the assumptions used by (Dickrell & Sawyer, 2004), which are restrictive to the study case applied. Therefore an amplified formulation to generalize the wear rate calculation is needed.

(Dickrell & Sawyer, 2004) equations may be adapted in order to contemplate new conditions. For a three-dimensional problem for example, the contact arc can be replaced by a contact area, so the shaft length must be considered.

In cases that the applied load is not uniform, a function of the force distribution along the shaft should be used. If the movement is oscillatory instead of complete revolution, than the wear concentrates in an arc and is not circumferentially regular. This arc can be expressed as the shaft radius average in the wear region R multiplied by the wear arc θ , which is not necessarily symmetric.

Adapting equation (4.1) for the generic case, the shaft/bushing length additional parameter results in a double integral of the applied force $F(z)$ in function of the length z divided by the contact area A , over the wear area, that means shaft radius R multiplied by wear angle variation $d\theta$ and wear length variation dz . As written in Equation (4.7).

$$\Delta \mathbf{R}_n = \iint \mathbf{K}_s \frac{F(z)}{A} \mathbf{R} d\theta dz \quad (4.7)$$

This equation is equivalent to (4.1) from (Dickrell & Sawyer, 2004), but \mathbf{P}_n is $\frac{F(z)}{A}$ and $d\mathbf{s}$ is $\mathbf{R}d\theta dz$.

4.2 Force Analysis

For the force analysis, several assumptions were considered: the bypass valve is a rigid body composed by the lever, the shaft and the valve plate. The system is a linear single degree of freedom without dumping, although there are clearances between the shaft and bushing, which could make the system be non-linear, this analysis is justified to give an idea about the linearized behavior.

Making a static analysis on the axes X and Y seen in Figure 4.4, the sum of the forces is equal zero, and the same for the resultant moment about the axes X and Y, so angular displacements are considered negligible. The only dynamic analysis is the moment about axis Z, which is the movement of opening and closing the valve.

There are two forces acting on the bypass valve: the exhaust gas force and the actuator force. Each one generating a moment on each end of the shaft. For any open position, both moments are in the same direction, about axis Z along the shaft and bushing, contributing to open the valve. When the valve is completely closed, the forces are acting parallel to the Y- direction, but when it is open, that means, angle β (Figure 4.5) is different than zero, the forces start acting in angle, so the X-component of the forces increase.

For an open position, the Y-components of the exhaust force (\mathbf{F}_{P3Y}) and of the actuator force (\mathbf{F}_{actY}) create the moment to open the valve, and their X components, \mathbf{F}_{P3X} and \mathbf{F}_{actX} are acting on the same axis of the shaft and bushing, not producing any moment.

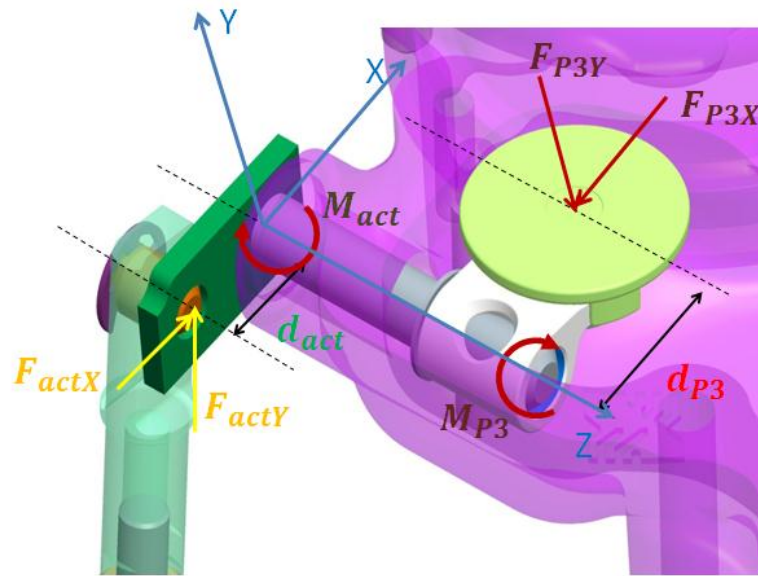


Figure 4.4 - Exhaust and actuator forces on the system.

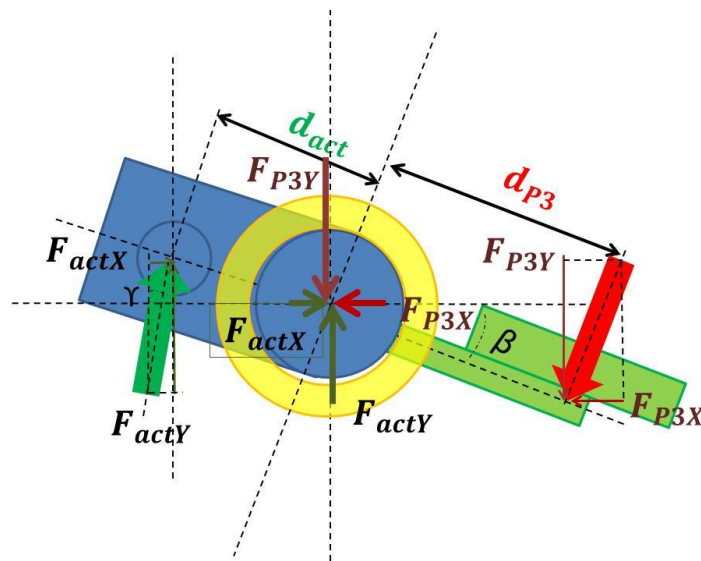


Figure 4.5 - Forces on Valve and plate assembly.

4.2.1 Actuator Force

It is possible to calculate the actuator force acting on the bypass valve from a known actuator inlet pressure. The schematic of the pneumatic actuator was showed previously in Figure 3.3. The actuator inlet pressure is distributed in the whole area of the actuator diaphragm, which pushes it in the displacement direction. Acting against this displacement, there is a spring with defined pre load in order to guarantee a minimum pressure to start movement.

In the closed position, demonstrated in Figure 4.6, there is an actuator force in the same direction of the exhaust force. In this case, both forces are pressing the shaft against the bushing. The moments of these two forces around the shaft are opposite to each other.

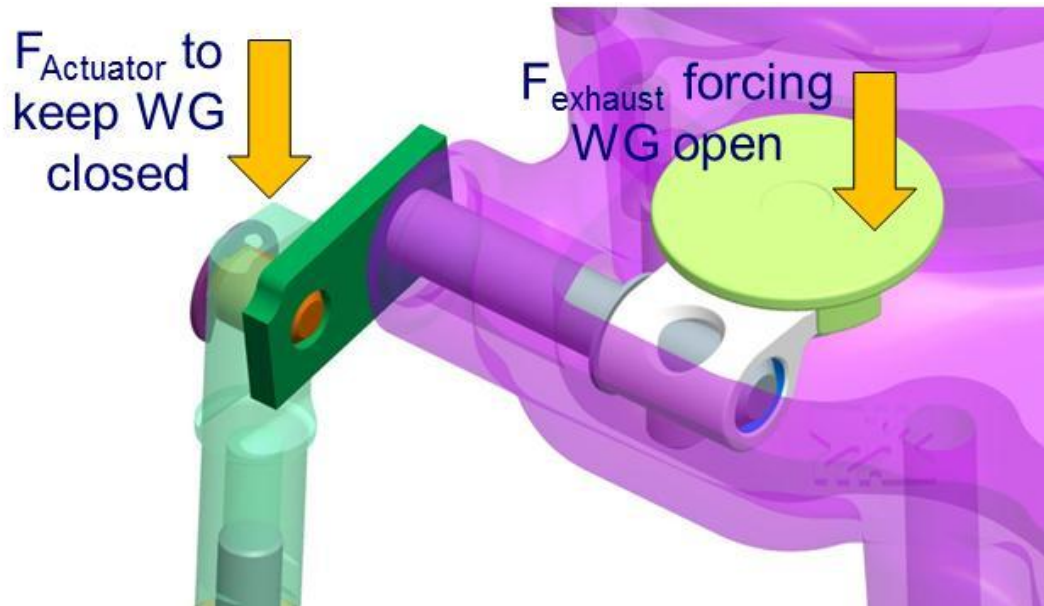


Figure 4.6 - bypass valve closed position.

For all open conditions, the actuator force is the measured actuator inlet pressure multiplied by the diaphragm area minus the spring force – the latter one considers the pre load and the spring displacement –, as given by equation (4.8). This is a static equation ignoring the push rod, spring and diaphragm masses.

$$F_{act} = P_{act} \cdot A_{diaphragm} - F_{spring} \quad (4.8)$$

In order to open the valve, the actuator rod displaces from the initial position to an elongated position, pushing the rigid body composed by lever connected to the shaft and the valve plate. The rod linear displacement causes a rotation in the shaft axis, opening the valve plate in an angle β .

At closed position, lever and actuator rod are perpendicular between them, but as the connection between rod and lever is not fixed, the angle between them varies with the lever angular position. The rod at open position generates an angle with its initial position. This angle is called γ and is illustrated in Figure 4.7.

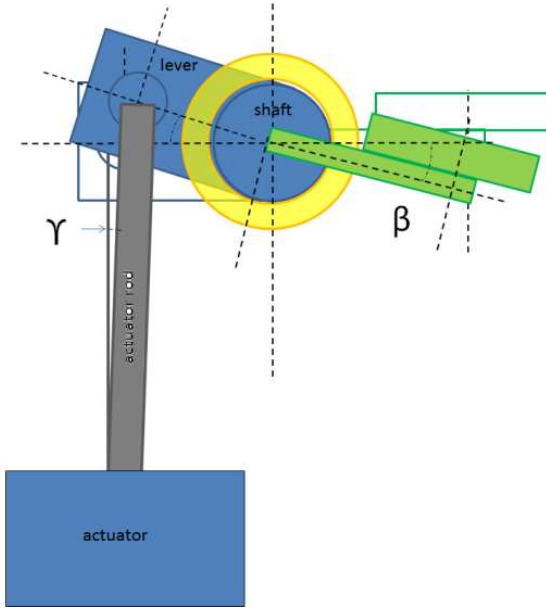


Figure 4.7 - Actuator rod inclination γ .

Figure 4.8 illustrates the actuator rod inclination schematic to explain the angle γ calculation. The connection between actuator rod and lever in the initial closed position is indicated as point **A**, aligned to the shaft center line, and as **A'** in the open position. The valve open position angle is β .

The intersection point between the shaft center line and the actuator rod in the open position is called point **D**. So h_2 is the distance between points **B** and **D**, and h_1 is the distance between points **D** and **A'**. The initial distance between the actuator (point **B**) and the shaft center line (x axis) is denominated L_i . The distance between point **B** and **A'** is the initial distance (L_i)

plus the actuator linear displacement n , that means $L_i + n$. So equation (4.9) can be used to express the distance between B and A' .

$$h_1 + h_2 = L_i + n \quad (4.9)$$

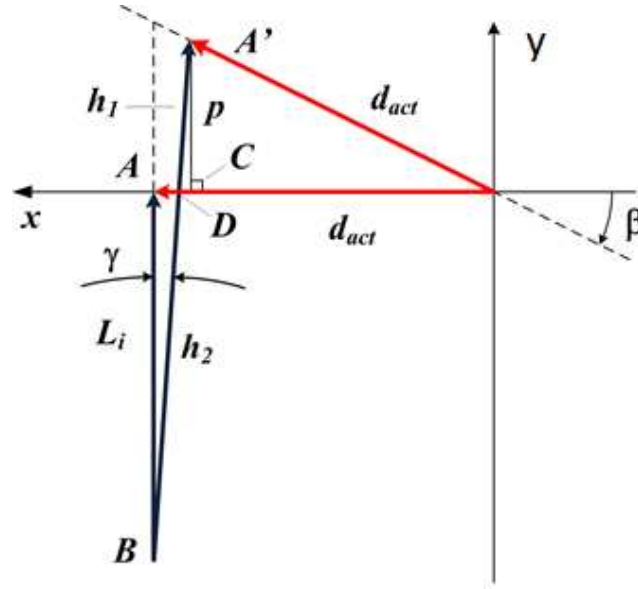


Figure 4.8 - Actuator rod inclination schematic.

The distance from C to A' is denominated p and is perpendicular to the shaft center line. C is on the x axis. The angle γ between rod closed position and rod open position is represented in Figure 4.8 as the angle between L_i and h_2 . So it can be calculated by the equation (4.10):

$$\cos\gamma = \frac{L_i}{h_2} \quad (4.10)$$

And another possibility to calculate angle γ is the equation (4.11):

$$\cos\gamma = \frac{p}{h_1} \quad (4.11)$$

Equalizing the two formulas for $\cos\gamma$, the equations (4.10) and (4.11) become equation (4.12):

$$\frac{p}{h_1} = \frac{L_i}{h_2} \quad (4.12)$$

In order to find p , equation (4.13) can be used, where d_{act} is the distance between the shaft center and A':

$$\sin\beta = \frac{p}{d_{act}} \quad (4.13)$$

Substituting p from equation (4.13) and h_1 from equation (4.9) in equation (4.12), it is possible to achieve equation (4.14):

$$\frac{\sin\beta d_{act}}{L_i + n - h_2} = \frac{L_i}{h_2} \quad (4.14)$$

Isolating h_2 from equation (4.14) in the first term, equation (4.15) is found:

$$h_2 = \frac{(L_i + n)L_i}{\sin\beta d_{act} + L_i} \quad (4.15)$$

Substituting h_2 in equation (4.10), angle γ can be finally calculated through equation (4.16)

$$\gamma = \cos^{-1} \frac{\sin\beta d_{act} + L_i}{(L_i + n)} \quad (4.16)$$

Once γ is known, the actuator force in X direction F_{actX} and in Y direction F_{actY} can be calculated as shown in equations (4.17) and (4.18).

$$F_{actX} = F_{act} \sin \gamma \quad (4.17)$$

$$F_{actY} = F_{act} \cos \gamma \quad (4.18)$$

The actuator displacement in the Y direction n_y can also be calculated as equation (4.19)

$$n_y = n \cos \gamma \quad (4.19)$$

4.2.2 Exhaust Gas Force

The exhaust gas force can be calculated from the exhaust gas pressure and actuator displacement measurements. The exhaust gas pressure coming from the engine enters the turbine housing and pushes the bypass valve plate illustrated in Figure 4.4 to try to open it. If the bypass valve is closed, this gas acts perpendicular to the valve plate. But if the valve plate is open to bypass the gas to the LP stage, then the exhaust gas force is perpendicular to the valve plate, but in angle β to the shaft, as seen in Figure 4.5. This angle is known from the Y component of actuator displacement measurement.

$$\beta = \frac{n_y}{d_{act}} \quad (4.20)$$

The force coming from the exhaust pressure F_{P3} , is computed by multiplying the valve plate area A_V by the exhaust pressure P_3 , as in equation (4.21).

$$F_{P3} = P_3 \cdot A_V \quad (4.21)$$

This force is then decomposed into the Y- direction F_{P3Y} and X-direction F_{P3X} for every different valve plate angular position β , as in equations (4.22) and (4.23).

$$F_{P3Y} = F_{P3} \cos\beta \quad (4.22)$$

$$F_{P3X} = F_{P3} \sin\beta \quad (4.23)$$

4.2.3 Forces Distribution

Both forces calculated before act on the shaft and bushing. The actuator force in one bushing end and the exhaust gas force in the opposite end. The force distribution along the bushing is unknown. One hypothesis is to consider it linear, as showed in Figure 4.9.

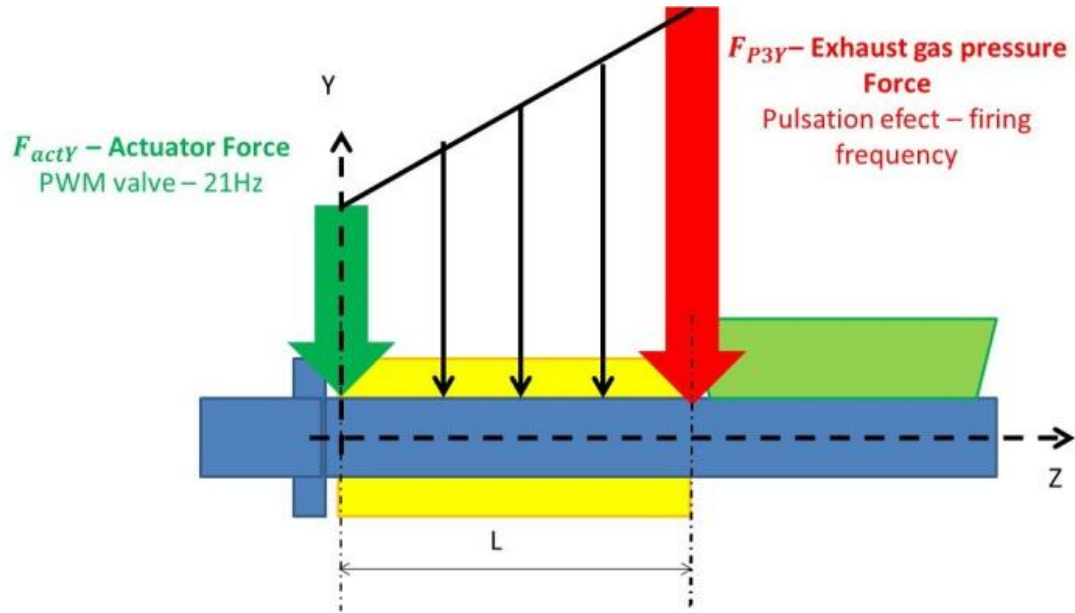


Figure 4.9 - Schematic forces acting on the bypass valve.

If the assumption of a linear force distribution is considered, the force equation development will follow the linear equation presented in equation (4.24), where m is the slope of the line and b is the y-intercept:

$$y = mz + b \quad (4.24)$$

The slope m is calculated then in equation (4.25), where L is the bushing length

$$m = \frac{F_{P3Y} - F_{actY}}{L} \quad (4.25)$$

If F_{actY} is the Y-intercept, the force function $F(z)$, can be calculated by replacing y from equation (4.24). This is shown in equation (4.26):

$$F(z) = F_{actY} + \left(\frac{F_{P3Y} - F_{actY}}{L} \right) z \quad (4.26)$$

Taking the amplified wear rate formula from equation (4.7), and replacing $F(z)$ by the force function given in equation (4.26), it is possible to calculate the wear rate of the shaft and bushing under study in this dissertation by equation (4.27):

$$\Delta R_n = \iint K_s \frac{F_{actY} + \left(\frac{F_{P3Y} - F_{actY}}{L}\right) z}{A} R d\theta dz \quad (4.27)$$

As the wear coefficient K_s , the contact area A and the shaft radius R are not function of z , neither θ . Than they can be removed from the integral as equation (4.28):

$$\Delta R_n = \frac{K_s R}{A} \iint F_{actY} + \left(\frac{F_{P3Y} - F_{actY}}{L}\right) z d\theta dz \quad (4.28)$$

The contour integral method says that:

$$\oint P d\theta + Q dz = \iint \frac{\partial Q}{\partial \theta} - \frac{\partial P}{\partial z} dz d\theta \quad (4.29)$$

Equalizing the term inside the double integral from equation (4.28) and the term inside the double integral from equation (4.29), equation (4.30) is found:

$$\frac{\partial Q}{\partial \theta} - \frac{\partial P}{\partial z} = F_{actY} + \left(\frac{F_{P3Y} - F_{actY}}{L}\right) z \quad (4.30)$$

If $\frac{\partial P}{\partial z}$ is equal to zero, then $\frac{\partial Q}{\partial \theta}$ is equal to the whole force function, as exhibited in equations (4.31) and (4.33):

$$\frac{\partial P}{\partial z} = 0 \quad (4.31)$$

$$\frac{\partial Q}{\partial \theta} = F_{actY} + \left(\frac{F_{P3Y} - F_{actY}}{L}\right) z \quad (4.32)$$

Integrating the equation (4.32), the first term of equation (4.29) is found:

$$\oint Q dz = \oint F_{actY} z + \left(\frac{F_{P3Y} - F_{actY}}{L}\right) \frac{z^2}{2} dz \quad (4.33)$$

Replacing the contour integral from equation (4.33) in equation (4.28), the result is equation (4.34):

$$\Delta R_n = K_s \frac{R}{A} \oint F_{actY} z + \left(\frac{F_{P3Y} - F_{actY}}{L}\right) \frac{z^2}{2} dz \quad (4.34)$$

Considering the contour of the wear symmetric from zero to a maximum length zm , the contour integral will be twice the integral from zero to zm , as indicated in equation (4.35)

$$\Delta R_n = K_s \frac{R}{A} 2 \int_0^{zm} F_{actY} z + \left(\frac{F_{p3Y} - F_{actY}}{L} \right) \frac{z^2}{2} dz \quad (4.35)$$

Solving the integral from equation (4.35), the shaft radius variation ΔR_n can be calculated by equation (4.36):

$$\Delta R_n = \Sigma K_s \frac{R}{A} \left[F_{actY} z^2 + 2 \left(\frac{F_{p3Y} - F_{actY}}{L} \right) \frac{z^3}{3} \right]_0^{zm} \quad (4.36)$$

Equation (4.36) will be used in another section to calculate the shaft radius variation using wear and forces parameters measured from the real application.

4.3 Natural frequency calculation

The bypass valve natural frequency is calculated in this section in order to check if it is influencing the wear due to the fact that the forces acting on the system are dynamic and can excite the bypass system. The complete system is considered for the natural frequency calculation, including actuator, lever, shaft and valve plate assembly as showed in Figure 4.10. From Newton's second law, equation (4.37) gives the sum of the forces in Y direction:

$$\Sigma F_y = m_A \ddot{n}_y. \quad (4.37)$$

Considering m_A the actuator rod mass, n_y the actuator rod displacement in the Y direction and the forces in the Y direction, as the actuator force, spring force and counter force, equation (4.37) can be rewritten as equation (4.38). Where actuator force is actuator inlet pressure multiplied by the diaphragm area $P_{act} A_A$, spring force is the spring rate multiplied by the displacement $2 \frac{k}{2} n_y$ and the counterforce is the force c coming from the valve plate system:

$$P_{act} A_A - 2 \frac{k}{2} n_y - c = m_A \ddot{n}_y \quad (4.38)$$

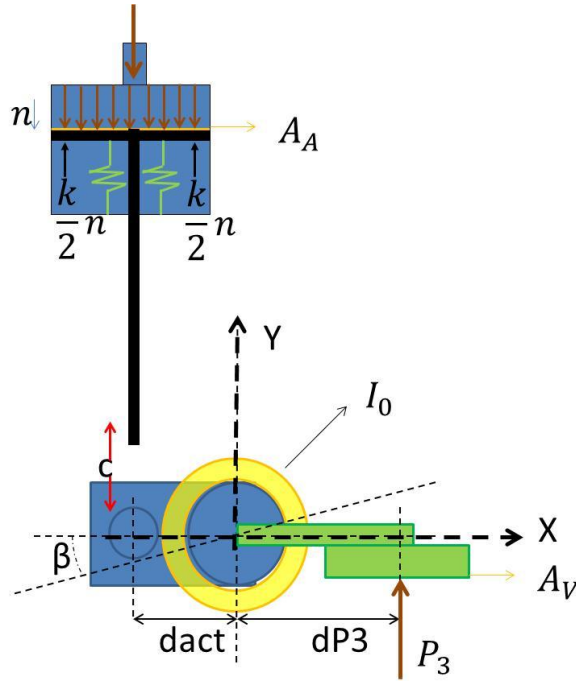


Figure 4.10 - Schematic forces of complete system.

Using Euler's equation to describe the rotation of a rigid body, equation (4.39) must be developed:

$$\Sigma M_0 = I_0 \ddot{\beta} \quad (4.39)$$

As stated before, the only dynamic analysis from this system is the moment about axis Z, caused by the actuator counterforce c and the exhaust gas force acting on the valve plate. Both generate a moment about the shaft axis as equation (4.40):

$$c d_{act} + P_3 A_V d_{P3} = I_0 \ddot{\beta} \quad (4.40)$$

The actuator force moment is $c d_{act}$, and the exhaust gas force moment is the exhaust gas pressure P_3 multiplied by the valve plate area A_V multiplied by the distance d_{P3} from the shaft center to the valve plate center. Isolating c from equation (4.38), substituting it in equation (4.40), it is possible to obtain equation (4.41):

$$(P_{act} A_A - k n_y - m_A \ddot{n}_y) d_{act} + P_3 A_V d_{P3} = I_0 \ddot{\beta} \quad (4.41)$$

From equation (4.20) is already known that the actuator displacement in the Y direction is given by equation (4.42):

$$\mathbf{n}_y = \mathbf{d}_{act}\boldsymbol{\beta} \quad (4.42)$$

And its second derivative is showed in equation (4.43):

$$\dot{\mathbf{n}}_y = \mathbf{d}_{act}\ddot{\boldsymbol{\beta}} \quad (4.43)$$

Substituting equations (4.42) and (4.43) in equation (4.41), the complete equation (4.44) is found:

$$\mathbf{P}_{act}\mathbf{A}_A\mathbf{d}_{act} - k\mathbf{d}_{act}^2\boldsymbol{\beta} - \mathbf{m}_A\mathbf{b}^2\ddot{\boldsymbol{\beta}} + \mathbf{P}_3\mathbf{A}_V\mathbf{d}_{P3} = \mathbf{I}_0\ddot{\boldsymbol{\beta}} \quad (4.44)$$

Grouping the terms from equation (4.44) in function of $\boldsymbol{\beta}$ and $\ddot{\boldsymbol{\beta}}$, the equation of motion of a single degree of freedom is obtained and written in equation (4.45):

$$(\mathbf{I}_0 + \mathbf{m}_A\mathbf{d}_{act}^2)\ddot{\boldsymbol{\beta}} + k\mathbf{d}_{act}^2\boldsymbol{\beta} = \mathbf{P}_{act}\mathbf{A}_A\mathbf{d}_{act} + \mathbf{P}_3\mathbf{A}_V\mathbf{d}_{P3} \quad (4.45)$$

Analyzing the homogeneous system associated that means forces (second term) are equal to zero and remembering that the equation of motion is differential, linear and has constant coefficients, it is convenient to propose a solution like:

$$\boldsymbol{\beta}(t) = \mathbf{a}e^{st} \quad (4.46)$$

And its second derivative is:

$$\ddot{\boldsymbol{\beta}}(t) = s^2\mathbf{a}e^{st} \quad (4.47)$$

Substituting equations (4.46) and (4.47) in equation (4.45) and resetting the forces, the characteristic equation (4.48) is given:

$$[(\mathbf{I}_0 + \mathbf{m}_A\mathbf{d}_{act}^2)s^2 + k\mathbf{d}_{act}^2]\mathbf{a}e^{st} = \mathbf{0} \quad (4.48)$$

In order to find a characteristic equation solution valid for every time t , equation (4.49) can be considered, as e^{st} is never zero.

$$[(\mathbf{I}_0 + \mathbf{m}_A\mathbf{d}_{act}^2)s^2 + k\mathbf{d}_{act}^2]\mathbf{a} = \mathbf{0} \quad (4.49)$$

The trivial solution occurs if $\mathbf{a} = \mathbf{0}$, but this is not desired once it represents no movement, so the characteristic polynomial from equation (4.50) is the only possibility:

$$(I_0 + m_A d_{act}^2) s^2 + k d_{act}^2 = 0 \quad (4.50)$$

Solving the characteristic polynomial, there are two solutions that can be written in terms of modal parameters like equation (4.51):

$$s_{1,2} = -\zeta \omega_n \pm j \omega_n \sqrt{1 - \zeta^2} \quad (4.51)$$

So the natural frequency of the bypass valve system can be calculated as equation (4.52):

$$\omega_n = \sqrt{\frac{k d_{act}^2}{I_0 + m_A d_{act}^2}} \quad (4.52)$$

Numerically calculating the natural frequency, the value found is 301.5Hz. This frequency does not match with the PWM valve operational frequency of 21Hz. The engine operates in the speed range of 0 to 3000rpm, has four cylinders, four-stroke, resulting in a firing frequency equals to two times the engine rotational speed, which is given by equation (4.53). That means that for every revolution there are two cylinders firing, which is a second order excitation. Calculating the engine maximum firing frequency, the value found is 100Hz, which is also out of the bypass valve natural frequency.

$$Firing\ Frequency = \frac{number\ of\ cylinders}{2} \times \frac{rpm}{60} \quad (4.53)$$

However, the 6th order on a 4 cylinder engine (the 2nd and the 4th are usually the most important) and the 4th order on 6 cylinder engine (the 3rd and the 6th are usually the highest ones) could actually excite the system.

There are two turbochargers in series in the studied engine, both of them run through the natural frequency of the bypass valve while accelerating. That means the operational frequency of the turbochargers matches with bypass valve natural frequency. Unfortunately this subject will not be covered in this study, but can be deeper researched as next step.

5 EXPERIMENTAL PROCEDURE I – VEHICLE AND ENGINE MEASUREMENTS

There were two sets of measurements, one performed in the engine dynamometer, and the other on vehicle. The difference between both is the cycle measured and the bypass control valve operational frequency. In both cases, the objective was to measure the exhaust gas pressure, actuator pressure and actuator displacement, so this data could be used to calculate the real forces acting on the shaft and bushing system.

The first set of measurements was performed in an engine dynamometer, on a 4 cylinders, 230hp engine running steady in steps from 2700rpm to 1100rpm. The pneumatic actuator was controlled by a 21Hz PWM valve and the data acquisition sampling frequency was set to 100Hz.

The second set of measurements was performed on a diesel truck fitted with a 4 cylinders turbocharged engine, which delivers 230hp. In this vehicle, the pneumatic actuator was controlled by a 150Hz PWM valve. The measured signals were recorded by a HBM eDaq data acquisition system using 1000Hz sampling rate. The acquired data were further analyzed using the SoMat Infield software and also the Matlab.

The measured track is a combined cycle of highway, uphill and downhill, very representative to the whole application cycle. The total track length is 132.6km and it requires a constant use of the bypass valve, once it needs to control the boost, especially during the uphill tracks.

In both cases (dynamometer and vehicle), there was a pressure transducer on the turbine inlet (P3) and another one in the actuator inlet (Pact), as shown in Figure 5.1, which is the same as Figure 3.2, but is repeated here in order to facilitate reading.

The interaction between the exhaust gas pressure and the actuator forces, considering the areas where they are applied, distance to the shaft, and all the parameters already discussed in chapter 4, generates an angular displacement on the valve plate position in direction of opening or closing it. This angular displacement could not be measured directly, but the linear displacement of the actuator rod was measured as indicated in Figure 5.2.

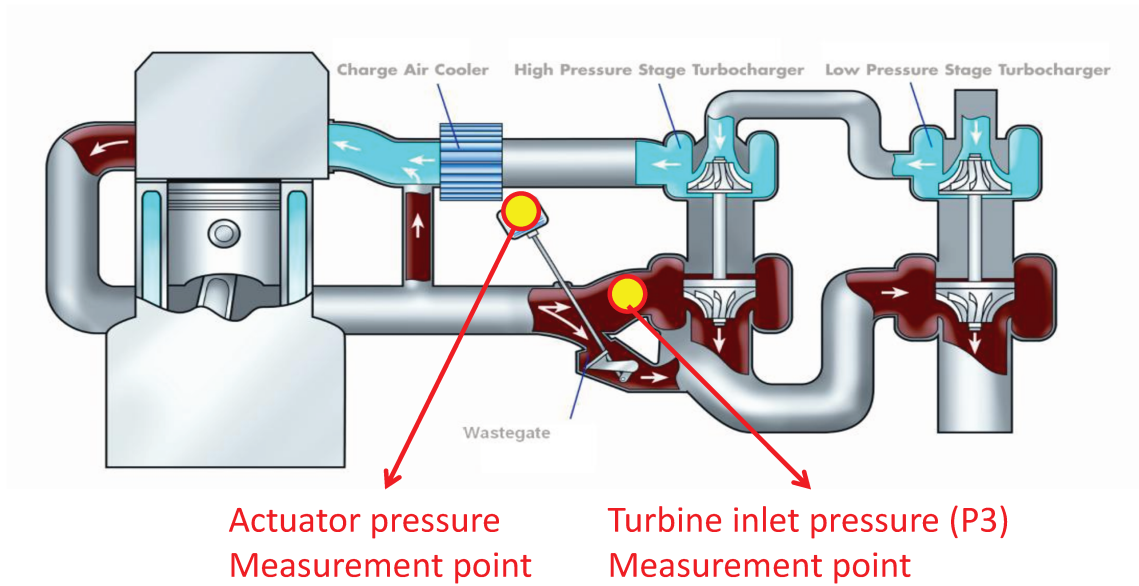


Figure 5.1 - Measurement points in the vehicle.

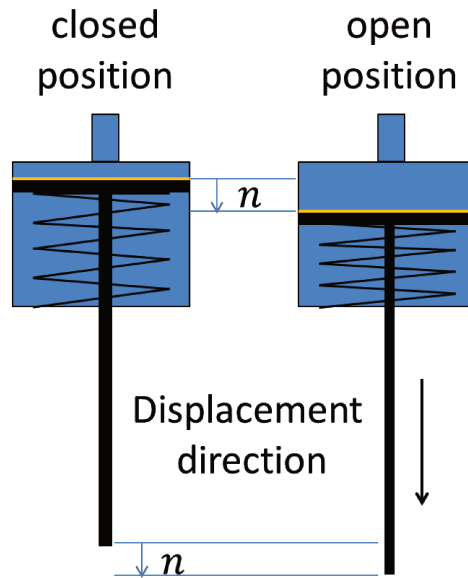


Figure 5.2 - Actuator displacement.

5.1 Engine measurements – Dynamometer test

As already mentioned, these measurements were performed in an engine dynamometer running from 2700 to 1100rpm in steps of 100rpm, as shown in Figure 5.3.

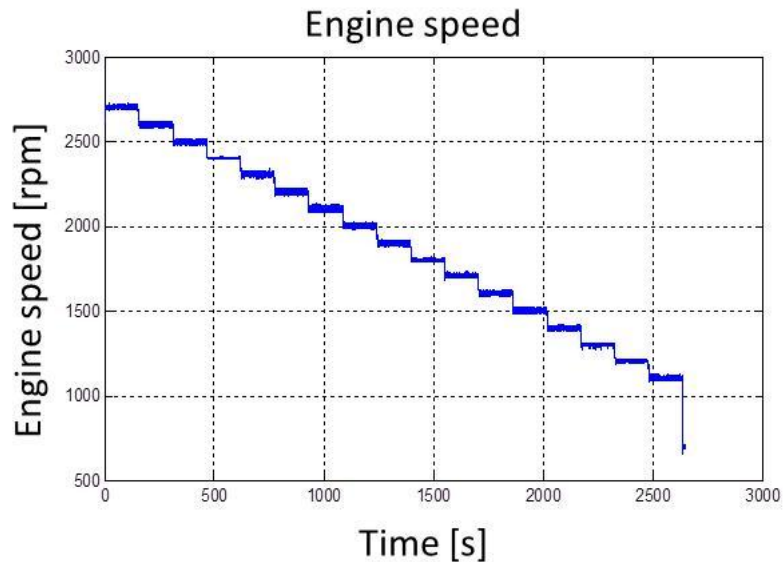


Figure 5.3 - Engine speed measured during dynamometer test.

The actuator displacement measurement plotted in Figure 5.4 shows that from 1500seconds on, the valve plate keeps mainly in the closed position, in this instant, the engine speed is about 1800rpm. The total displacement is, in average, very low, since the maximum actuator displacement is 10mm. Even at higher engine speeds and full load, the displacement does not increase, it is also possible to observe a big oscillation in the open positions.

The occurrence of each displacement level is shown in the histogram presented in Figure 5.5. A great number of displacements lower than 0.1mm call the attention. That represents almost 45% of the measurement time as cumulative histogram exhibited in Figure 5.6. That is related to the time interval from 1500 seconds until the end, when the bypass valve is forcing the closed position.

In order to know the frequency content of the actuator displacement signal, the waterfall plot was computed and the result is presented in Figure 5.7. As can be seen, a 21Hz component is clearly outlined, which corresponds to the PWM valve operation frequency. It is worth noting

that this frequency does not match with the actuator and valve plate system natural frequency, which is, as already presented in Chapter 4, 301.5Hz.

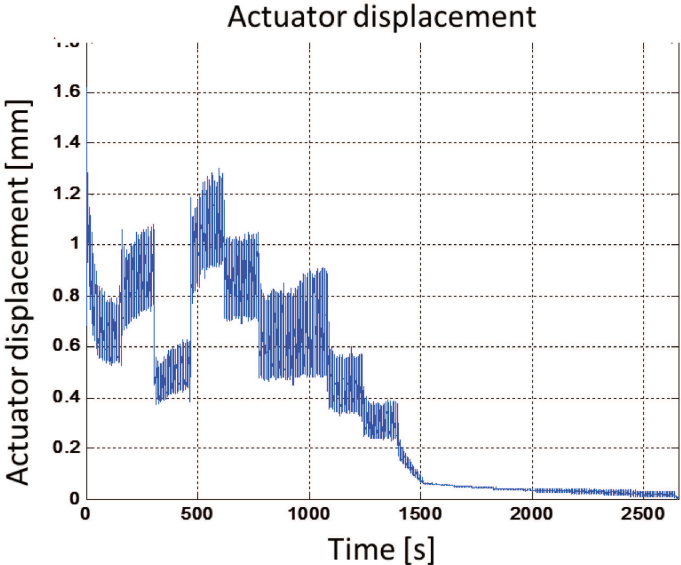


Figure 5.4 - Actuator displacement – dynamometer test.

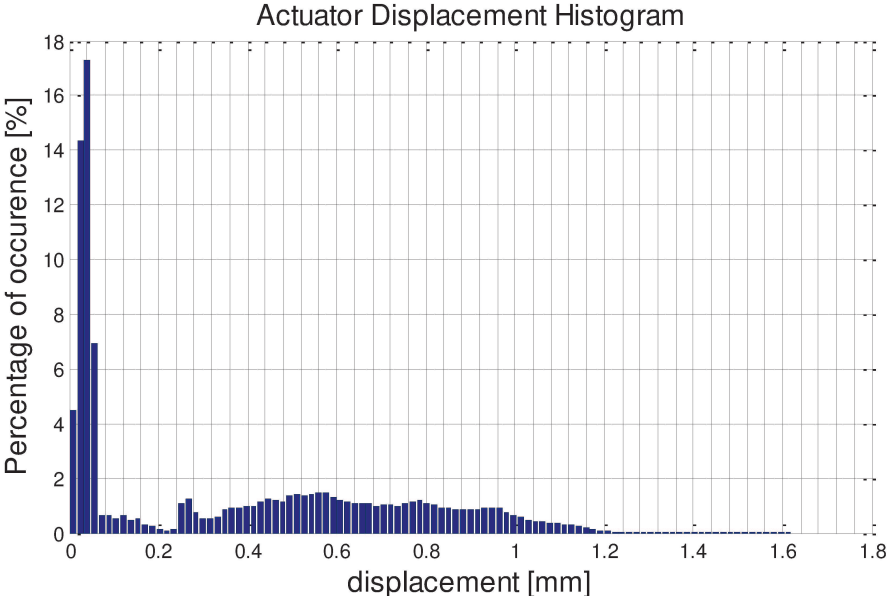


Figure 5.5 - Actuator displacement histogram - dynamometer test.

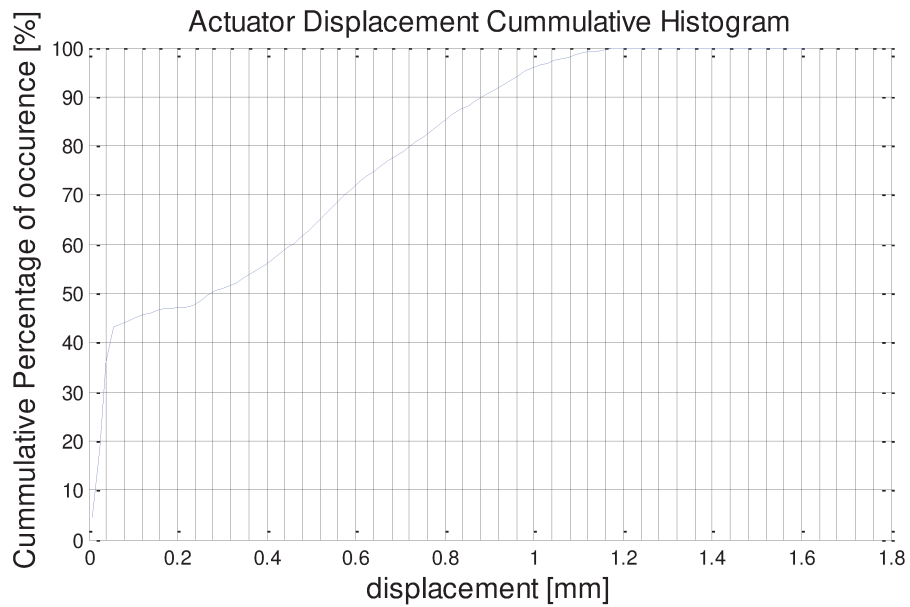


Figure 5.6 - Actuator cumulative histogram - dynamometer test.

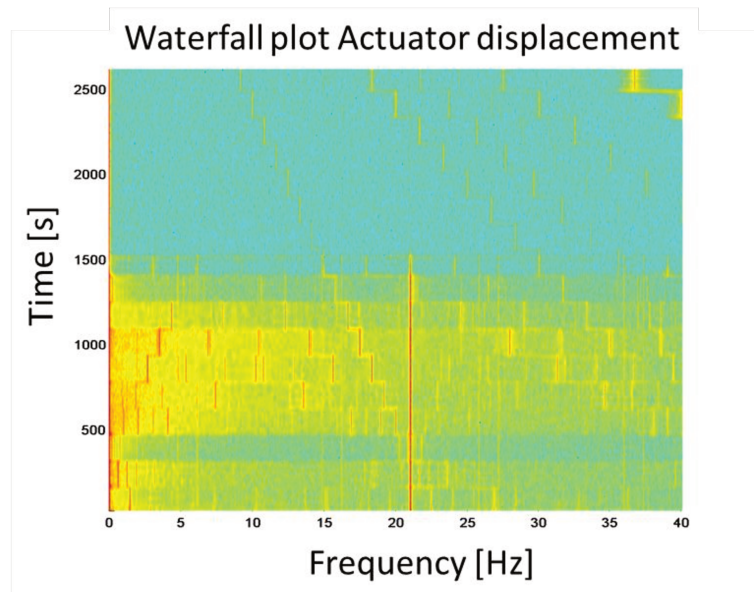


Figure 5.7 - Actuator displacement waterfall - dynamometer test.

The actuator pressure plotted over time in Figure 5.8 also shows a closed position of the valve plate from 1500 seconds on, and an oscillation around the open positions. That means that on engine speed lower than 1800rpm (from 1500 seconds on), the bypass valve is closed and only the HP stage Turbocharger is operating.

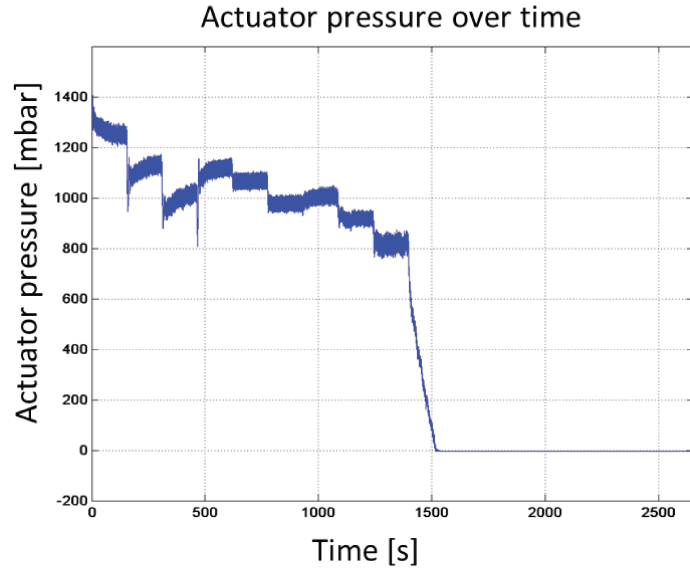


Figure 5.8 - Actuator pressure - dynamometer test.

The actuator pressure histogram seen in Figure 5.9 and cumulative histogram presented in Figure 5.10 show more than 40% of low pressure level occurrence, related to the closed position from 1500 seconds on.

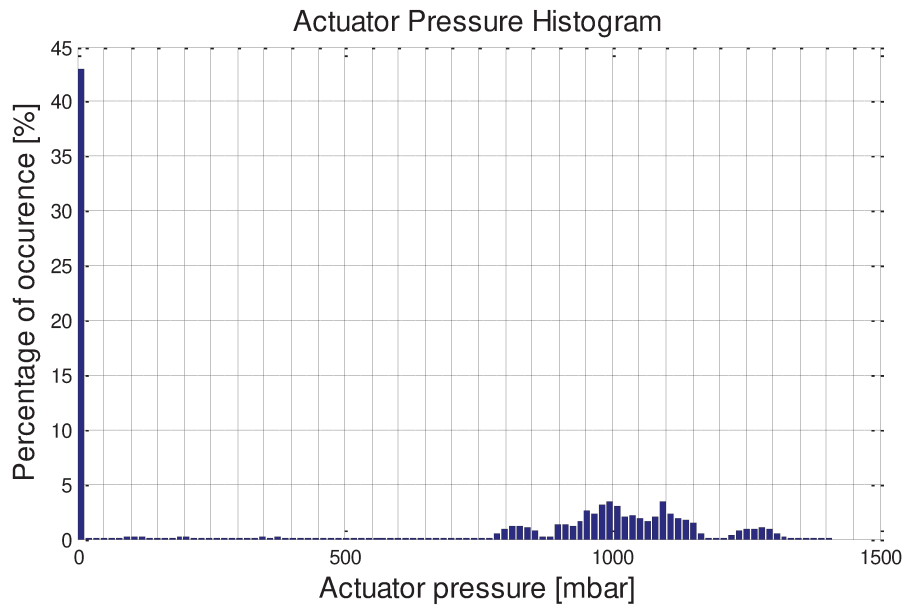


Figure 5.9 - Actuator pressure histogram - dynamometer test.

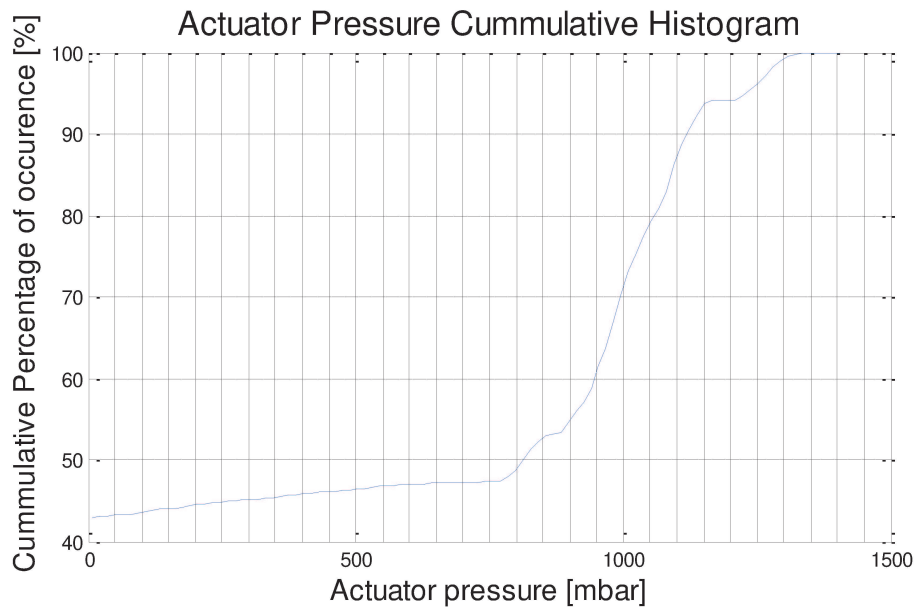


Figure 5.10 - Actuator pressure cumulative histogram - dynamometer test.

The 21Hz component of the PWM valve operation frequency can also be detected in the actuator pressure waterfall demonstrated in Figure 5.11. When the actuator is no longer operating, from 1500 seconds on, this frequency component vanishes from the signal and cannot be seen in the waterfall anymore. This is a great indicator that the 21Hz is really coming from the PWM valve.

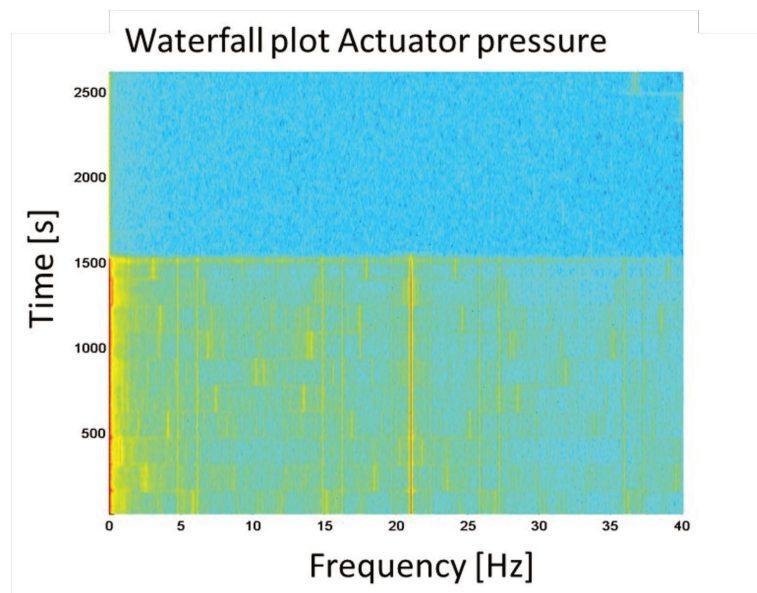


Figure 5.11 - Actuator pressure waterfall - dynamometer test.

In order to check the influence of components X and Y from actuator force over the shaft and bushing, F_{actX} and F_{actY} , where calculated based on equations presented in chapter 4.2.1. Using the measured actuator displacement and pressure, one can conclude that the F_{actX} is much smaller than the F_{actY} , as can be seen in Figure 5.12. In this case, the X-component does not reach 0.5% of the Y-component value, as exhibited in Figure 5.13.

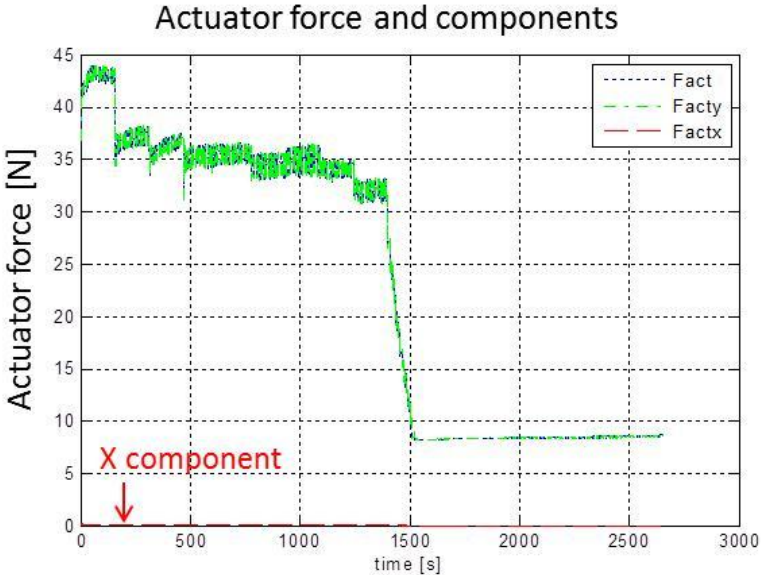


Figure 5.12 - Actuator force components.

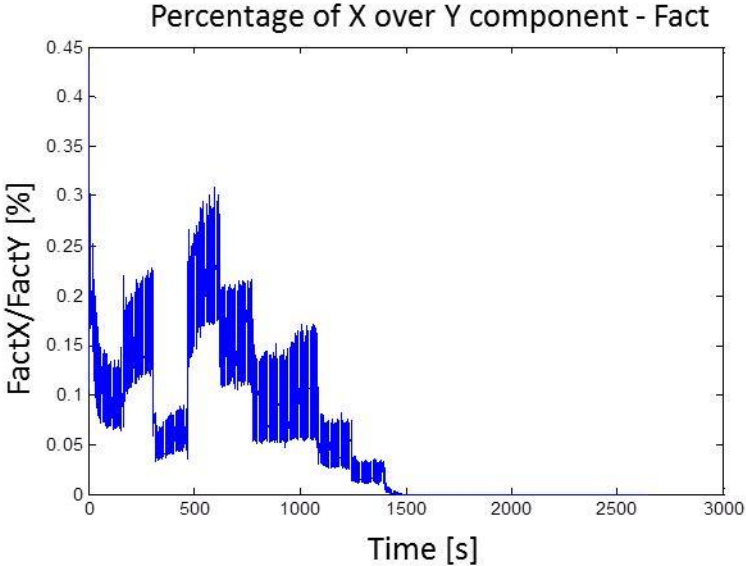


Figure 5.13 - Percentage of Fact components.

The exhaust gas pressure measurement is shown in Figure 5.14. From engine speed of 2700rpm to the maximum power of 2400rpm, the exhaust gas pressure does not follow the engine speed (decreasing each step). But from the rated power to the final speed, the exhaust gas pressure decreases proportional to the engine speed.

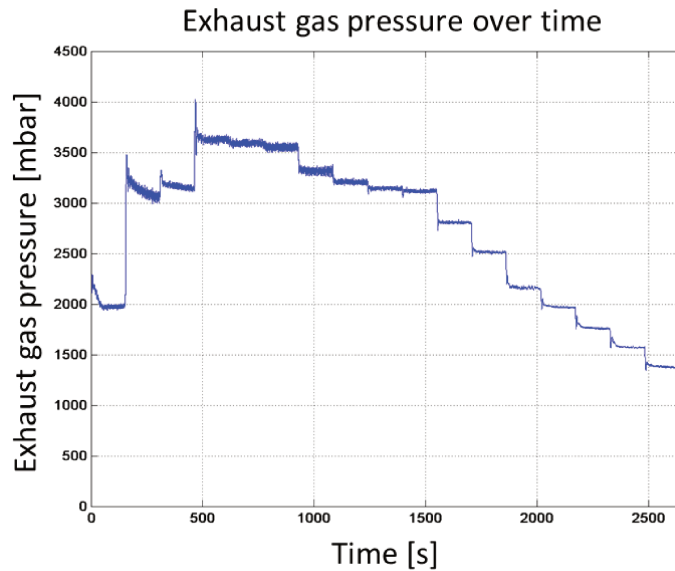


Figure 5.14 - Exhaust gas pressure - dynamometer test.

The behavior of exhaust gas pressure is very different from the actuator pressure, once its histogram and consequently its cumulative histogram, showed in Figure 5.15 and Figure 5.16, respectively, are well distributed over the complete range of amplitudes, and does not show high concentration in the lower pressure levels.

Analyzing the exhaust gas pressure waterfall shown in Figure 5.17, it is not possible to detect the 21Hz frequency component highlighted in the actuator pressure and displacement waterfalls, which supports the conclusion that this frequency is not related to the engine operation.

Analyzing the exhaust gas force components plotted in Figure 5.18, it is clear that the exhaust force component F_{P3Y} is much higher than the F_{P3X} component. That is because the valve opening angle β reaches a maximum of 3.5° , as shown in Figure 5.19. So the X component is not more than 6% of the Y component presented in Figure 5.20:

The resultant force in the X direction, $Res_X = F_{P3X} - F_{actX}$, plotted in Figure 5.21, is almost the same as the exhaust gas pressure due to the fact that the actuator force is almost zero.

The resultant force in the Y direction, $Res_Y = F_{P3Y} - F_{actY}$, plotted in Figure 5.22 is very similar to the exhaust force because the actuator component is very low in comparison to the exhaust force.

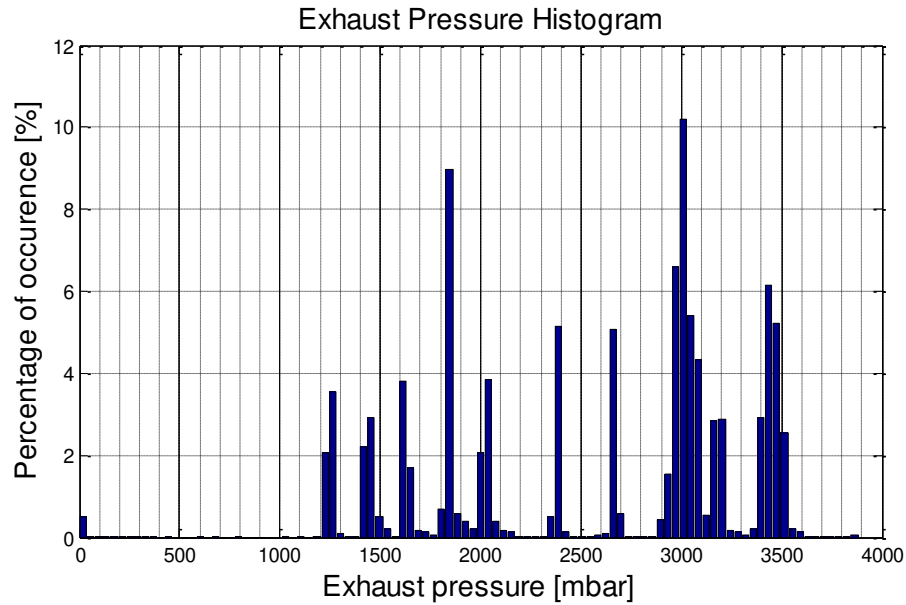


Figure 5.15 - Exhaust gas pressure histogram - dynamometer test.

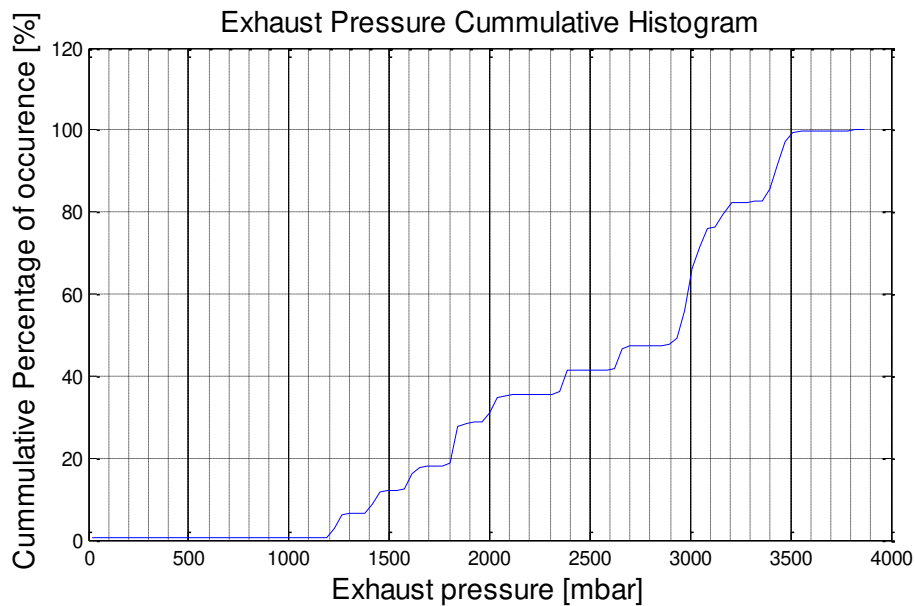


Figure 5.16 - Exhaust gas pressure cumulative histogram - dynamometer test.

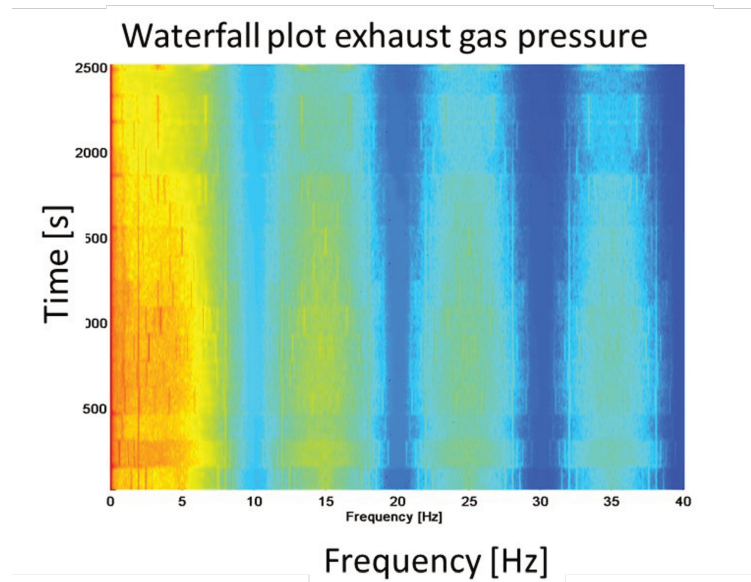


Figure 5.17 - Exhaust gas pressure waterfall - dynamometer test.

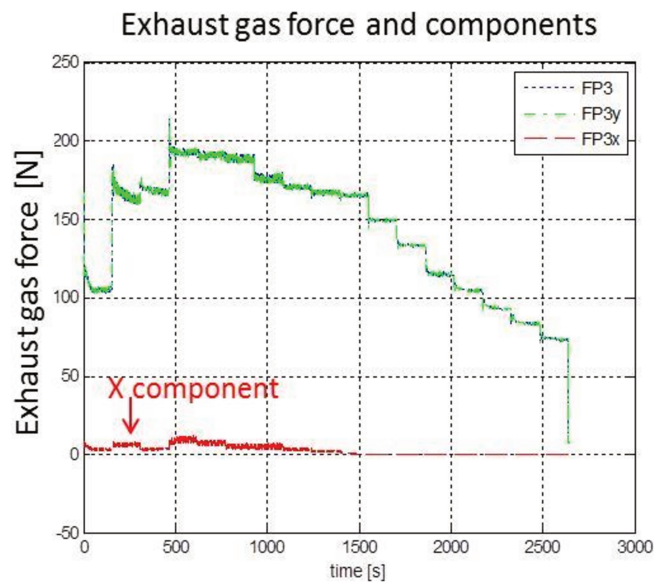


Figure 5.18 - Exhaust gas force components.

From this dynamometer engine test, assembled with a 21Hz PWM valve, it is possible to conclude that there is a great concentration of micro movements lower than 0.1mm in the actuator displacement measurements. A 21Hz frequency is detected in the actuator displacement and pressure waterfall graphics, but not in the exhaust gas pressure measurements. This frequency matches with the PWM valve operation frequency.

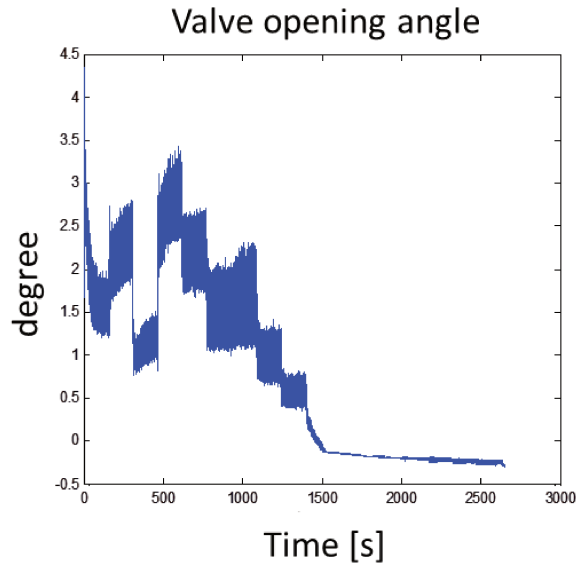


Figure 5.19 - Valve opening angle (Beta).

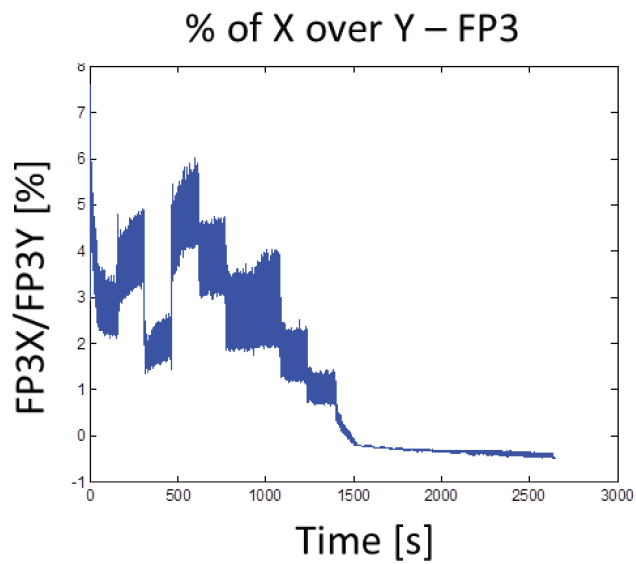


Figure 5.20 - Percentage of exhaust gas force components.

The X components from actuator and exhaust pressure forces are not relevant in comparison to the Y-components, this is explained by the small opening angle measured due to the soft speed transitions, characteristic from a dynamometer test. This same behavior is not expected on vehicle measurements where the speed transition is faster.

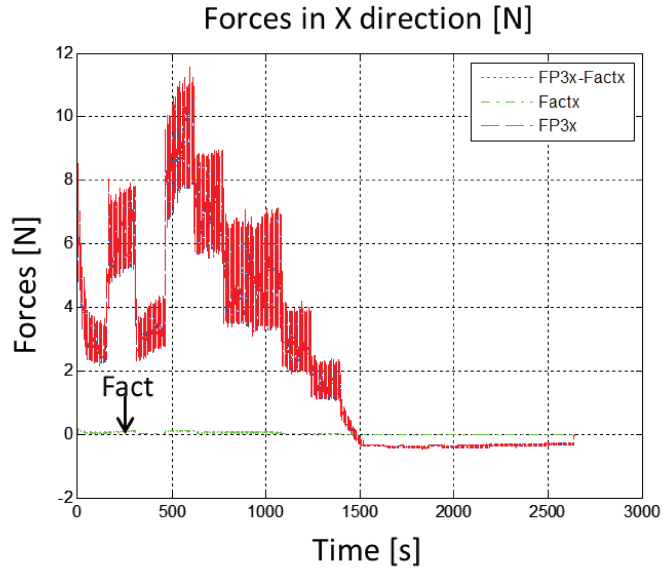


Figure 5.21 - Resultant forces in the X direction – dynamometer test.

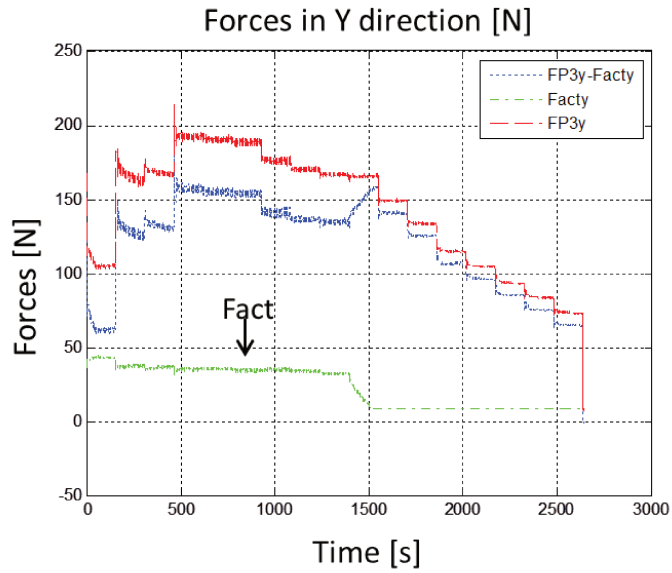


Figure 5.22 - Resultant force in the Y direction - dynamometer test.

5.2 Vehicle measurements

The vehicle used to perform measurements had basically the same engine, but a 150Hz PWM valve assembly to control the actuator. In this case, the data acquisition system sampling frequency was set to 1000Hz, 10 times higher than the one used during the dynamometer test, which allowed analyzing in more detail other phenomena.

Different from a dynamometer test, during a vehicle test it is not possible to control the engine speed, which varies according to the driver, the track, the traffic, among other factors. The advantage is that the real variation of engine speed over time can be measured, Figure 5.23 shows the engine speed in function of time.

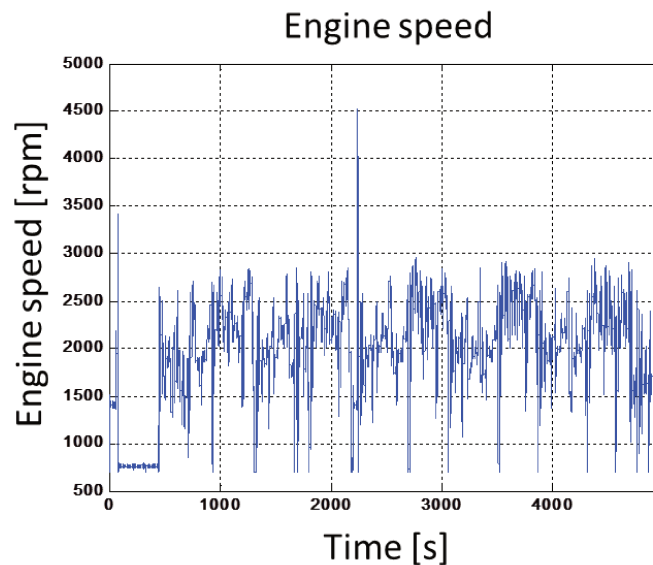


Figure 5.23 - Engine speed- vehicle test.

Because of the vehicle test, it is possible to see some peaks in the actuator displacement measurements presented in Figure 5.24. The average displacement is higher than the measured on dynamometer.

Different from the dynamometer results, in these measurements, only 10% of the actuator displacements were smaller than 0.1mm (Figure 5.25), but still there is a high occurrence of micro movements lower than 0.3mm, which adds up to 60% of all period of time recorded, as is shown in Figure 5.26.

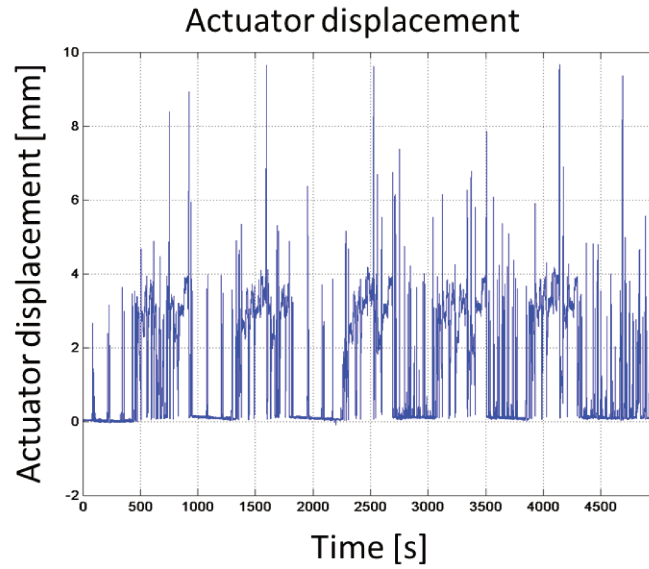


Figure 5.24 - Actuator displacement - vehicle test.

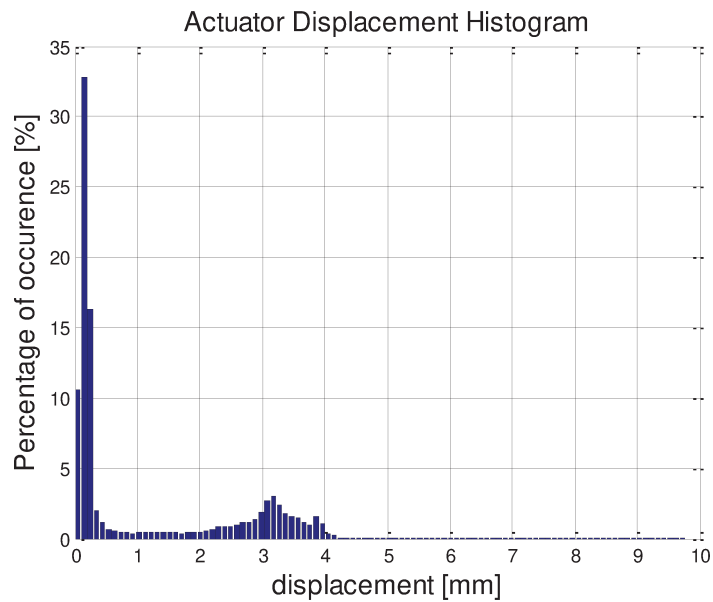


Figure 5.25 - Actuator displacement histogram - vehicle test

The PWM operational frequency component of 21Hz from the valve from dynamometer test could not be detected in the actuator displacement waterfall, confirming that the 21Hz was really coming from the PWM valve. But the 150Hz frequency component from the new PWM valve was not detected either. This could be justified by the new technology used in the valve

super-dumping the system, but unfortunately this is customer confidential information and could not be shared in detail.

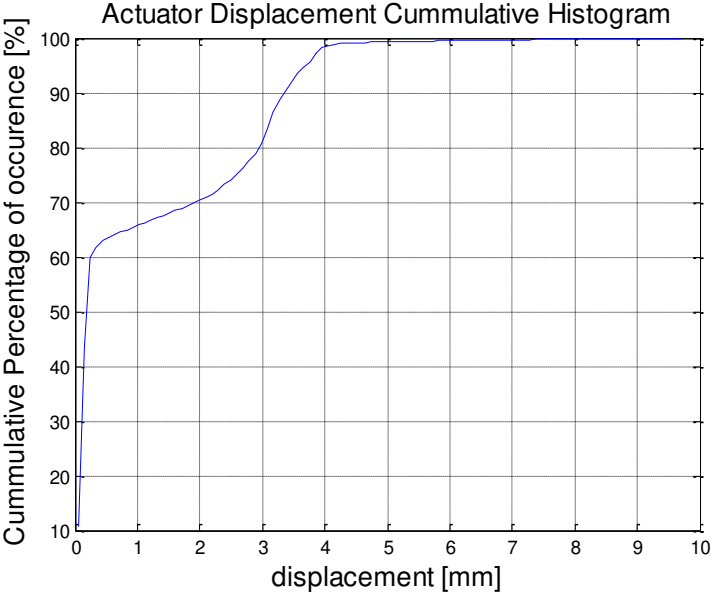


Figure 5.26 - Actuator displacement cumulative histogram - vehicle test.

Further studying the actuator displacement signal, an order map in function of the engine speed was analyzed and showed that the second and fourth orders of the engine speed are the more important ones. This makes sense, once the measured vehicle has a four cylinders engine, four-stroke, that means that for every revolution there are two cylinders firing, which is a second order excitation. Once the pressure variation is not pure sinusoidal, other harmonics can also appear in the measured signals, in this case the fourth component is also relevant. Actuator displacement order map is presented in Figure 5.27:

The actuator pressure measurement over time is displayed in Figure 5.28. In comparison to the dynamometer result, the amplitude is much higher, already expected from the fast engine speed variation.

The actuator pressure histogram (Figure 5.29) and cumulative histogram (Figure 5.30) show that the lowest pressure level, equivalent to the 0.1mm displacement, represents about 10% of the overall time measured. And 60% of the pressure occurrence is in a low level, matching to the actuator displacement results.

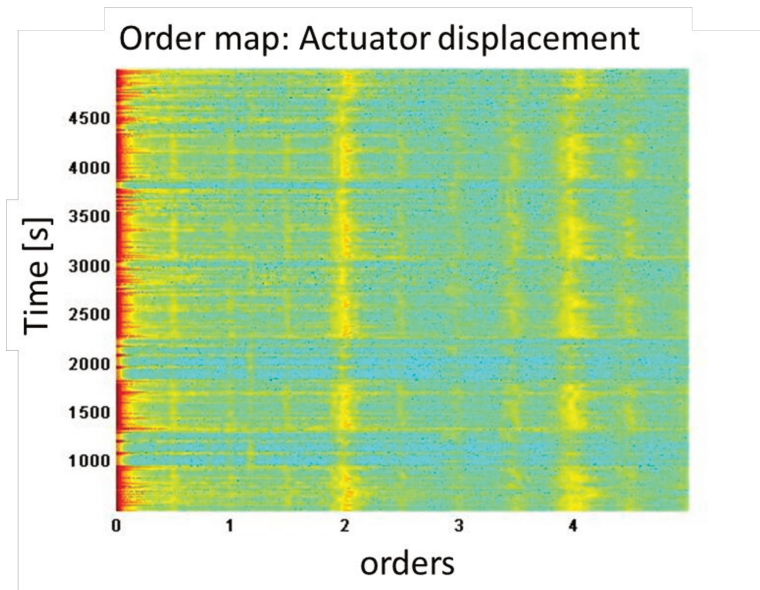


Figure 5.27 - Actuator displacement order map - vehicle test.

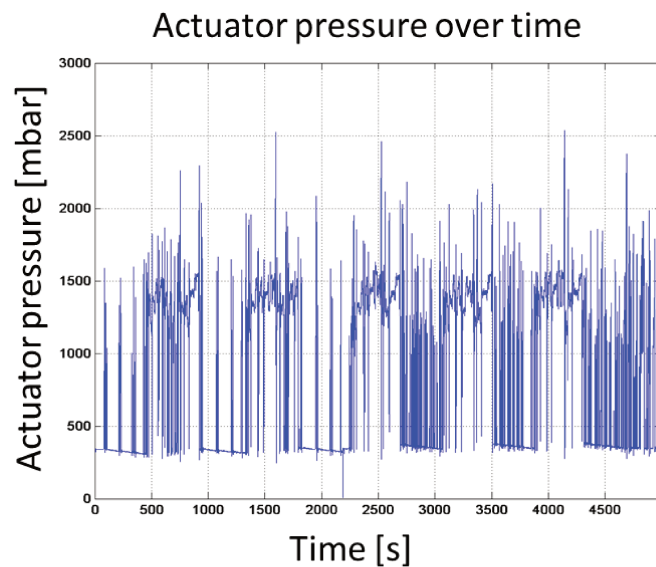


Figure 5.28 - Actuator pressure - vehicle test.

The actuator pressure waterfall exhibited in Figure 5.31 does not show the 21Hz neither 150Hz. A frequency component in 115Hz was highlighted, but it does not match with the PWM valve operational frequency.

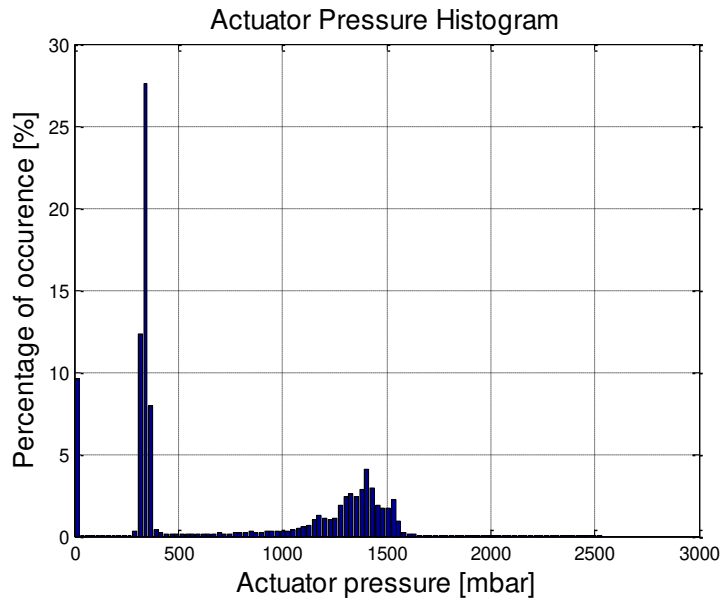


Figure 5.29 - Actuator pressure histogram - vehicle test.

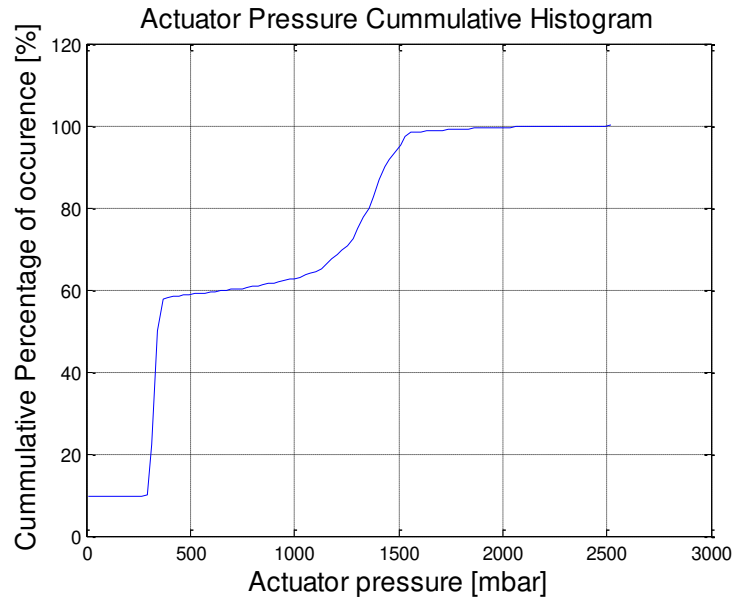


Figure 5.30 - Actuator pressure cumulative histogram - vehicle test.

The actuator pressure order map analysis plotted in Figure 5.32 also shows the engine second and fourth order in evidence.

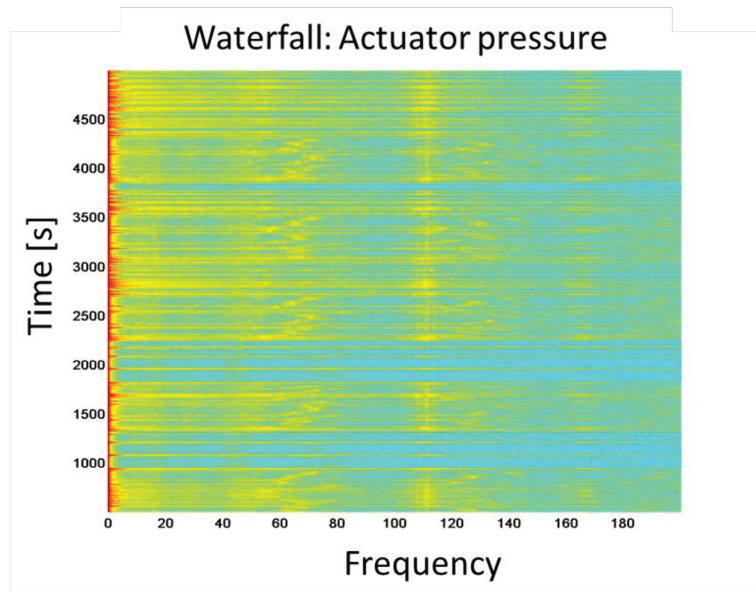


Figure 5.31 - Actuator pressure waterfall - vehicle test.

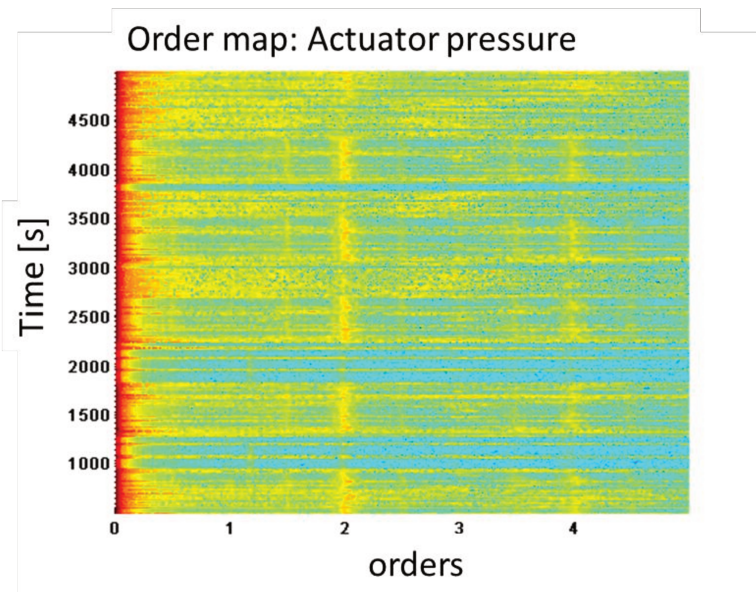


Figure 5.32 - Actuator pressure order map - vehicle test.

The actuator force decomposition into F_{actX} and F_{actY} presented in Figure 5.33 shows a stronger influence of the X component in comparison to the dynamometer test, but it still does not reach more than 7% of the Y component, as shown in Figure 5.34.

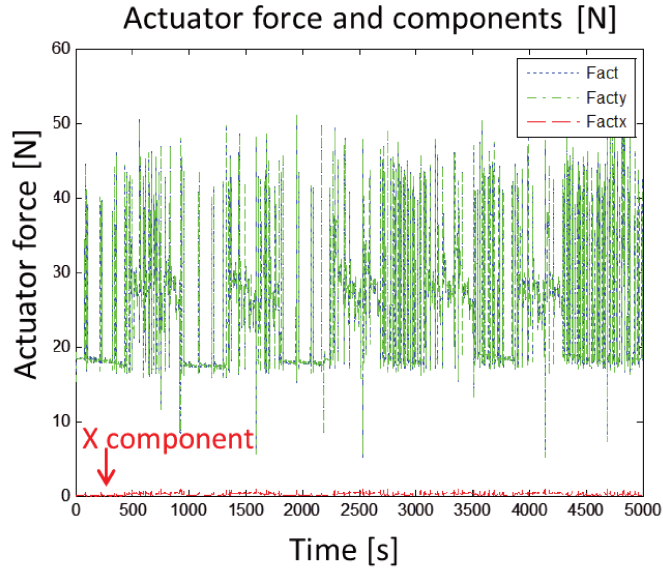


Figure 5.33 - Actuator force components- vehicle test.

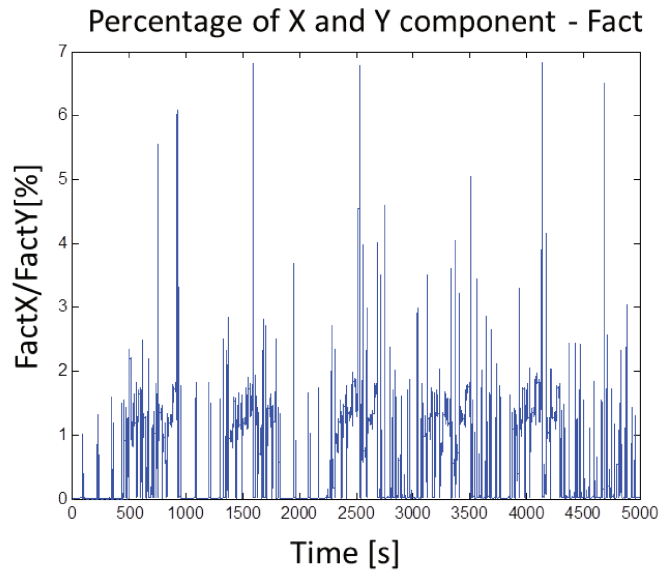


Figure 5.34 - Percentage of actuator force components -vehicle test.

The exhaust gas pressure over time is plotted in Figure 5.35. As expected it also presents higher amplitude in comparison to the dynamometer test, due to the faster engine speed variation.

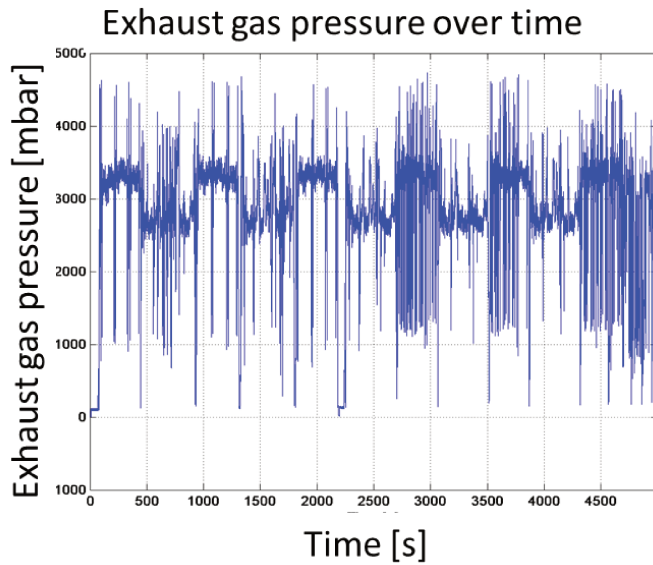


Figure 5.35 - exhaust pressure - vehicle test.

The Exhaust pressure level is well distributed in the complete operational range, as illustrated by Figure 5.36 and Figure 5.37.

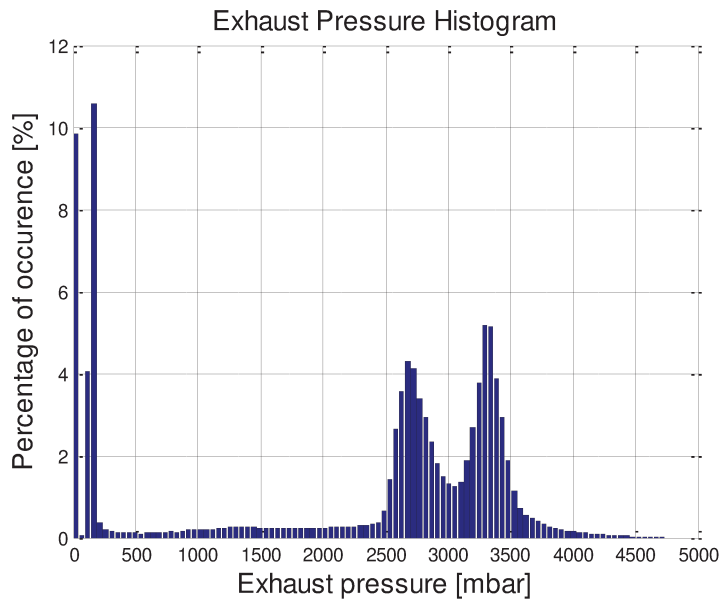


Figure 5.36 - Exhaust pressure histogram - vehicle test.

The exhaust pressure order map in function of engine speed exhibited in Figure 5.38 was analyzed and showed that the second and fourth orders of the engine speed are the more important ones, as expected for this 4 cylinders engine.

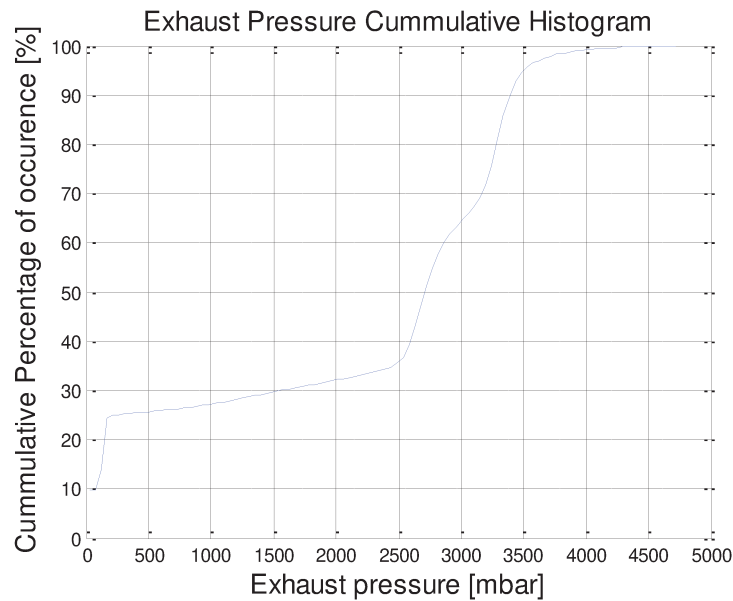


Figure 5.37 - Exhaust pressure cumulative histogram - vehicle test.

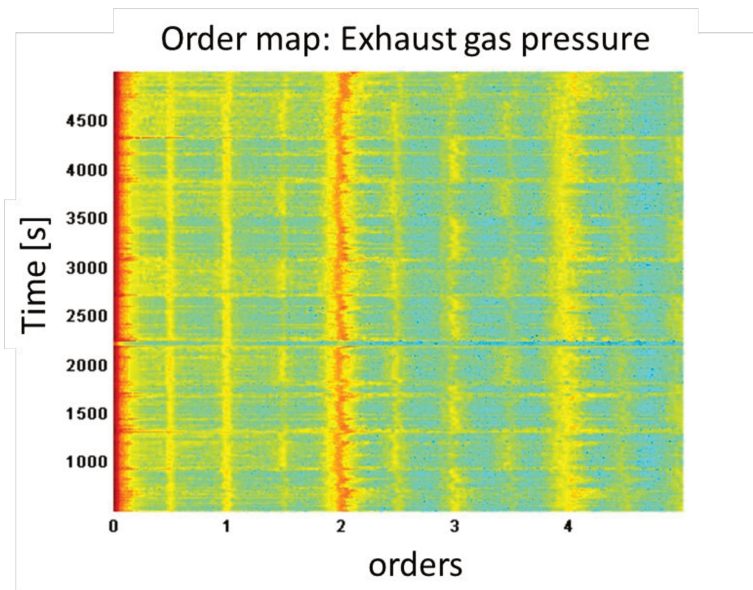


Figure 5.38 - Exhaust pressure order map - vehicle test.

The exhaust gas force X and Y components can be seen in Figure 5.39. In this case, there is a much higher influence of the X component than that observed in dynamometer test. The reason is that the valve opening angle β is higher, reaching peaks of 30° (Figure 5.40). Therefore, the X component also reaches peaks of 50% of the Y component as plotted in Figure 5.41.

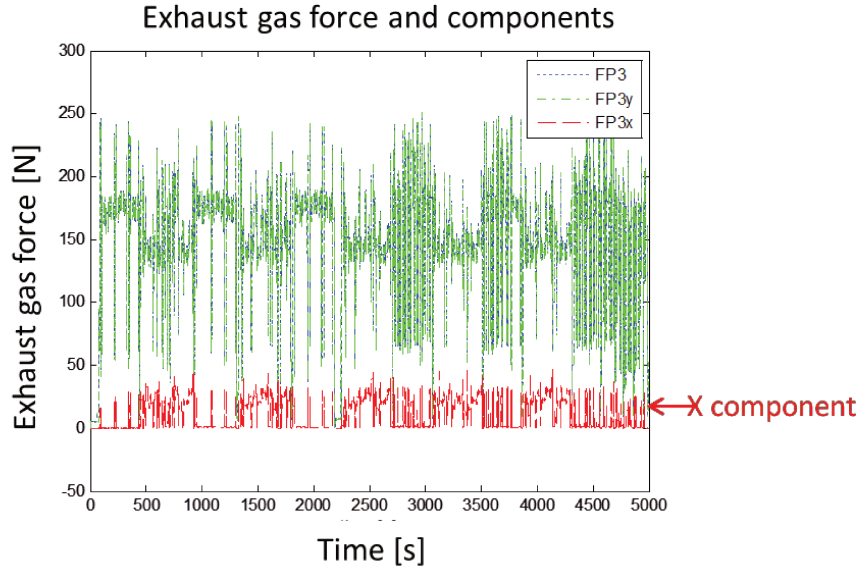


Figure 5.39 - Exhaust gas force components - vehicle test.

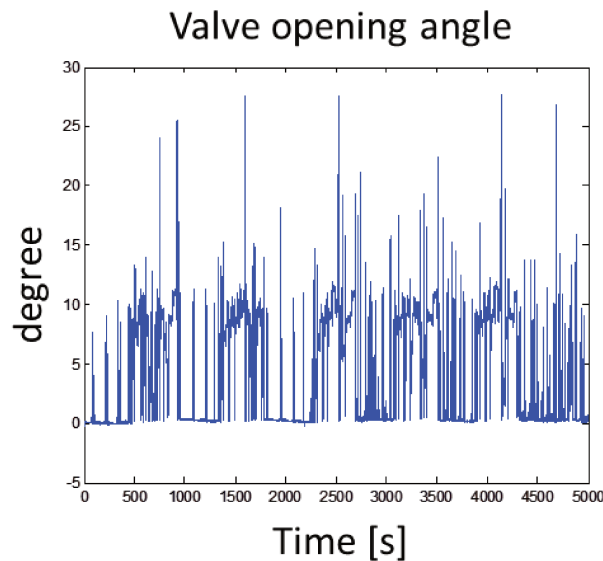


Figure 5.40 - Valve opening position (Beta) - vehicle test.

The resultant force in the X direction, $Res_X = F_{P3X} - F_{actX}$, plotted in Figure 5.42, shows the same result than the dynamometer test, the resultant force is very similar to the exhaust force because the actuator force is very low.

The resultant force in the Y direction had a very different behavior than the dynamometer test, because of the fast engine speed variation of the vehicle test. There are moments when the

actuator force is bigger than the exhaust gas force, changing the direction of the resultant, reaching negatives values. This can be confirmed in Figure 5.43.

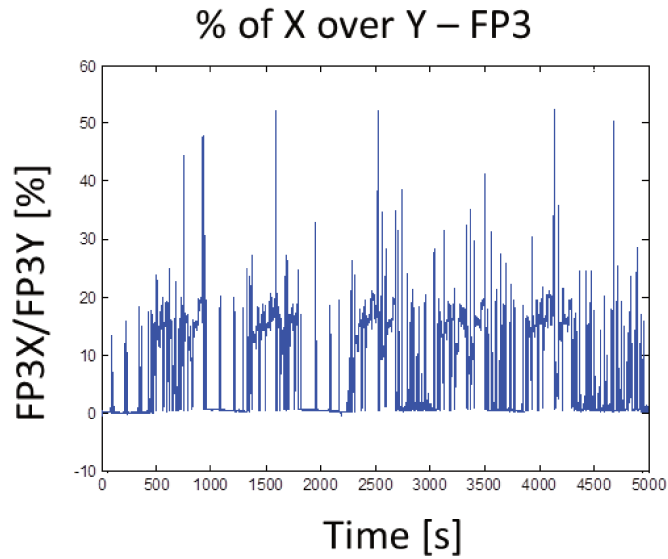


Figure 5.41 - Percentage of exhaust force components - vehicle test.

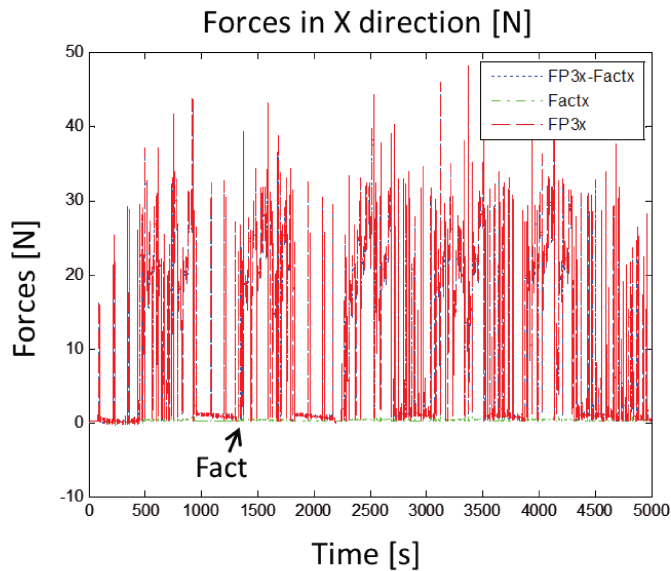


Figure 5.42 - Resultant force in X direction - vehicle test.

The conclusions from vehicle tests are that by changing the control valve operational frequency from 21Hz to 150Hz, the 21Hz frequency is no longer highlighted in the actuator

pressure and displacement waterfall graphics. As the acquisition sampling rate, was 1000Hz that means 10 times higher than the dynamometer test, it was now possible to observe another critical frequency, the engine second order. Although the 21Hz frequency was not highlighted, there is still a concentration of micro movements lower than 0.1mm.

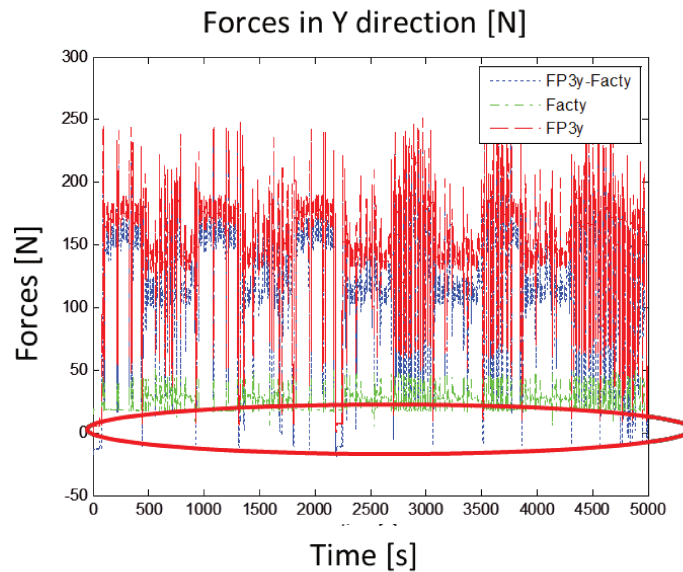


Figure 5.43 - Resultant force in Y direction - vehicle test.

It is possible to conclude that there is a dynamic behavior between the actuator force and exhaust gas force. There are specific conditions when the actuator force is higher than the exhaust force, which could cause a different contact point between shaft and bushing.

6 EXPERIMENTAL PROCEDURE II – WEAR ANALYSIS

In this chapter the wear measurements and analysis of shafts and bushings after going through durability tests are presented. Moreover, a wear comparison between two systems that run durability test using different control valve operational frequency is also made. And finally, the influence of the design parameters on the shaft and bushing wear rate is analyzed.

Durability vehicles run repeatedly critical tracks, representative of real application in different conditions as highways, off road, city cycles and others, depending on the target market. The main objective of such tests is to analyze components behavior, before releasing them to production. In the present case of the bypass valve, the wear of shaft and bushing was measured after the turbocharger cumulated a specific target mileage.

For this analysis, an universe of ten vehicles was used: from two different applications (bus and trucks), with two different engines (4 and 6 cylinders), driven on different tracks (urban and highway), by different drivers, each one with different load and running for different mileage. All these broad variety of conditions result in completely different loads applied to the valve. The distribution of vehicles analyzed is shown in Figure 6.1.

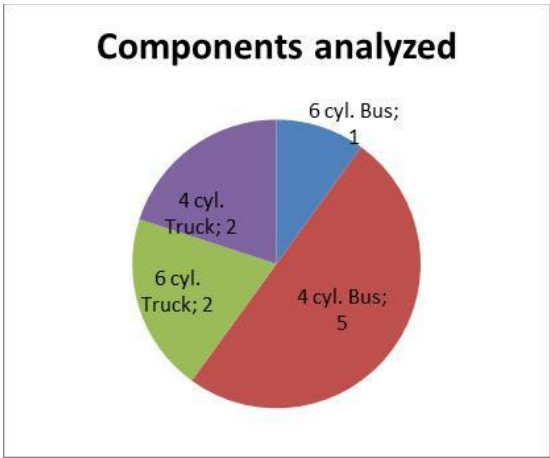


Figure 6.1 - Universe of vehicles analyzed.

In the shaft, the wear region appears on the back of the valve plate, as shown in Figure 6.2. The wear is in the same direction of the exhaust pressure, suggesting that this exhaust pressure is pushing the shaft against the bushing, and this contact is causing wear. In the 4 cylinders engines, heavier wear signs were detected close to the actuator side while in the case of the 6 cylinders engine, the wear marks started close to the valve plate.

In order to measure the bypass valve wear, the shaft was cut from the lever arm to draw it from the turbine housing, carefully cleaned up, and fixed in a device to keep the shaft parallel to the z axis from the tridimensional measurement machine, as demonstrated in Figure 6.2.

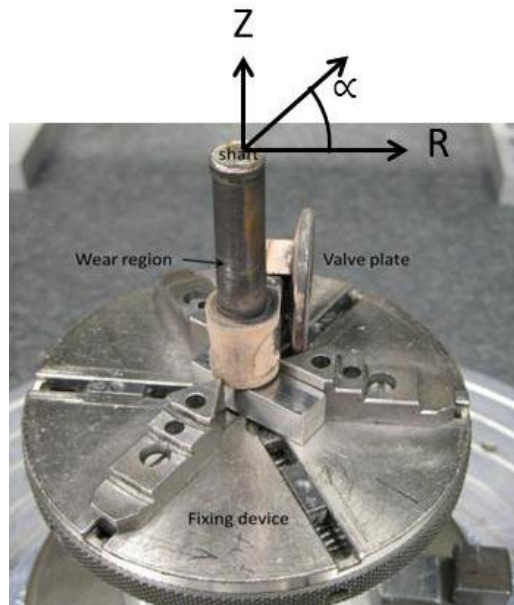


Figure 6.2 – Fixing device for wear measurement.

Beginning from the edge close to the valve plate, the machine started reading the X and Y position of each point in the perimeter of the shaft, in the whole 360°, keeping the same Z position. After the complete ring was measured, the machine displaced 1mm in the Z direction towards the cut end (in the upper side in Figure 6.2.) and measured the following ring.

6.1 Wear parameters

The main objective of this section is to find some important wear parameters, as the wear area, depth, and length that may contribute to the wear analysis working as input for the wear rate calculation.

The wear measurements and data analysis were conducted for all ten vehicles commented before. However, in order to facilitate the explanation, the results from a specific truck (T4.2) – a four cylinders engine, assembled with a 21Hz PWM control valve, which run the durability test for 37,000km – were taken as example to be detailed in this section. Further results from the other vehicles are available in the Appendix.

The wear measurements from the shaft and bushings were collected, processed and transformed into cylindrical coordinates to plot the graphics exhibited in Figure 6.3, where the abscissas are the shaft and bushing perimeters, opened in 360 degrees, and the ordinate is the shaft/bushing length. An interpolation of the measured points was necessary to guarantee that the whole cylinder surface could be plotted. Unfortunately the shaft and bushing wear regions were not aligned during measurements.

In Figure 6.3, the color map is associated to the depth of the wear: the hotter (red) the color, the deeper is the wear on that region (the smaller is the diameter in the case of shaft and the bigger is the internal diameter in the case of the bushing). It is possible to detect a higher concentration of wear in one end of the shaft/bushing, and not a distributed wear along the shaft/bushing length. This observation suggests that the initial contact area was a point, and not a line, as Hertz cylindrical contact theory predicts. This is due to the fact that the forces on both ends of the shaft are not equal, leading to a slight tilt.

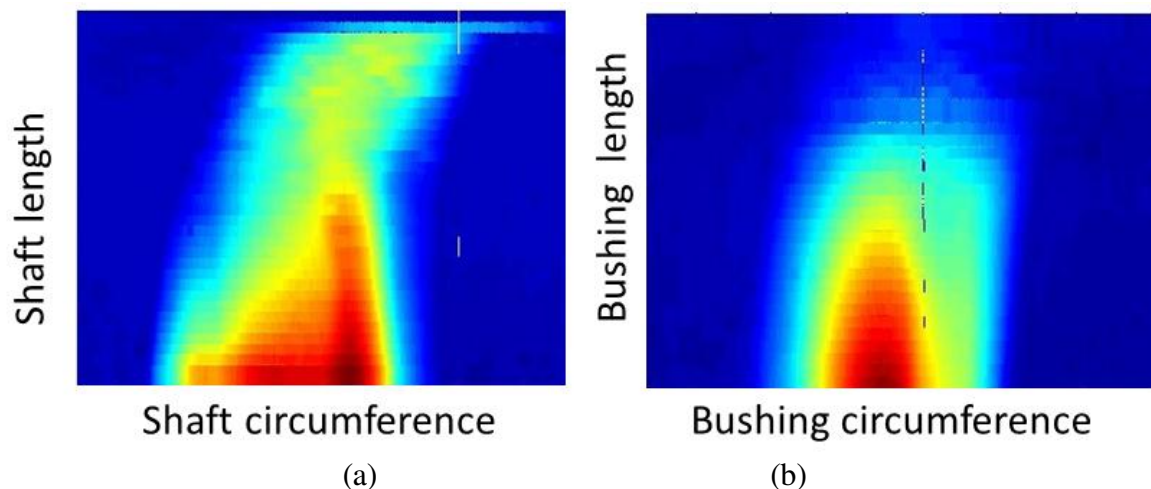


Figure 6.3 – (a) Shaft and (b) bushing wear measurement. Truck T4.2.

The deepest point in the worn region can be considered as the first contact point, and the progression of this contact area is modeled in order to give a contact area as a function of wear depth. This means that the more severe is the wear, the bigger is the contact area, where the forces acting in the system are distributed.

The second step on the wear analysis was to draw the contour line of each wear depth, bounding its contact area. Each contour line represents 0.05mm of wear depth and is plotted in Figure 6.4.

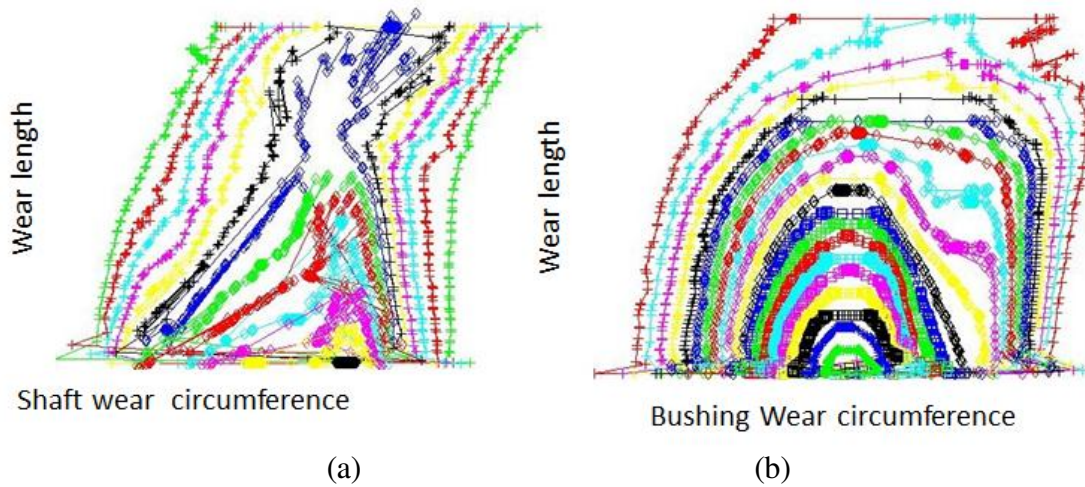


Figure 6.4 – (a) Shaft and (b) bushing wear area bounded for each wear depth. Truck T4.2.

A side view of the bushing wear contour shown in Figure 6.4(b) can be seen in Figure 6.5. It is easy to see that the deeper the wear depth, the smaller is the length and also the worn area. Isolating each contour area, it was possible to calculate the contact area for every wear depth and to build the correlation between them, as shown in Figure 6.6, for the shaft, and in Figure 6.7, for the bushing. In order to fit a second order polynomial regression in the measured points, an intersection at initial point [0, 0] was forced. As one can see, the deeper the wear, the bigger is the contact area between shaft and bushing.

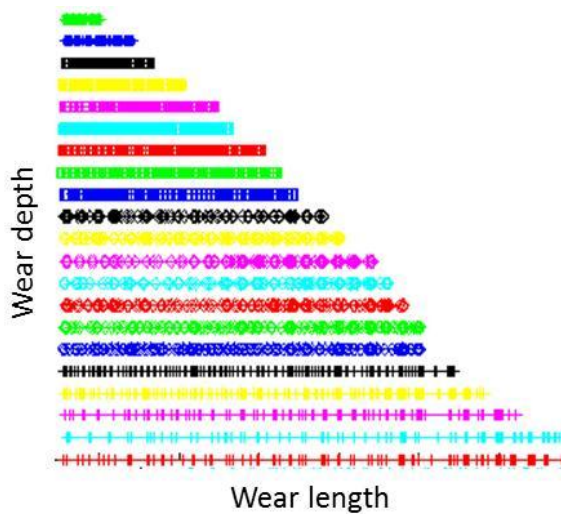


Figure 6.5 – Bushing wear length vs depth.

Shaft T4.2 Contact area @ each depth wear

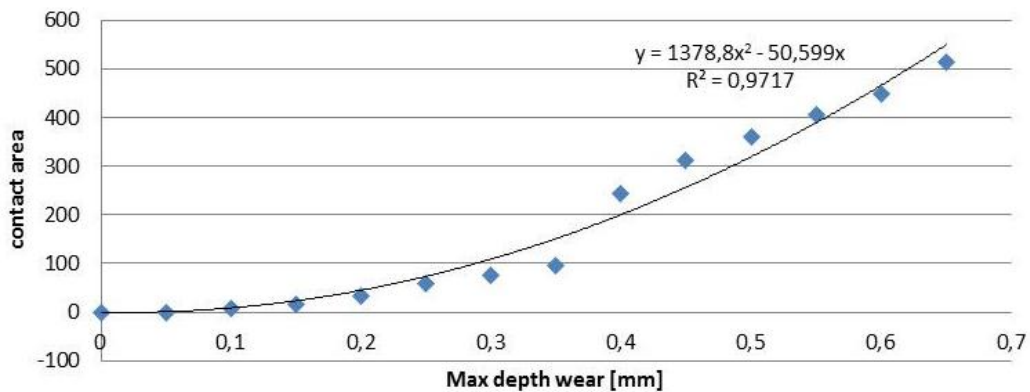


Figure 6.6 – Shaft wear area vs wear depth. Truck T4.2.

Bushing T4.2 Contact area @ each depth wear

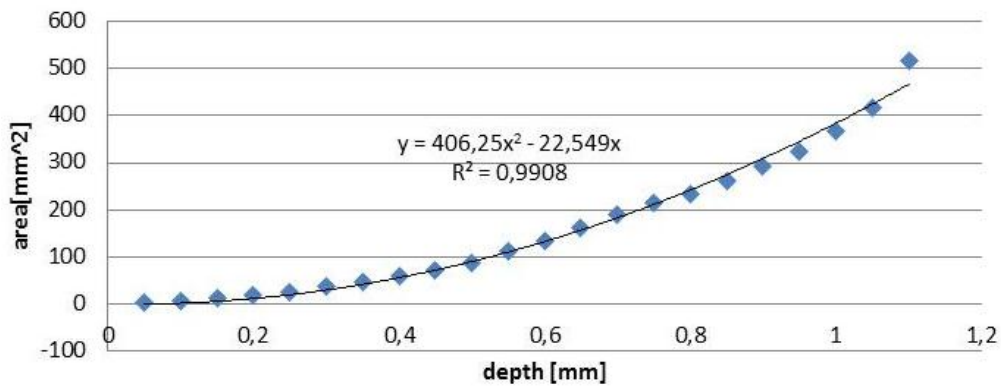


Figure 6.7 – Bushing wear area vs wear depth. Truck T4.2.

Wear volume was also calculated multiplying the contact area by wear depth. The cumulative wear volume versus wear depth is given in Figure 6.8, for the shaft, and in Figure 6.9, for the bushing. A second order polynomial regression with initial point at [0, 0] could be fitted successfully.

The circumference axis of the contact area or the contact width could also be correlated to each wear depth, as seen in Figure 6.10, for the shaft, and in Figure 6.11, for the bushing. However, in this case, a linear regression was more appropriated. Intersection point [0, 0] had also to be forced. The deeper the wear, the bigger is the contact area and the wider is the contact.

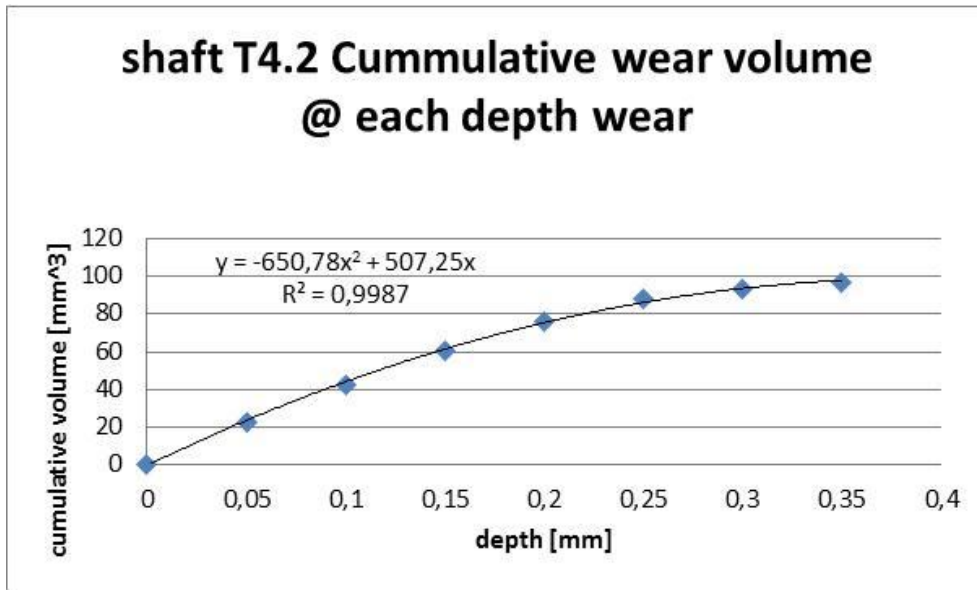


Figure 6.8 – Shaft cumulative wear volume vs wear depth. Truck T4.2.

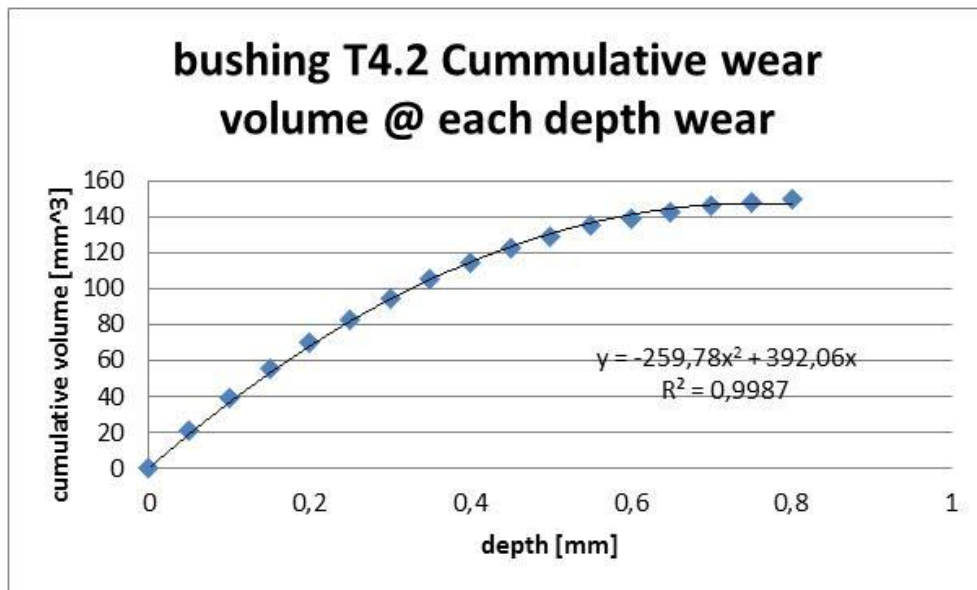


Figure 6.9 – Bushing cumulative wear volume vs wear depth. Truck T4.2.

The length axis of the contact area to each wear depth is plotted in Figure 6.12 for the shaft and in Figure 6.13 for the bushing, a linear regression fit to correlate the measured points with intersection on [0,0]. Obviously, the deeper is the wear, the bigger is the contact area and the longer is the contact.

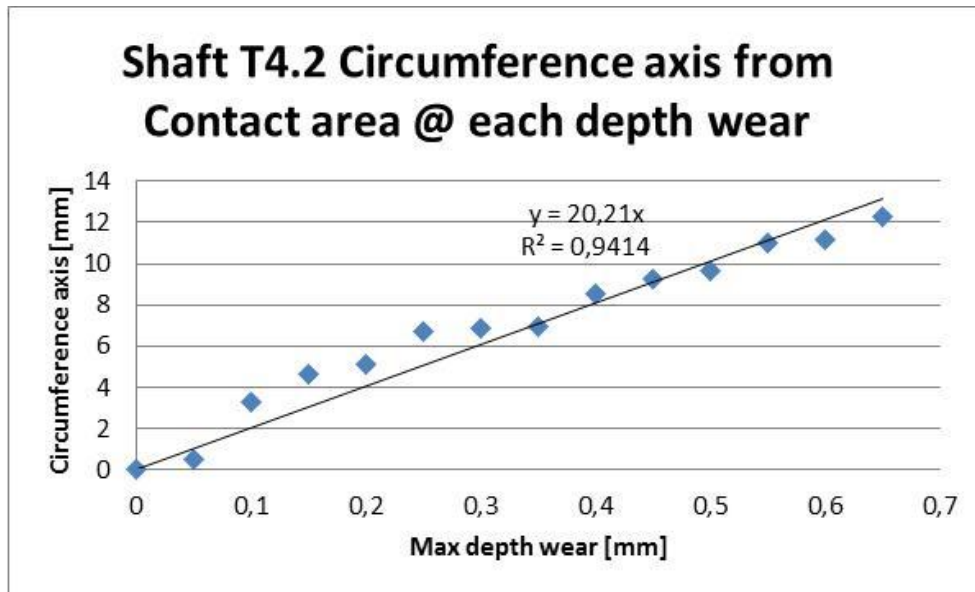


Figure 6.10 – Shaft circumference axis. Truck T4.2.

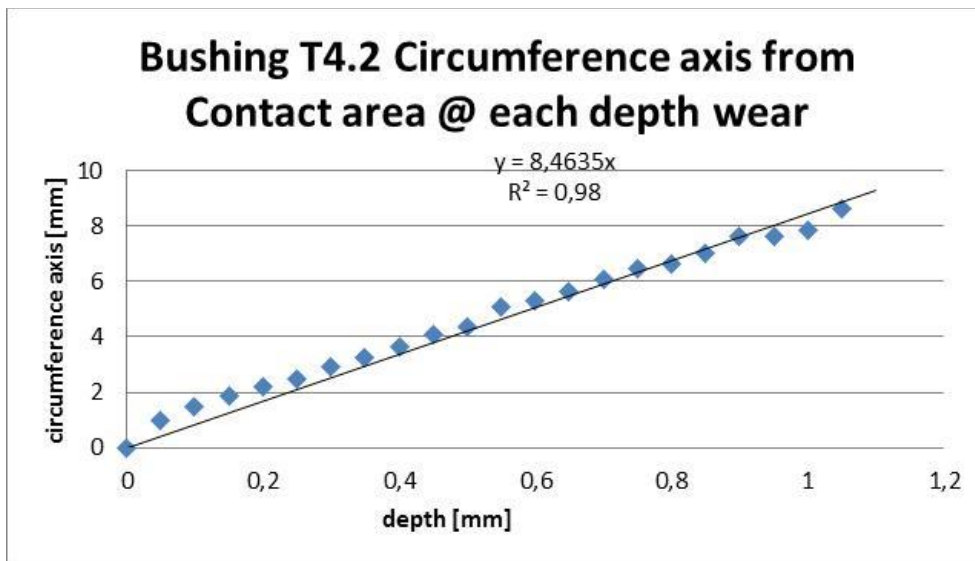


Figure 6.11 – Bushing circumference axis. Truck T4.2.

All these correlations and resulting equations make possible a good wear parameters prediction. Analyzing the circumference and length axis correlation to wear depth from all the shafts and bushings, the result is that a linear regression with intersection at point [0, 0] can be considered, with a determination coefficient R^2 greater than 0.9.

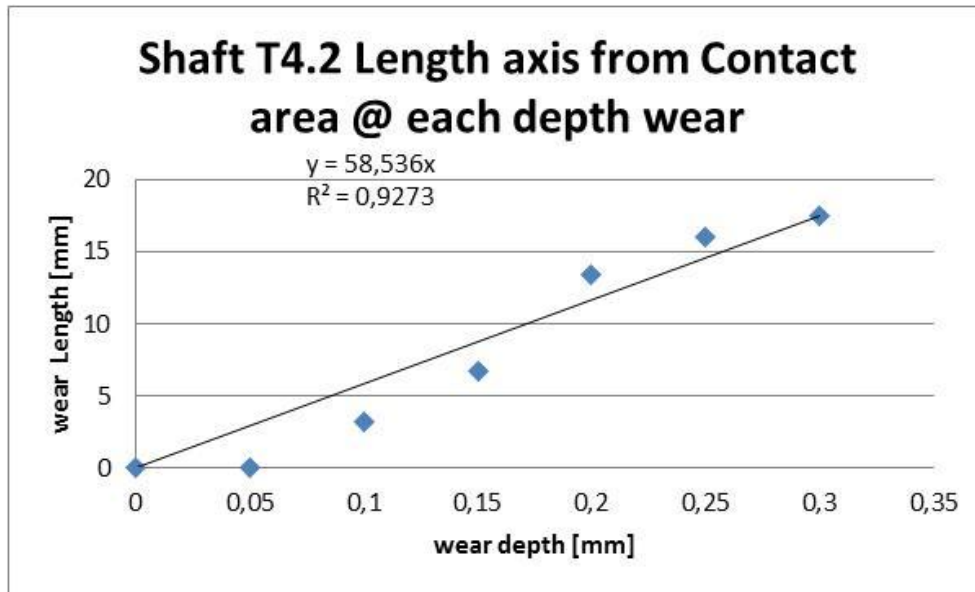


Figure 6.12 – Shaft length axis. Truck T4.2.

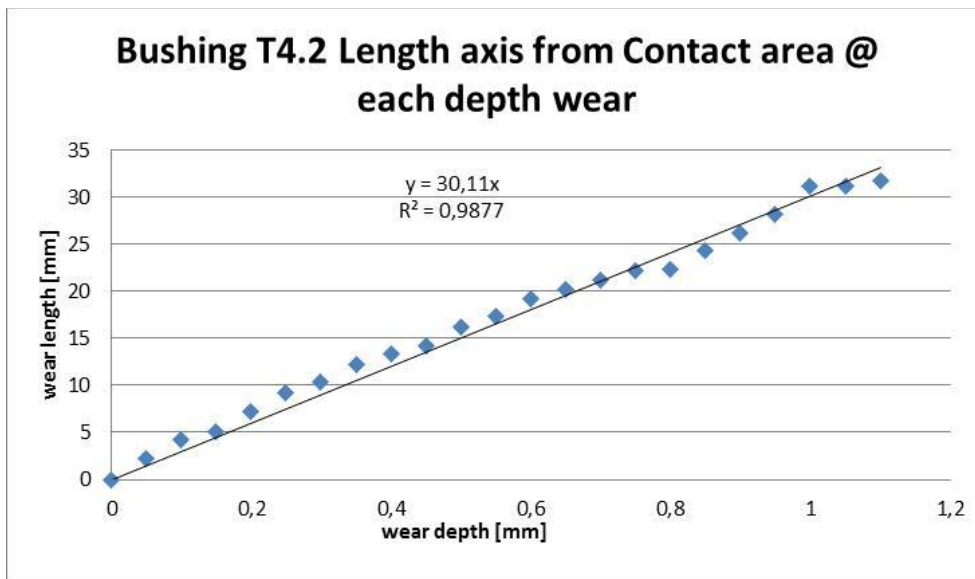


Figure 6.13 – Bushing length axis. Truck T4.2.

6.2 Wear comparison between two control valve systems

In order to verify whether or not the control valve operational frequency can affect the wear rate on the shaft and bushing, a comparison between two 4 cylinders engine trucks was performed. The first subject used was the already introduced Truck T4.2 – which ran for 37,000km during the durability test with an engine assembled with a 21Hz PWM control valve. The second one was another truck, designated here by T4.3, which performed a 196,400km durability test using a 150Hz PWM control valve. A single shaft/bushing system returned from the durability tests of each vehicle.

Both shaft wear measurements are shown in Figure 6.14. It is possible to note that a different wear pattern emerged: there are two different wear concentration areas in the 150Hz PWM control valve map, and they are basically one opposite to the other. The wear pattern difference analysis is not a subject under study in this dissertation, but can be considered in further studies.

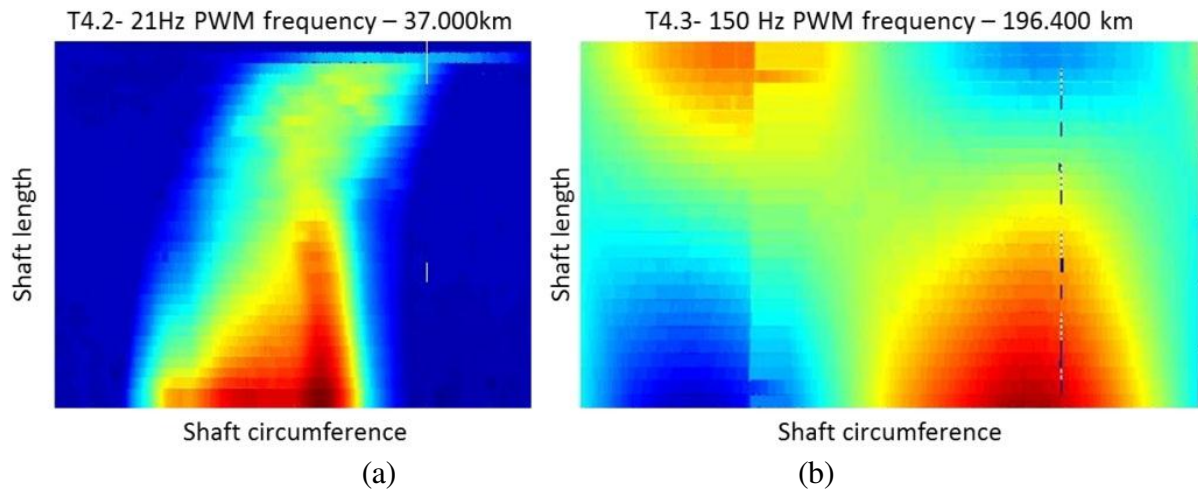


Figure 6.14 – Shaft wear measurements. (a) 21Hz and (b) 150Hz PWM control valve.

Computing the wear depth, wear area and wear volume per kilometer, it is possible to conclude that the overall wear rate increased with the 21Hz PWM control valve. Considering the results of this system as baseline, Figure 6.15 shows that the valve wear rate increased by about five times when compared to the 150Hz PWM control valve.

SHAFT Wear rate comparison 21Hz x 150Hz

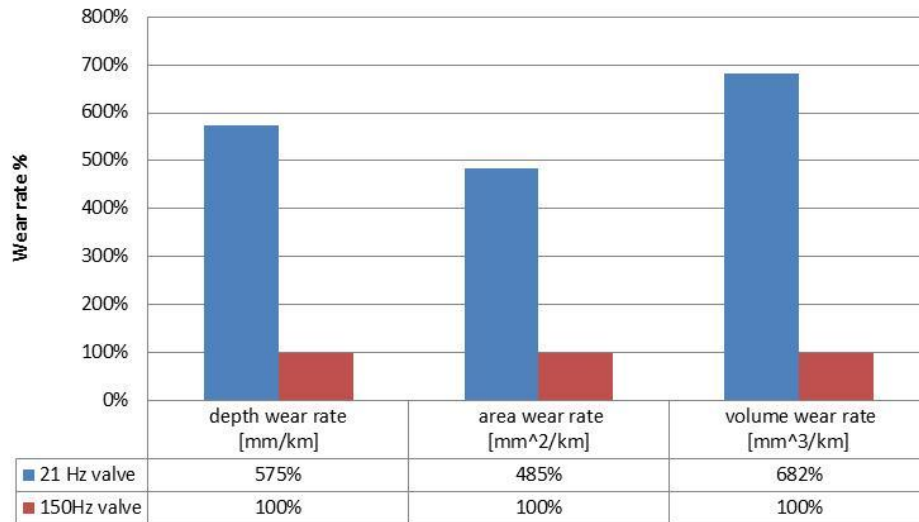


Figure 6.15 – Shaft wear rate comparison: 21Hz and 150Hz PWM control valve.

The bushing wear also presented a different wear pattern, as shown in Figure 6.16. Observing the 150Hz PWM measurements (Figure 6.16(b)), it is not possible to say there is a second wear concentration in the opposite end, but there is an extended wear region along the bushing.

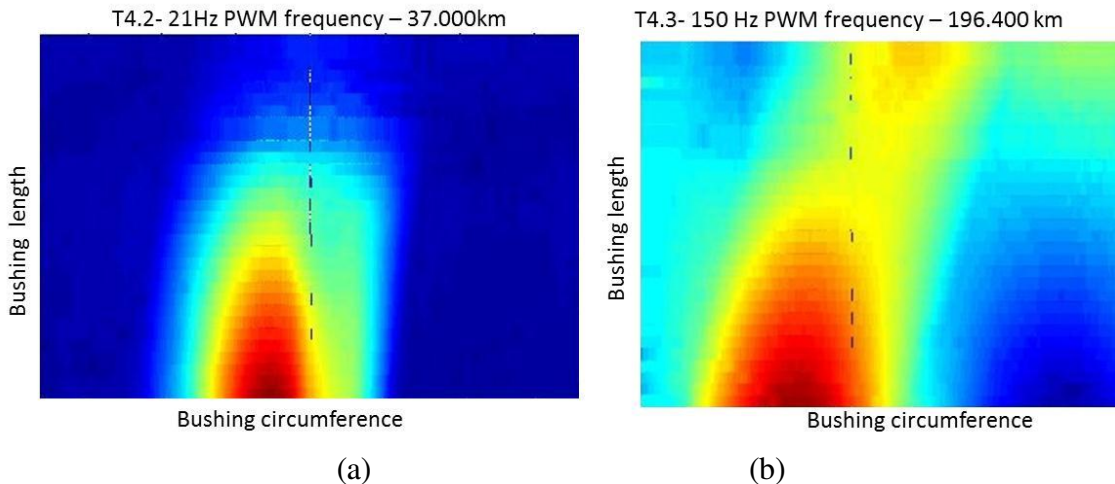


Figure 6.16 – Bushing wear measurements. (a) 21Hz and (b) 150Hz PWM control valve.

For the bushing, the improvement in the wear rate using a 150Hz PWM control valve is up to six times when compared to the 21Hz PWM control valve, as plotted in Figure 6.17

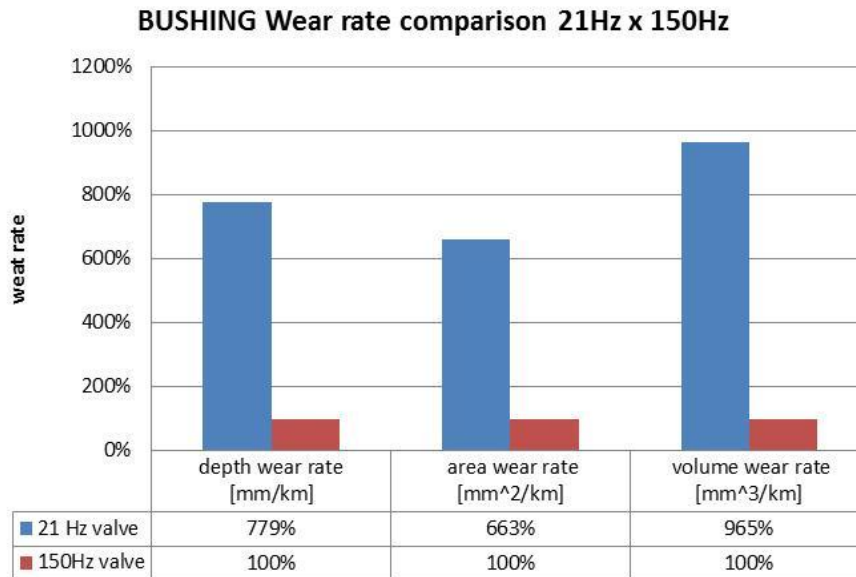


Figure 6.17 – Bushing wear rate comparison: 21Hz and 150Hz PWM control valve.

The result is no doubt positive, but it was only analyzed one shaft and bushing out of each vehicle. From a statistic perspective, that is not enough to state any conclusion yet. More samples are needed to have a reliable universe and confirm the improvement rate brought by the 150Hz PWM valve.

6.3 Semi-ellipse adaptation

Motivated by the second order polynomial regression of the contact area versus wear depth and the linear regression of the circumference and length axis to the wear depth, a semi-ellipse adaptation was made as an attempt to eliminate the wear levels irregularities. The idea behind this procedure was look for a procedure to estimate the shaft and bushing wear rate.

The maximum circumference and length axes measured for each wear level were used in the ellipse formula as the semi-axes limits. So the adapted semi-ellipses had the same width and maximum length as the curve levels contour. The curve levels contour and the corresponding adapted semi-ellipses are all plotted together in Figure 6.18.

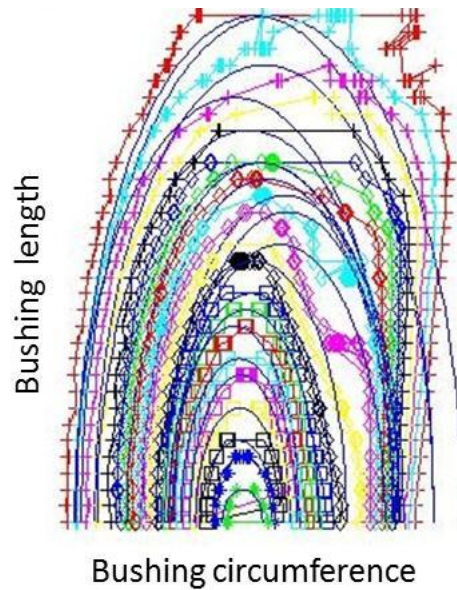


Figure 6.18 – Bushing wear curve level and adapted ellipse. Truck T4.2.

For every curve level, the measured area and corresponding adapted semi-ellipse area were calculated and compared. The difference between both area values for each level is shown separately in Figure 6.19.

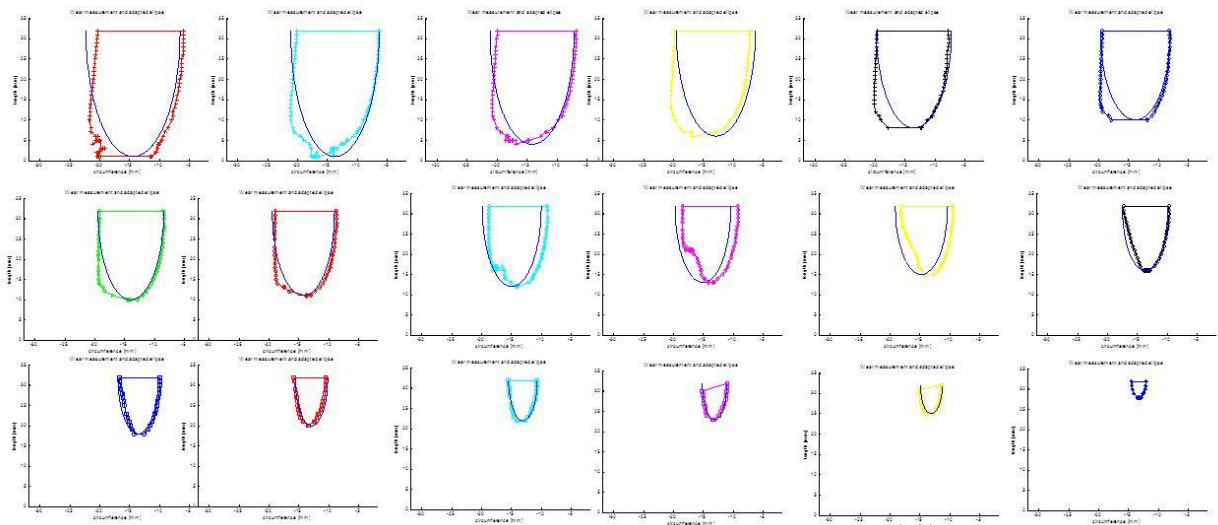


Figure 6.19 – T 4.1 Adapted semi-ellipse area errors for each wear level. Truck T4.2.

The semi-ellipse adaptation was done for all shafts and bushings measured out of the durability vehicles. The error for each level was calculated, and the error average for the complete component was also computed. A criteria was defined as error average lower than 30%

to consider the adaptation acceptable, due to possible measurement error, component deformation by the time it is cut from the turbine housing and others.

The shafts wear curves were not successfully adapted to semi-ellipses, only 40% of the shafts kept under the target. On the other hand, the bushings fit well to the adapted semi-ellipses, matching 80% of the cases. The error average of shafts and bushings wear area adapted to semi-ellipses are shown in Figure 6.20. The conclusion is that this method could be applied for the bushings, but not for the shafts.

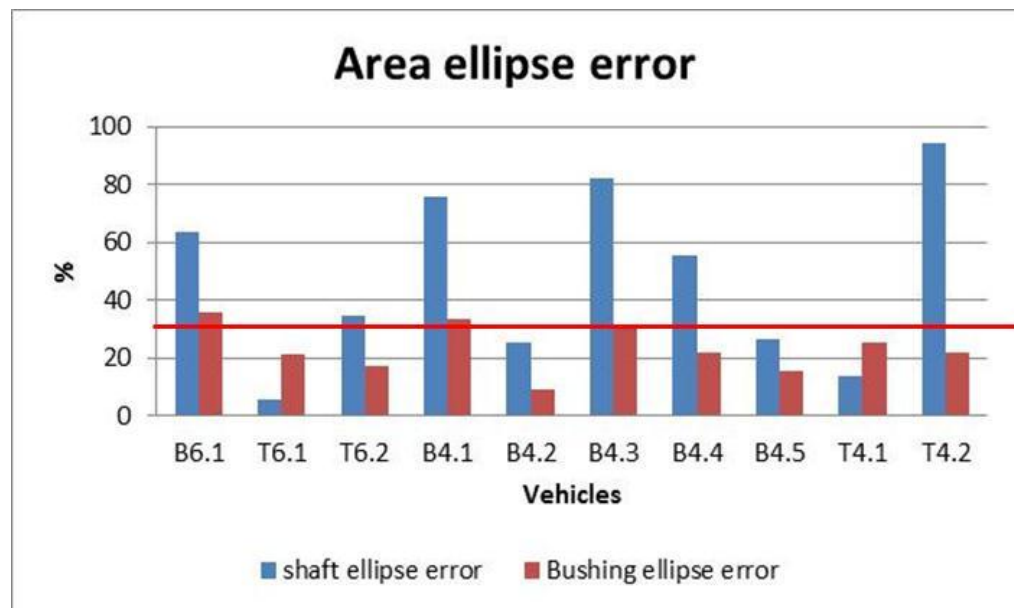


Figure 6.20 - Area semi-ellipse error overview

The semi-ellipse adaptation for bushings can help predicting the wear shape, area and volume as a function of the wear depth. One of the reasons for the “not semi-ellipse adaptable” shape of the wear measured, is the high irregularity of the wear shape, because the forces applied on shaft and bushing are not constant during vehicle operation. This could cause different wear spots that do not start at only one point nor increase proportional to the mileage.

6.4 Wear rate calculation based on measurements

As already mentioned in Section 4.1, the case under study in this dissertation does not satisfy all the assumptions from (Dickrell & Sawyer, 2004), so the amplified formulation to generalize the wear rate calculation must be used.

The general wear rate equation developed with the linear force distribution was given in equation (4.36) and requires some forces and wear parameters. The forces parameters were calculated based on the pressure values measured on vehicle as a function of time, and they were presented in Chapter 5. Unfortunately, the pressure signals were not acquired in every vehicle that had the shaft and bushing wear analyzed. Only the truck 4 cylinders had the complete measurements done that means the pressure and displacements on vehicle and later on, the wear measurements from the shaft and bushing. The wear parameters were obtained from the shaft and bushing wear measurements, as radius, area and length in function of wear depth, as discussed in Section 6.1.

As the coefficient wear (K_s) is unknown, the wear rate calculation will be left as a function of this value, so equation (4.36) can be rewritten as follows:

$$\frac{\Delta R}{\Delta t} \cdot \frac{1}{K_s} = \sum \frac{R(lw)}{A(lw)} \left(F_{actY}(t) z m(lw)^2 + 2 \left(\frac{F_{P3Y}(t) - F_{actY}(t)}{L} \right) \frac{z m(lw)^3}{3} \right) \quad (6.1)$$

For comparison purposes, the wear rate was calculated varying two design parameters: longer bushing length and bigger bushing internal diameter. The wear rate progression can be seen in Figure 6.21.

It is possible to state that the longer bushing provides a decreased wear rate in comparison to the actual design. And on the other hand, a bigger diameter would decrease bushing lifetime. As shown in Figure 6.22, for a 50% longer bushing, there is an average of 30% wear rate improvement. And for a 50% diameter increase, there is about 32% lifetime decrease.

The same calculation was performed using the shaft wear data. It is clear that the bushing wear rate was much higher than the shaft wear rate. In comparison to the bushing, the shaft result trend was the same, but quantitatively there was a considerable difference, as presented in Figure 6.23.

The improvement expected for longer shaft is also about 30% for a 50% length increase. And a 50% bigger diameter brought a 31% lifetime reduction as shown in Figure 6.24:

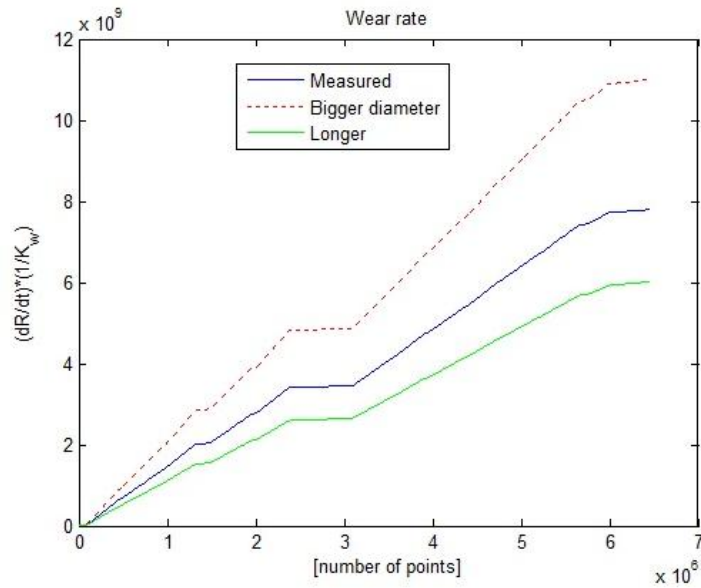


Figure 6.21 - Wear rate comparison - different bushing design parameters.

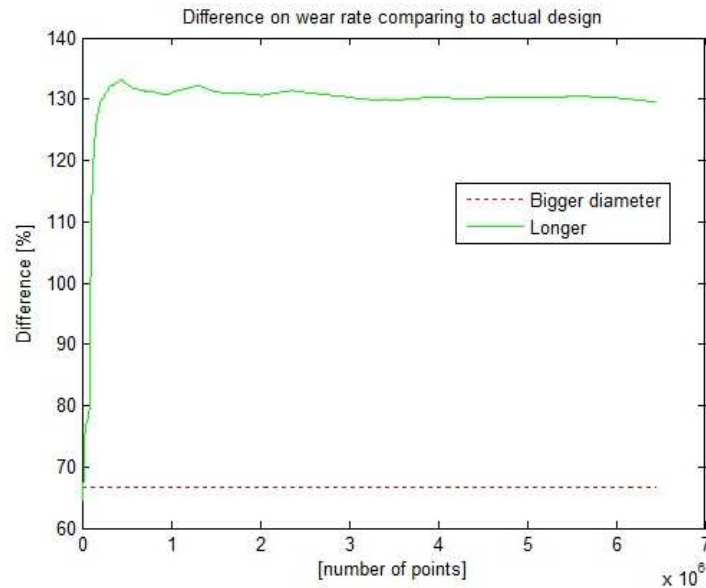


Figure 6.22 - Bushing - % comparison between different design parameters.

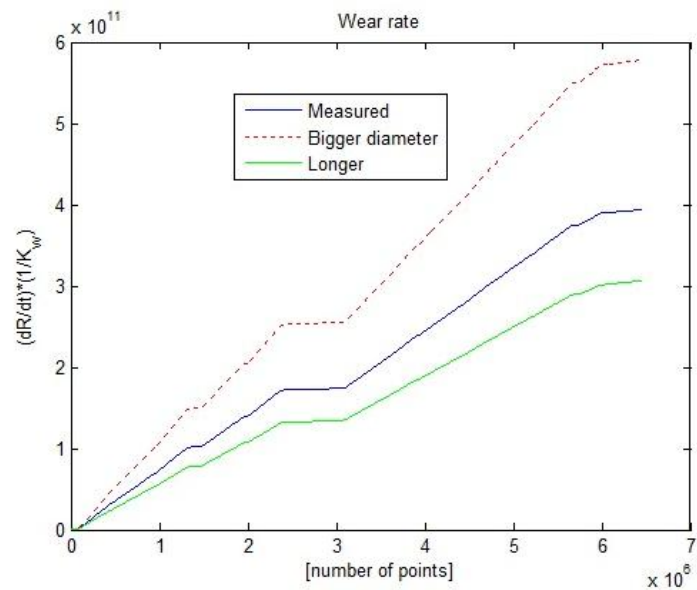


Figure 6.23 - Wear rate comparison - Different shaft design parameters.

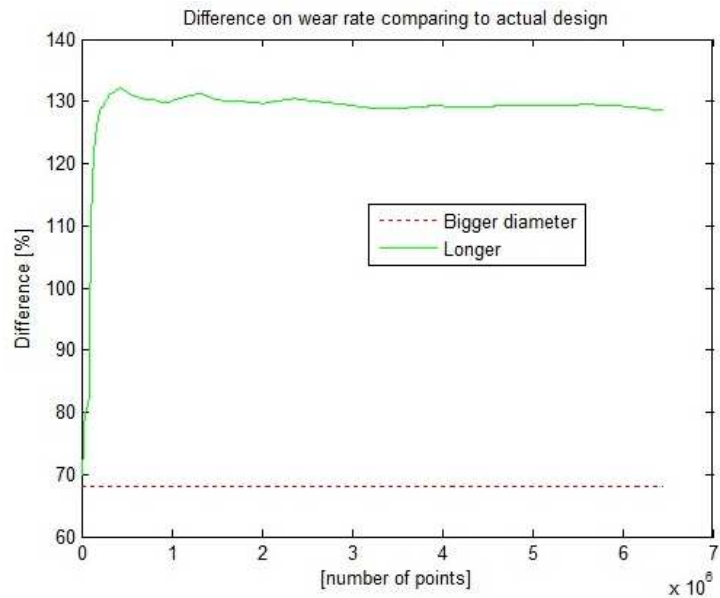


Figure 6.24 - Shaft - % comparison between different design parameters.

7 CONCLUSION AND FUTURE WORKS PROPOSALS

The main objective in this work was to analyze the premature wear presented on shaft and bushing from bypass valves of regulated two stages turbochargers and suggest possible solutions to improve it. This analysis was composed by a theoretical part including static and dynamic conditions and equations of motion. And an experimental part including engine measurements and wear measurements of worn components from durability tests.

7.1 Conclusions

The models for the evolution of wear for a shaft / bushing system can be quite simple – as the one presented by (Dickrell & Sawyer, 2004) which is based on the assumption of uniform contact pressure and constant applied load – or very complex – including the effects of temperature, variable loading, cyclic movement of the shaft inside the bushing, abrasive particles, among others. However, no matter how complex or detailed the formulation to estimate the wear rate can be, the author of the present work did not find in the literature (and do not believe there is) a theory that can explain all the phenomena observed during the development of this dissertation, as, for example, the wear pattern presented on the Appendix.

This dissertation deals with a real application which is the excessive wear rate observed in the bypass valve shaft and bushing system after the durability tests of trucks and busses.

As an attempt to explain such behavior, an extended formulation based on (Dickrell & Sawyer, 2004) equations was proposed, relaxing the original restrictive assumptions in order to make the formulation suitable for the current application. The main change on the original formulation was the assumption of linear force distribution along the shaft and bushing length.

As a first approach, the bypass valve was considered to be a one degree of freedom linear systems, which is a quite reasonable assumption if one considers small angular displacements and neglect the gaps among the components of the systems. The natural frequency of the bypass valve was computed to be about 300Hz. The major concern here was whether or not some

external forces could excite the system near or on this natural frequency, which could increase the dynamic load and, consequently, the wear rate.

There are basically two external forces acting on this system: the actuator force and the exhaust gas pressure force. The control valve operational frequencies were 21Hz and 150Hz, which are far from 300Hz. The engine firing frequency can go up to 50Hz (3000rpm), which means that the 6th order on a 4 cylinder engine (the 2nd and the 4th are usually the most important) and the 4th order on 6 cylinder engine (the 3rd and the 6th are usually the highest ones) could actually excite the system. Another source of excitation could be the turbocharger itself, once the natural frequency of the bypass valve is within the turbocharger operational speed range. Despite the fact that no resonance phenomena were observed during the data processing, further investigation on this subject should be carried on.

A very important conclusion, as highlighted by the pressure and displacement measurements, is that the dynamometric test is not representative when compared to the vehicle test. The dynamic loads acting on the bypass valve during the durability test were much higher than those measured during the dynamometric test. In both cases, however, small movements – about 0.1mm – of the actuator displacement were observed, which could suggest some kind of vibration problem and, for this reason, deserve a deeper analysis.

A 21Hz frequency component was clearly detected in the actuator displacement and pressure order maps. This frequency, which matches with one of the PWM valve operational frequencies, completely disappeared from the measurements when the valve controller was replaced by the 150Hz PWM valve.

Comparing the wear between shaft and bushings that run in the same conditions, except for the PWM valve operational frequency, it was clear that the 21Hz PWM valve had an aggressive wear rate, while the 150Hz PWM valve improved the lifetime about 5 times. The different wear pattern presented by the components that run with a 150Hz PWM valve should also be studied in detail in the future.

For wear comparison, there was only one sample out of durability test using a 21Hz PWM valve and another one using 150Hz PWM valve. From a statistical perspective that is not enough to conclude the influence of the control valve operational frequency, but the durability tests were controlled by the vehicle manufacturer, and the author could not interfere on the test conditions.

A semi-ellipse adaptation on the wear curve levels was proposed as an attempt to create a prediction for shaft and bushing wear, but that was not successful for the shaft, only for the bushing.

The wear rate was computed using as input the data from the experimental analysis. Not only from engine measurements but also from wear measurements. Varying some design parameters in the wear rate formulation, it was possible to evaluate their influence on the wear and the result was that bigger shaft and bushing diameters decrease the lifetime, whereas longer shaft and bushing improve the wear rate.

A great advantage of this work is that the experimental analysis data could be used in the extended wear rate calculation, which produces a closer result to the real application.

7.2 Future Works Proposals

Although the efforts exhausted in this work, there are subjects that can be further investigated to complement the wear analysis of the bypass valve applied on a regulated two stages turbocharger:

The force distribution along the shaft was considered linear in this work, but due to the different wear patterns measured from durability, specially the one with 150Hz PWM valve, it is worth studying other force distributions and check if they better describe the wear pattern.

The bypass system natural frequency of 300Hz can be excited by the turbocharger speed and by the engine speed in the case of a six cylinders. This can be further investigated to confirm if any resonance problem is involved in the wear.

The small movements – about 0.1mm – measured in the dynamometer and also in the vehicle test where the 21Hz PWM valve was replaced, suggests some kind of vibration problem and deserve a deeper analysis.

Due to the many variables of the durability tests with different engine types, drivers, track, etc., there were only two pairs of shaft and bushing that could be compared. In order to enrich the statistical analysis and gain more reliability, more components out of controlled durability tests must be analyzed.

In this dissertation, only two design parameters were evaluated to check the trend of the wear rate, but different other designs could be included in the wear rate calculation, as well as oscillatory forces with different frequencies.

References

AHMADI, N., KEER, L., & MURA, T. (1983). Non-Hertzian contact stress analysis for an elastic half space—normal and sliding contact. *International Journal of Solids and Structures*. Retrieved from <http://www.sciencedirect.com/science/article/pii/002076838390032X>

ALEKSANDROV, V. M., BRONOVETS, M. A., & SOLDATENKOV, I. a. (2008). Mathematical modeling of wear of journal bearings in outer space. *Journal of Friction and Wear*, 29(3), 182–187. doi:10.3103/S1068366608030057

CIAVARELLA, M., & DECUZZI, P. (2000). The state of stress induced by the plane frictionless cylindrical contact I. the case of elastic similarity. *International Journal of Solids and Structures*, 38, 4507–4523.

CIAVARELLA, M., & DECUZZI, P. (2001). The state of stress induced by the plane frictionless cylindrical contact II.pdf. *International Journal of Solids and Structures*, 38, 4525–4533.

DICKRELL, D. J., & SAWYER, W. G. (2004). Evolution of Wear in a Two-Dimensional Bushing. *Tribology Transactions*, 47(2), 257–262. doi:10.1080/05698190490439175

DINE, S., CROMER, R., & CALABRESE S. J. (1996). Redesigning Mechanical Systems for Low Wear Using System Dynamics Modeling *W ^*, 118(April), 0–7.

DROZDOV, Y. N. (1976). Development of a Method for the calculation of the life of a dry frictional contacts under extreme operating conditions. *Wear*, 38, 217–223.

JOHNSON, K. L. (1987). *contact mechanics*. New York: Cambridge University Press.

Kunert, K. von. (1961). Spannungsverteilung im Halbraum bei elliptischer Flächenpressungsverteilung über einer rechteckigen Druckfläche. *Forschung*, (1). doi:DK 539.319 : 539.383 : 531.252.001.5

MOSLEH, M., SAKA, N., & SUH, N. P. (2002). A mechanism of high friction in dry sliding bearings, 252, 1–8.

NAYAK, L., & JOHNSON, K. L. (1979). Pressure between elastic bodies having a slender area of contact and arbitrary profiles. *International Journal of Mechanical Sciences*, 21(4), 237–247. doi:10.1016/0020-7403(79)90067-5

WEN, J., & KHONSARI, M. M. (2009). Thermomechanical Coupling in Oscillatory Systems With Application to Journal Bearing Seizure. *Journal of Tribology*, 131(2), 021601. doi:10.1115/1.3071976

WILLIAMS, J. A. (1999). Wear modelling : analytical , computational and mapping : a continuum mechanics approach, 1–17.

APPENDIX A – MATLAB FILES

Le_dados_desgaste_Rmin.mat

```
clear all
close all
clc

for i = 1:9;
    arquivos(i,:) = ['p0' num2str(i,2) '.txt'];
end

for i = 10:32;
    arquivos(i-1,:) = ['p' num2str(i,2) '.txt'];
end

Rmax=0;
Rmin = 6;
for i = 1:size(arquivos,1);
    d = load(arquivos(i,:));
    Teta{i} = d(:,5);
    R{i} = d(:,4);
    z(i) = str2num(arquivos(i,2:3));
    if min(R{i}) < Rmin;
        Rmin = min(R{i});
    end
end

om = -180:0.1:180;
Ri = zeros(size(arquivos,1),length(om));

for i = 1:size(arquivos,1);
    Ri(i,:) = interp1(Teta{i},R{i},om);
end

[Om,Z] = meshgrid(om,z);
Ri = circshift(Ri,[0 1800]);

e=1e-3;
dL = 0.05; % intervalo entre as alturas
L = [0:dL:max(max(Ri-Rmin))];
i = 1;
%j = 4;

figure
mesh(Om,Z,Ri-Rmin);
xlabel('circumference [degree]')
ylabel('length [mm]')
title('Wear measurement')
```

```

axis([-200 200 0 40 0 1.6])

figure
cores = 'bgrcmykbgrcmykbgrcmykbgrcmykbgrcmykbgrcmykbgrcmyk';
marcador = '++++++dddddddssssss*****vvvvvv>>>>>><<<<<<<';

for j = 1:length(L)
    [lin{j},col{j}]=find(abs(Ri-Rmin-L(j))<e);

    omv{j} = om(col{j});
    zv{j} = z(lin{j});

    Rn(j) = mean(mean(Ri(lin{j},col{j})));
    omv{j} = (omv{j}-180)*pi/180;
    %A(j) = polyarea(Rmax*omv{j},zv{j});
    hold on

    [omp{j}, zp{j}]=poly2ccw(omv{j},zv{j});
    % plot3(omp{j},zp{j},L(j)*ones(size(omp{j})));
    P = [omp{j}.' zp{j}.''];
    M{j} = contorno_desgaste(P);
    omv{j} = M{j}(:,1);
    zv{j} = M{j}(:,2);
    omint{j} = spline(1:length(omv{j}),omv{j},linspace(1,length(omv{j}),200));
    zint{j} = spline(1:length(zv{j}),zv{j},linspace(1,length(zv{j}),200));

    A(j) = polyarea(Rmin*omint{j},zint{j});
    if j>1
        plot3(Rmin*omint{j},zint{j},L(j)*ones(size(omint{j})),[cores(j)
marcador(j) '-']);
        xlabel('circumference [mm]')
        ylabel('length [mm]')
        title('Wear measurement')

        omaux = omint{j};
        zaux = zint{j};

%semi-eixos
    semip1(j) = Rmin*(max(omaux)-min(omaux))*0.5;
    semip2(j) = max(zaux)-min(zaux);

    end
end

semip1=sort(semip1(end:-1:1),'ascend'); %ordem crescente
semip2=sort(semip2(end:-1:1),'ascend');

A = sort(A(end:-1:1),'descend');
L = L(1:end);
V(1) = 0;

for j = 2:length(A)

```

```

        V(j) = V(j-1)+dL*A(j);
    end
    A = sort(A(end:-1:1), 'ascend');

    figure
    plot(L,A)
    xlabel('wear depth [mm]')
    ylabel('wear area[mm^2]')
    title('Wear area vs wear depth')

    figure
    plot(L,V)
    xlabel('wear depth [mm]')
    ylabel('wear volume [mm^3]')
    title('cumulative wear volume vs wear depth')

    save dados_desgaste_VW278a_Buchse.mat L A semip1 semip2 zint Rmin

    %% Ajuste de elipse

    figure
    for j =3:length(omv)

        f = @(p,x) erro_elipse(p,x);

        omaux = omv{j};
        zaux = zv{j};
        d = [omaux zaux];

        %p0 chute inicial dos parâmetros da elipse
        p0 = [(max(omaux)-min(omaux))*0.5 max(zaux)-min(zaux) mean(omaux) max(zaux)];
        erro_elipse(p0,d)
        po = fminsearch(@(p) f(p,d),p0);
        erro_elipse(po,d)

        % elipse ajustada
        p = p0;
        x = linspace(p(3)-p(1),p(3)+p(1),200);
        y = p(4)-p(2)*sqrt(1-(x-p(3)).^2/p(1)^2);

        %semi-eixos
        semip1e(j) = Rmin*p(1);
        semip2e(j) = p(2);

        plot3(Rmin*omaux,zaux,L(j)*ones(size(omaux)),[cores(j) marcador(j) '-
        '],Rmin*x,y,L(j)*ones(size(x)));
        xlabel('circumference [mm]')
        ylabel('length [mm]')
        title('Wear measurement and adapted ellipse')
    end

```

```

% área ajustada por elipses
Ae(j) = pi*Rmin*p(1)*p(2)/2;

Ve(1) = 0;
for j = 2:length(Ae)
    Ve(j) = Ve(j-1)+dL*Ae(j);
end
axis([-32 -2 0 35])
hold on

end

semiple=sort(semiple(end:-1:1),'ascend'); %ordem crescente
semip2e=sort(semip2e(end:-1:1),'ascend');

Ae = sort(Ae(end:-1:1),'ascend');

figure
plot(L,Ae)
xlabel('wear depth [mm]')
ylabel('wear area[mm^2]')
title('Wear area vs wear depth- adapted ellipse')

figure
plot(L,Ve)
xlabel('wear depth [mm]')
ylabel('wear volume [mm^3]')
title('cumulative wear volume vs wear depth- adapted ellipse')

figure
plot(L,semiple)
xlabel('wear depth [mm]')
ylabel('semi axis circumference[rad]')
title('Circumference semi axis growth through wear depth- adapted elipsee')

figure
plot(L,semip2)
xlabel('wear depth [mm]')
ylabel('semi axis wear length [mm]')
title('Wear length semi axis growth through wear depth - adapted ellipse')

save dados_desgaste_VW278a_Buchse_Elipse.mat L Ae semiple semip2e Rmin

```

Dynamic.mat

```

clear all
close all
clc

```

```

%measurements from D0834 VW316 230cv WG Brazil setting point and Norgreen

```

```

%Arquivo VW316_Serra 6 descidas_AE13077-001.sif

load dinamica.mat
% load dados_desgaste_VW278a_Buchse.mat
load dados_desgaste_VW278a_Spindel.mat

figure
plot(Pact)
xlabel('Number of points')
ylabel('Actuator pressure [mbar]')
title('Actuator pressure')

figure
plot(Weg_act)
xlabel('Number of points')
ylabel('Actuator displacement [mm]')
title('Actuator displacement')

figure
plot(P3)
xlabel('Number of points')
ylabel('Exhaust gas pressure [mbar]')
title('Exhaust gas pressure')
%Parameters from drawings

rWG=13; %valve plate radius[mm]
rAct=10; %actuator diaphragm radius[mm]

BL=33.6; %Bushing Lenght [mm]
Rb=5.07; %bushing radius [mm]
Rs=5; %shaft radius [mm]
Es=1.761*10^5; %Elasticity modulus from shaft[N/mm^2]
Eb=1.825*10^5; %Elasticity modulus from bushing[N/mm^2]
vs=0.256; %Posisson ration shaft
vb=0.285;%Posisson ration bushing
dact=20; %[mm]
dP3=20; %[mm]
Preload=1; %[mm] precarga
k=8; % [N/mm]k da mola desenho 58061191318
Gs=Es/2*(1+vs);
Gb=Eb/2*(1+vb);
Js=pi*Rs^4/2;

P3=P3.*10^-4; %Transformar mbar em N/mm^2
Pact=Pact.*10^-4; %Transformar mbar em N/mm^2

Fspring=k*(Weg_act-Preload);
FP3=P3.*pi*rWG^2; %[N]
Fact=Pact.*pi*rAct^2; %falta considerar a força da mola [N]

k=0;
n=0;
t=0;

```

```

s=0;
u=0;
nlength=6459840;
for i=1:nlength
    Fact(i)=Fact(i)-Fspring(i);%considerando a força da mola [N]

    Teta(i)=Weg_act(i)/dact; %rad
    FP3y(i)= FP3(i)*cos(Teta(i)); %componente Y da força FP3
    FP3x(i)=FP3(i)*sin(Teta(i)); %componente X da força FP3

    FRes(i)=FP3y(i)-Fact(i);

    Mp3=FP3y(i)*dP3;
    Mact=Fact(i).*dact;
    Angle=((Mp3+Mact).*52.85)./(Js*Gs);

    if FRes(i)<0
        k=k+1;
    end
    if Weg_act(i)<0.05
        n=n+1;
    end
    if Weg_act(i)<=1
        t=t+1;
    elseif Weg_act(i)<=5
        s=s+1;
    elseif Weg_act(i)<=10
        u=u+1;
    end

    end

CF=(k/nlength)*100; %Porcentagem de valvulas fechadas por força
CD=(n/nlength)*100; %Porcentagem de valvulas fechadas por deslocamento=0
N01=(t/nlength)*100; %numero de pontos com abertura menor do q 1mm
N05=(s/nlength)*100; %numero de pontos com abertura entre 1mm e 5mm
N010=(u/nlength)*100; %numero de pontos com abertura entre 5mm e 10mm
MaxAngle=max(Angle)*180/pi; %graus

figure
plot(FRes)
xlabel('Number of points')
ylabel('FRes [N]')
title('Resultant Force FP3y-Fact')
hold on
plot(Fact,'g-')
hold on
plot(FP3y,'r-')
hold on
plot(FP3x,'m-')
legend('FRes', 'Fact', 'FP3y','FP3x')
% plot(Weg_act,'r-')

figure
plot(Teta.*Rs)%semiaxis

```

```

xlabel('Number of points')
ylabel('Circumference Semiaxis[mm]')
title('Valve Opening angle')

% XXXXXXXXXXXXXXXXXXXXXXXXXXXXXXXXXXXXXXXXXXXXXXXXXXXXXXXXXXXXXXXXXXXXX
%calculo dRdtkw
nlw = length(zint); % número de profundidades
    %R = Rmax-L;

    for i = 2:nlw
        R = Rmax-L(i);
        A1 = R./A(i);
        zM = max(zint{i});
        dRdtsKw = A1*(2*zM^3/3.*(FP3y-Fact')./BL+Fact'.*zM^2);
        Z=cumtrapz(dRdtsKw);
    %     T{i}=cumsum(dRdtsKw);
    end
% Total=cumsum(T,2);
Rmin=Rmax-max(L);
Kw=-Z./(Rmin-Rmax);

figure
plot(Kw)

%*****DIAMETRO MAIOR*****
% considerando areas de contato e força medidas, apenas parametro do
design
% foram alterados
RmaxDm=7.5;

    for i = 2:nlw
        RDm = RmaxDm-L(i);
        A1Dm = RDm./A(i);
        zM = max(zint{i});
        dRdtsKwDm = A1Dm*(2*zM^3/3.*(FP3y-Fact')./BL+Fact'.*zM^2);
        ZDm=cumtrapz(dRdtsKwDm);
    end

%     *****COMPRIMENTO MAIOR*****
%     considerando areas de contato e força medidas, apenas parametro do
design
%     foram alterados
BLCm =15+BL;

    for i = 2:nlw
        R = Rmax-L(i);
        A1 = R./A(i);
        zM = max(zint{i});
        dRdtsKwCm = A1*(2*zM^3/3.*(FP3y-Fact')./BLCm+Fact'.*zM^2);

```

```

        ZCm=cumtrapz (dRdtsKwCm);
    end

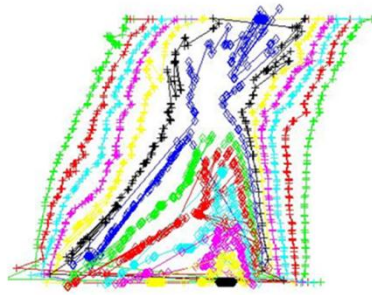
difCm=(Z./ZCm).*100;
difDm=(Z./ZDm).*100;

figure
plot(Z)
xlabel('Number of points')
ylabel('(dR/dt)*(1/K_w)')
title('Wear rate')
hold on
plot(ZDm,'r:')
hold on
plot(ZCm,'g-')
legend('Measured', 'Bigger diameter', 'Longer')

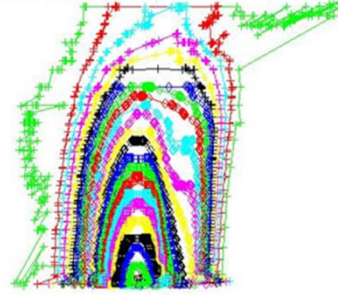
figure
plot(difDm,'r:')
xlabel('Number of points')
ylabel('Difference [%]')
title('Difference on wear rate comparing to actual design')
hold on
plot(difCm,'g-')
legend('Bigger diameter', 'Longer')

save forces.mat FP3y Fact

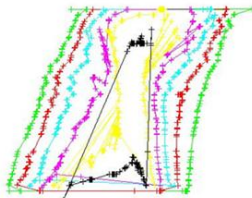
```

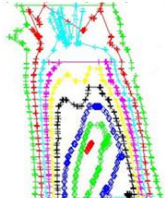
Shaft T4.2 – external diameter



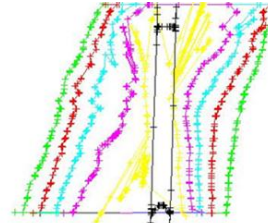
Bushing T4.2 – internal diameter



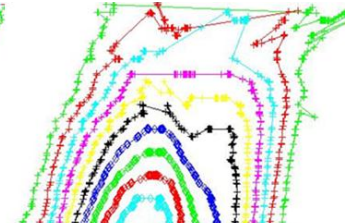
Shaft B4.1 – external diameter



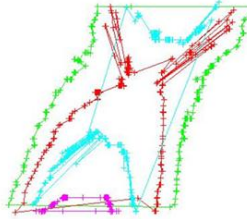
Bushing B4.1 – internal diameter



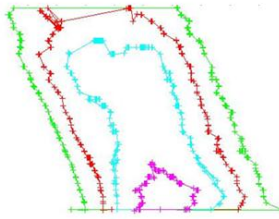
Shaft B4.2 – external diameter



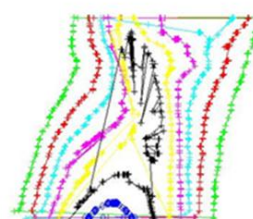
Bushing B4.2 – internal diameter



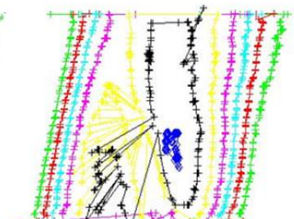
Shaft B4.3 – external diameter



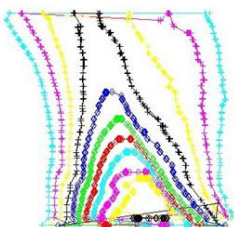
Bushing B4.3 – internal diameter



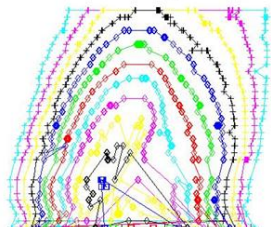
Shaft B4.4 – external diameter



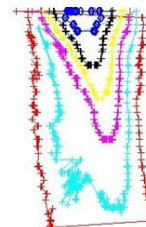
Bushing B4.4 – internal diameter



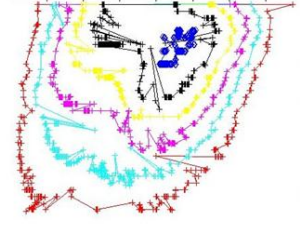
Shaft B4.5 – external diameter



Bushing B4.5 – internal diameter



Shaft B6.1 – external diameter



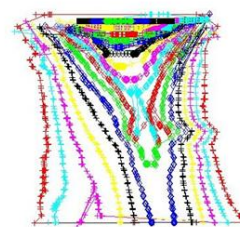
Bushing B6.1 – internal diameter



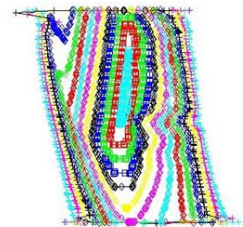
Shaft T6.1 – external diameter



Bushing T6.1 – internal diameter



Shaft T6.2 – external diameter



Bushing T6.2 – internal diameter